

VU Research Portal

Divide et Impera

de Man, S.P.J.

2011

document version

Publisher's PDF, also known as Version of record

[Link to publication in VU Research Portal](#)

citation for published version (APA)

de Man, S. P. J. (2011). *Divide et Impera: Multi-lockin instrument for surface force measurements and applications to Casimir force experiments*.

General rights

Copyright and moral rights for the publications made accessible in the public portal are retained by the authors and/or other copyright owners and it is a condition of accessing publications that users recognise and abide by the legal requirements associated with these rights.

- Users may download and print one copy of any publication from the public portal for the purpose of private study or research.
- You may not further distribute the material or use it for any profit-making activity or commercial gain
- You may freely distribute the URL identifying the publication in the public portal ?

Take down policy

If you believe that this document breaches copyright please contact us providing details, and we will remove access to the work immediately and investigate your claim.

E-mail address:

vuresearchportal.ub@vu.nl

DIVIDE ET IMPERA

Multi-lockin instrument for surface force measurements and
applications to Casimir force experiments

Sven de Man

Reading committee:

prof.dr. V. Adrian Parsegian, University of Massachusetts Amherst (United States)
prof.dr. Dirk Bouwmeester, University of California Santa Barbara (United States) and Leiden University (The Netherlands)
prof.dr. Joël Chevrier, Université Joseph Fourier Grenoble (France)
prof.dr. Elisabeth Charlaix, Université Lyon 1 (France)
prof.dr. Joost Frenken, Leiden University (The Netherlands)
dr. Rick Bethlem, VU University Amsterdam (The Netherlands)

Cover design: Jacob Kerssemakers

Printed by: IJskamp Drukkers

This work was funded by the Netherlands Organisation for Scientific Research (NWO) under the Innovational Research Incentives Scheme *Vernieuwingsimpuls* VIDI-680-47-209.

Vrije Universiteit
Faculty of Sciences
Department of Physics and Astronomy
Condensed Matter Physics
De Boelelaan 1081
1081 HV Amsterdam
The Netherlands

ISBN 978-94-91211-48-5

VRIJE UNIVERSITEIT

DIVIDE ET IMPERA

Multi-lockin instrument for surface force measurements and
applications to Casimir force experiments

ACADEMISCH PROEFSCHRIFT

ter verkrijging van de graad Doctor aan
de Vrije Universiteit Amsterdam,
op gezag van de rector magnificus
prof.dr. L.M. Bouter,
in het openbaar te verdedigen
ten overstaan van de promotiecommissie
van de faculteit der Exacte Wetenschappen
op dinsdag 14 juni 2011 om 11.45 uur
in de aula van de universiteit,
De Boelelaan 1105

door

Sven Pieter Johan de Man

geboren te Zuidelijke IJsselmeerpolders

promotor: prof.dr. R.P. Griessen
copromotor: dr. D. Iannuzzi

Contents

1	Introduction	3
1.1	The Casimir effect	4
1.2	Measuring the Casimir force	5
1.3	Our new experimental method	7
1.4	Sneak preview	12
1.5	A new force sensor	13
2	Calibration with the electrostatic force	16
2.1	Introduction	16
2.2	No anomalous scaling in electrostatic calibrations for Casimir force measurements	17
2.3	Contact potentials in Casimir force setups: an experimental analysis	28
2.3.1	Introduction	29
2.3.2	Experimental details	29
2.3.3	Results and discussion	32
2.3.4	Conclusions	39
3	Halving the Casimir force	40
3.1	Introduction	40
3.2	Halving the Casimir force with Conductive Oxides	41
3.3	Halving the Casimir force with conductive oxides: experimental details	51
3.3.1	Introduction	52
3.3.2	Experimental setup	52
3.3.3	Results and Discussion	60
3.3.4	Conclusions	75
4	Force measurements in gases	77
4.1	Introduction	77
4.2	On the use of Hydrogen Switchable Mirrors in Casimir force experiments	79
4.2.1	Introduction	80
4.2.2	Casimir effect with Hydrogen Switchable Mirrors: previous experimental results	82

4.2.3	Casimir effect with Hydrogen Switchable Mirrors: qualitative analysis of the experimental results	84
4.2.4	Casimir effect with Hydrogen Switchable Mirrors: is the modulation of the force observable?	85
4.2.5	Conclusions	95
4.3	Force measurements in H ₂ gas	97
4.4	Hydrodynamic force measurements in various gases	105
5	Fiber-top and Ferrule-top Casimir force measurements	110
5.1	Introduction	110
5.2	Casimir force experiments in air: Two birds with one stone	112
5.2.1	Fiber-top Casimir force setup	113
5.3	Measurement of the Casimir force with a ferrule-top sensor	116
5.3.1	Introduction	117
5.3.2	Experimental setup	118
5.3.3	Results and discussion	122
5.3.4	Conclusions	126
5.4	Simple fiber-optic interferometer with linear phase response	127
Appendix		135
A Calculation of the Casimir force		136
Bibliography		137
Summary		143
Samenvatting		146
List of publications		150
Articles		150
Patent		152
Talks		152
Acknowledgment		154
Curriculum Vitae		155

Chapter 1

Introduction

The mechanical parts of Micro- and NanoElectroMechanical Systems (MEMS and NEMS) are often designed to work at separations where the interaction mechanisms caused by quantum fluctuations of the electromagnetic field cannot be neglected. It is well known, for example, that non-retarded van der Waals forces play a central role in interfacial adhesion and friction between surfaces in contact [1]. At larger separations, long-range retarded van der Waals forces can still affect the performance of MEMS and NEMS [2–4]. It is thus now commonly believed that, if one could suitably engineer the strength of those interactions with techniques that can be easily reproduced in micro- and nanofabrication processes, unprecedented opportunities would come available for the development of conceptually new MEMS and NEMS [5–10]. For this reason, previous studies on dispersion forces in colloidal suspensions [11, 12] are currently receiving renewed attention [7, 13, 14], because they prove that the retarded van der Waals attraction can be largely reduced or even switched to repulsive if the gap between the surfaces is filled with a liquid [15–17]. Since MEMS and NEMS are often designed to work in air or other gaseous environments, it is now interesting to investigate whether similarly dramatic effects can be observed in the absence of liquids, where, due to historical reasons, the long-range retarded van der Waals force is called Casimir force [18].

Driven by these considerations, over the last four years we have developed an experimental setup designed to carry out precise measurements of the Casimir force between a sphere and a plate in the presence of a gaseous intervening medium [19, 20]. In this thesis we describe the instrument and the experimental procedure, show its versatility as a general tool for the investigation of forces between surfaces at sub-micron separation, and present several original results obtained with this setup.

This chapter is partially based on the paper: S. de Man, K. Heeck, K. Smith, R. J. Wijngaarden, and D. Iannuzzi, *Int. J. Mod. Phys. A* **25**, 2231 (2010)

1.1 The Casimir effect

With the development Quantum Mechanics and Quantum Electrodynamics, we have come to understand that the vacuum ground state is not empty, but filled with continuous fluctuations of the electromagnetic field. These fluctuations are often interpreted as virtual particles that frequently pop in and out of existence to disturb the emptiness of vacuum, and have observable consequences like the Lamb shift and spontaneous emission [21]. It was not until 1948, however, that it was realized that these quantum fluctuations would have any effect on macroscopic objects. Hendrik Casimir, at that time working at Philips Research (Philips Gloeilampenfabriek NV), considered what would happen with two perfectly conductive and electrically neutral plates placed parallel in a vacuum filled with electromagnetic fluctuations [18]. Since the plates impose boundary conditions on the electromagnetic fields, the number of allowed vacuum modes inside the cavity is substantially less than outside the cavity. Casimir derived that the plates are actually pulled together by the quantum fluctuations, by showing that the total free energy of the system decreases as the cavity gets smaller. It was later shown that one can also state that the virtual photon pressure on the outside walls of the cavity is stronger than on the inside walls, because more vacuum modes exist outside the cavity than inside [22]. The Casimir force between perfectly conducting plates is given by

$$F_C = -\frac{\pi^2 \hbar c A}{240 d^4}, \quad (1.1)$$

where A is the area of the plates, d is the distance between them, and \hbar and c are the usual fundamental constants. Interestingly, apart from the prefactor $\pi^2/240$, this equation can be obtained from dimensional analysis. In fact, the notion of a quantum force combined with electromagnetic field fluctuations leads naturally to $F \propto \hbar^\alpha c^\beta$. Considering that the force has to scale linearly with A and should depend on distance, we have $F \propto \hbar^\alpha c^\beta A d^\gamma$, of which the only solution with correct units is $\alpha = 1$, $\beta = 1$, and $\gamma = -4$.

In 1956, E. M. Lifshitz generalized the theory to incorporate the finite conductive of the plates that form the cavity [23]. He followed a different route than Casimir and started from the dipole-dipole interaction between the atoms of the interacting surfaces. He then performed a continuous medium approximation and described the dielectric properties of the surfaces with their dielectric functions. Furthermore, Lifshitz took into account that the electromagnetic fields that travel from one plate to the other have a finite propagation speed, namely the speed of light. Lifshitz final result is, although mathematically quite involved, very illuminating. His result turned out to be equivalent to Casimir's result when one substitutes perfectly conducting dielectric properties, but he also recovered the Van der Waals force for small plate-plate separation. For relatively large separation (i.e. larger than roughly 10 nm),

the finite speed of light starts to play a role, and the force is then called “retarded Van der Waals force”. Lifshitz thus accomplished to unify the Van der Waals force and the Casimir force, and showed that both are limiting extremes of the same interaction. In the literature, there is no strict distinction in the use of this terminology, and the wording Casimir effect is also used for the interaction between real (dielectric) materials.

The first attempt to experimentally verify the existence of the Casimir effect was carried out by Sparnaay, a colleague of Casimir at Philips in 1958 [24]. His results did not deviate significantly from Casimir’s theory, but were certainly not precise enough to confirm it either. In 1978, though, Van Blokland and Overbeek measured the force between two surfaces coated with chromium [25]. Their experiment demonstrated the existence of the Casimir force and showed good agreement with the Lifshitz theory. In 1997, Lamoreaux published the force data he acquired with his torsion pendulum setup and also showed good agreement between theory and experiment [26]. From then on, various groups started to perform Casimir force measurements and begun to investigate both fundamental and practical aspects of the Casimir effect. For a general review, see, for example, [5] or [27].

The Casimir effect has received a lot of attention in the literature during the last decade, because of its fundamental nature and perhaps also its magic appearance. In experimental tests probing forces at short separations, the Casimir force is often considered as a major background force that has to be accurately accounted for. The main problem with the Casimir effect in such experiments is that one cannot switch it off: it will thus always be present in force measurements between closely spaced objects. Only by changing the dielectric properties of the interacting surfaces or by altering the intervening medium can one reduce the interaction strength. In the search for new extra-gravitational forces at short distances, a solid understanding of the Casimir force is essential.

From a more practical point of view, the miniaturization of all kinds of electrical and mechanical devices has brought the relevant dimensions down to such a degree that the Casimir and Van der Waals forces are becoming the dominant interaction mechanisms. In particular, stiction in MEMS and NEMS is often governed by these forces [1, 4]. Therefore, finding ways to reduce the Casimir force will allow MEMS and NEMS to become even more compact.

1.2 Measuring the Casimir force

The Casimir force is quite a weak force and notoriously difficult to measure because it is easily dominated by electrostatic forces. There are only a handful of experimental setups in the world that can provide systematic measurements of the Casimir interaction. These setups can be divided into macroscopic and microscopic versions. The torsion balance is a significant example of the macro-

scopic branch as it is widely used for detection of small forces, most notably the gravitational force. It is also used for the detection of the Casimir force in the sphere-plate geometry, for example by Lamoreaux in 1997 [26] and more recently in Japan in 2009 [28]. In 2002, researchers in Italy used a macroscopic cantilever (2 cm long) and a parallel juxtaposed surface to study the Casimir effect in the plane-plane geometry [29]. It is commonly understood that with these macroscopic setups it is more difficult to control spurious electrostatic forces than in microscopic ones, because of the difficulty to create large surfaces with homogenous electric properties (e.g. uniform work functions).

It is therefore not surprising to see that most groups investigating the Casimir effect have resorted to the use of micromechanical systems in the sphere-plane geometry. These microscopic setups can then be split into two groups, namely based on MEMS see-saw force sensors or based on Atomic Force Microscopy (AFM). The see-saw Casimir force experiments were started at Bell Labs by Capasso and Chan [2, 3] and later on used by both Decca [30, 31] and Iannuzzi [32, 33]. The AFM approach to measuring surface forces between a sphere and a plate was initiated by Ducker [34] and applied to Casimir force measurements by Mohideen [35]. Now several groups are using this device to obtain systematic data, for example the groups of Chevrier [36] and Binns [37]. Our work also fits into this last category, although we have significantly improved the experimental method and setup to obtain very reproducible force measurements.

In general, in a Casimir force setup, there are at least three technical issues that must always be carefully addressed:

- *Calibration:* Casimir force experiments necessarily rely on a force sensor. The force sensor must be calibrated with a known force. Furthermore, one must be sure that, during the measurements, the calibration parameters do not vary significantly.
- d_0 : in most of Casimir force setups, the two interacting surfaces are initially put at a given separation d_0 , and then moved closer and closer with calibrated steps or ramps. The initial value of d_0 is not known *a priori*. d_0 must thus be independently measured, and must remain constant within one run. It is thus highly desirable to measure how much thermal drifts influence the measurement of d_0 [19, 20, 36].
- V_0 : the electrostatic potential difference between two juxtaposed surfaces connected to ground is, in general, not zero. The residual potential V_0 can give rise to electrostatic forces that easily overcome the Casimir force. It is thus important to measure V_0 and apply a counter-bias potential to compensate for this effect. Recently, it has been emphasized that V_0 , in general, varies with surface separation and time [19, 38, 39]. A single

measurement for one single separation is thus not sufficient for accurate Casimir force experiments.

We have developed an experimental method that allows one to simultaneously (i.e., in the same run): (i) calibrate the force sensor, (ii) measure d_0 , (iii) compensate for V_0 , (iv) measure the Casimir force [19, 20]. In the next section, we give an overview of the experimental method. Further on in the thesis the experimental method is discussed in full detail (see, for example, section 3.3).

1.3 Our new experimental method

The experimental setup we designed to perform precise measurements of the Casimir force is a custom made Atomic Force Microscope (AFM). The measurement head is from a Veeco Multimode AFM (with low-noise laser upgrade). The force sensor is a 1 N/m Si cantilever with a 200 μm diameter sphere attached to its free end. This sensor is mounted into the AFM head, and its deflection is measured with an optical lever, where a light beam reflected from the back of the cantilever is detected by a position sensitive photodetector. The surface of the sphere has to be brought in close proximity to another surface, in order for the Casimir effect to become measurable. We mount a planar sample on a piezoelectric stage that is feedback controlled with an internal capacitive sensor (resolution on the order of 50 pm). The calibrated translator is used to accurately vary the separation between the surfaces. We also added a stick-slip piezoelectric stepper motor to perform the coarse adjustment of the sample position. The measurement head and piezoelectric positioning stage (feedback controlled piezo and stepper motor combined) are mounted on an aluminum block that functions as a temperature stabilized heat reservoir roughly 10 K above room temperature; mechanical drifts due to expansion and contraction of the setup is hereby strongly reduced. The AFM is then placed on an active anti-vibration platform inside an anechoic chamber to isolate the setup from mechanical and acoustic vibrations (see Fig. 1.1a). The anechoic chamber is placed on an optical table inside a temperature controlled laboratory. In Fig. 1.1b, we show a close-up of our custom designed AFM. Apart from the AFM head and positioners, an optical fiber mounted on a mechanical translation stage is visible on the forefront of the photo. This fiber is pointed towards the bottom of the sample, and is used as an interferometer to measure the phase and amplitude of a small modulation of the planar sample position, as will become clear later in the text.

The technique employed to tackle the technical issues common to Casimir force experiments is based on Kelvin probe force microscopy[40]. The trick is to apply an AC potential difference across the sphere and planar sample surfaces, which will give rise to two signals at different oscillation frequencies

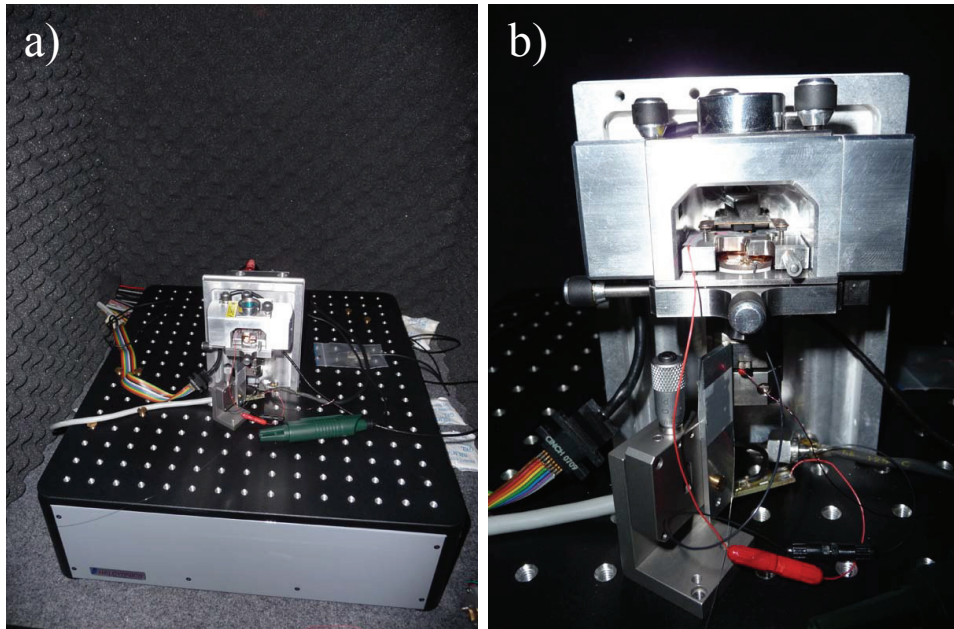


Figure 1.1: Photographs of the Casimir force setup. a) Our custom built Atomic Force Microscope (AFM) mounted on an active anti-vibration stage inside an acoustic isolation box. b) Close-up of the AFM with the Veeco Multimode measurement head mounted at the upper part of an aluminum block and the piezoelectric translators mounted underneath the head. In front of the AFM, an optical fiber is mounted on a manual translation stage pointed at the piezoelectric stage to interferometrically measure the phase and amplitude of the separation modulation (see text for details).

that will allow us to calibrate the instrument and extract d_0 , and compensate the residual potential V_0 independently.

The electrostatic force between a conductive sphere and a conductive plate at separation d is

$$F = \frac{\varepsilon_0 \pi R V^2}{d} \quad (1.2)$$

where ε_0 is the permittivity of vacuum, R is the radius of the sphere, V is the net potential difference across the surfaces, and $d \ll R$ (Proximity Force Approximation[41]). Since the photodetector signal, S , depends linearly on the deflection of the cantilever, it is clear that S is proportional to the applied force.

Let's now suppose that there exists no residual contact potential difference between the two surfaces (i.e. $V_0 = 0$). Then the signal arising from the oscillating potential difference $V(t) = V_{AC} \cos(\omega_1 t)$ satisfies

$$S_{V_0=0}(t) \propto \frac{(V(t))^2}{d} = \frac{(V_{AC} \cos(\omega_1 t))^2}{d} = \frac{V_{AC}^2}{2d} + \frac{V_{AC}^2}{2d} \cos(2\omega_1 t) \quad (1.3)$$

in which the fact that the electrostatic force depends quadratically on voltage results in a signal at $2\omega_1$, twice the driving frequency (with $\omega_1 \ll \omega_{res}$, the free resonance of the cantilever). The amplitude of the oscillating signal at $2\omega_1$, which we will call $S_{2\omega_1}$, is measured by a lock-in amplifier and used to extract d_0 and to calibrate the force sensitivity of the instrument as explained in a previous paper[19]. By examining the value of d_0 for consecutive measurement runs, we established that the mechanical drift of our setup is ≤ 0.2 nm per measurement run [19, 20]. If one would keep V_{AC} constant during a measurement run in which the separation d is varied, the amount of cantilever oscillation would strongly vary as the force diverges for small d (see Eq. 1.2 and 1.3). To avoid that, the lab computer is reducing V_{AC} as the separation decreases (the computer symbol in Fig. 1.2a)[19]. In this way, we typically keep the electrostatic calibration force constant at roughly 100 pN RMS [19].

However, even when both surfaces are coated with the same material, there generally is a contact potential difference V_0 between the surfaces. We have to compensate this residual potential in order to have no background electric force in our Casimir force measurement. The counter bias voltage is a DC voltage that we call V_{DC} (see Fig. 1.2a). Then the presence of both potentials V_0 and V_{DC} implies

$$\begin{aligned} S(t) &\propto \frac{(V(t) + V_0 + V_{DC})^2}{d} \\ &= \frac{(V_0 + V_{DC})^2}{d} + \frac{2(V_0 + V_{DC})V_{AC}}{d} \cos(\omega_1 t) + \frac{V_{AC}^2}{2d} + \frac{V_{AC}^2}{2d} \cos(2\omega_1 t) \end{aligned} \quad (1.4)$$

The cross-product appears at the frequency ω_1 and is proportional to $(V_0 + V_{DC})$. By measuring the amplitude S_{ω_1} of this signal with a lock-in amplifier we can

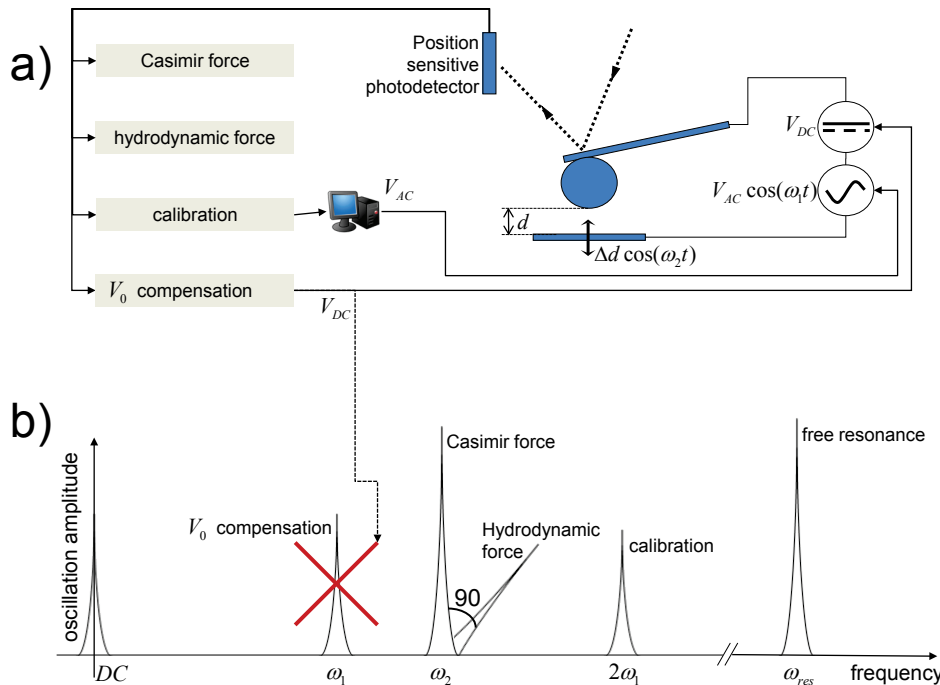


Figure 1.2: a) Schematic of the experimental setup and working principle. b) Spectrum of the motion of the cantilever in response to the electric, Casimir and hydrodynamic forces, as a result of an oscillating potential difference across the interacting surfaces at ω_1 and the small modulation of the separation d at ω_2 . The dashed arrow between figures a) and b) indicates that the V_0 compensation mechanism effectively zeros the signal at ω_1 . See text for details.

create a negative feedback loop that generates V_{DC} in such a way that S_{ω_1} becomes negligible, i.e. $V_0 + V_{DC} = 0$ [19, 39]; this feature is indicated in Fig. 1.2 by the dashed arrow that point from Fig. 1.2a to Fig. 1.2b and eliminates the presence of the signal peak at ω_1 . We have thus successfully compensated the contact potential difference between the interacting surfaces. Note that the addition of both V_0 and V_{DC} in the treatment does not alter the amplitude of the oscillation at $2\omega_1$ ($S_{2\omega_1}$).

With the residual potential compensated, the force sensitivity calibrated, and the absolute surface separation determined, we can now turn to the actual measurement of the Casimir force. As it is hard to measure the static deflection of the cantilever resulting from the Casimir force (the force is small, the spring constant is relatively high, and the read-out is not very stable in DC), we resort again to a modulation technique. We let the planar sample execute a very small oscillatory motion $\Delta d \cos(\omega_2 t)$, with $\Delta d \simeq 2$ nm and $\omega_2 \ll \omega_{res}$. As a result, there will be an in-phase oscillatory response of the cantilever because the Casimir force is separation dependent:

$$S_{\omega_2}^I(t) \propto \frac{\partial F}{\partial d} \Delta d \cos(\omega_2 t) \quad (1.5)$$

where $\partial F / \partial d$ represents the gradient of the force at the current separation. By measuring the amplitude of $S_{\omega_2}^I(t)$ with another lock-in amplifier, we measure directly the gradient of the Casimir force*. In the sphere-plane geometry that we employ, and within the validity of the Proximity Force Approximation[41], the measured Casimir force gradient is equal to the expected force between parallel plates.

As the measurements are performed in air, the oscillation of the position of the planar sample gives rise to a moving column of gas above it. This results in a hydrodynamic interaction between the plate and the sphere, resulting in a signal of the form:

$$S_{\omega_2}^Q(t) \propto \frac{v(t)}{f(d)} = \frac{\omega_2 \Delta d \sin(\omega_2 t)}{f(d)} \quad (1.6)$$

where $v(t)$ is the velocity of the plate, and $f(d)$ is constant for separations $d \gg R$, is proportional to d for separations for which both $d \ll R$ and the non-slip boundary conditions for the Navier-Stokes equations are valid, and has a more complicated dependence on distance for values of d close to the mean free path of the air molecules due to the gas slip at the surfaces[42, 43]. From Eqs. 1.5 and 1.6, it is clear that both signals at ω_2 are orthogonal (one is a cosine, the other a sine), and can thus be independently measured with

*There is also a small contribution of the gradient of the electrostatic calibration force to $S_{\omega_2}^I(t)$, but we can correct for that with the simultaneous measurement of $S_{2\omega_1}$. The derivation of this correction goes beyond the scope of this section.

the same lock-in amplifier locked at ω_2 [†]. It is of crucial importance, however, that the phase of the lock-in amplifier is aligned perfectly with the actual phase of the oscillatory motion of the plate, because otherwise both signals $S_{\omega_2}^I(t)$ and $S_{\omega_2}^Q(t)$ get mixed by the lock-in. The fiber optic interferometer is used to secure the correct phase alignment of the ω_2 lock-in amplifier. Using the setup described above, we have recently explored the role of conductive oxides in Casimir force experiments (see chapter 3).

1.4 Sneak preview

Stiction and jump-to-contact in MEMS and NEMS is mainly caused by electrostatic and Casimir/van der Waals forces. Although the electrostatic interaction can be controlled by using metallic coatings, their result is a strong Casimir interaction, as reflective materials tend to cause strong confinement of the electromagnetic vacuum fluctuations. Therefore, to reduce both the electrostatic and Casimir interactions in a MEMS or NEMS, one would need to use a material that is DC conductive to get rid of electric charges, but insulating at optical frequencies to reduce the Casimir interaction. One such a material is Indium Tin Oxide ($\text{In}_2\text{O}_3:\text{Sn}$), a material widely used in semiconductor industry, for example in LCD displays and touch screens. We have performed Casimir force measurements between a gold coated sphere and a plate coated with this transparent conductive oxide, and we have demonstrated that the Casimir interaction between these surfaces is halved with respect to the gold-gold interaction, and that the ITO surface is conductive enough to prevent any electrostatic interaction. Thus the total force between these surfaces is very small. Coating of MEMS and NEMS surfaces with ITO could, therefore, extend the working range of these devices because of less severe stiction problems. The experiment is described in chapter 3.

Next to performing Casimir force measurements, we have used this setup to verify the distance dependence of the electrostatic force between a sphere and a plate, investigated contact potential variations, measured hydrodynamic forces at short separations, and even explored chemical forces due to hydrogen adsorption. The verification of the electrostatic force is crucial for our Casimir force measurements, because we calibrate our system with this force. Using our calibrated piezoelectric stage (calibrated with respect to traceable standards), we verified with high statistics the $1/d$ distance scaling of the force, and ruled out any spurious scaling as observed in a different experimental setup [38]. Furthermore, we also found that the contact potential compensation scheme that we use is supplying a distance dependent counter bias to the sphere and plate, implying that the net contact potential difference between the sphere

[†]Note that the implicit time dependence of d in $f(d)$ (due to the separation modulation at ω_2) does not invalidate eq. 1.6, as it will only cause signals at higher harmonics of ω_2 .

and plate is separation dependent. This effect is observed also in other setups in the world, and is still under debate. These results are presented in chapter 2.

The small mechanical oscillation of the plate that we use to measure the Casimir force gradient also generates a hydrodynamic interaction between the sphere and the plate. The gas molecules in the gap between the interacting surfaces is pushed in and out continuously. Of course, the strength of this interaction depends on the specific gas molecules that are mediating the force. We have therefore investigated the hydrodynamic interaction between a $100\ \mu\text{m}$ radius sphere and a plate in the separation range from $10\ \mu\text{m}$ to $100\ \text{nm}$ in air, He, Ar, and SF_6 gas. Although air and Ar are gases with typical mean free paths, He and SF_6 represent two extremes on the mean free path scale. He is the smallest and lightest gas molecule and has therefore the longest mean free path, while SF_6 is a large and heavy molecule with a very short mean free path. Since the hydrodynamic interaction is governed by collisions of the gas molecules amongst themselves and with the interacting surfaces, the force should depend drastically on the mean free path. Because our setup was designed to measure the Casimir force, it gives hydrodynamic force data at small separation with unprecedented accuracy and reproducibility. We present our results on this interesting subject in chapter 4.

Apart from using gases to change the strength and form of the hydrodynamic interaction, one could also use a gas to switch the Casimir force, as proposed and tried by Iannuzzi [32] with H_2 gas. In that experiment, the researchers had coated one of the surfaces with a Hydrogen Switchable Mirror (HSM) [44], a material that changes its dielectric properties from metallic to insulating upon exposure to hydrogen gas. Since the Casimir effect depends strongly on the dielectric properties of the surfaces, a decrease of the force was expected. In chapter 4 we compute how much of a decrease in the force one should detect when the HSM loads with hydrogen. This calculation clarifies the negative outcome of the experiment, because the resolution of their MEMS based Casimir setup was not sufficient to observe the predicted effect. On the other hand, this calculation also shows that the expected switch in the force should be easily detectable by our Casimir force setup in its present state. Motivated by this, we also performed force measurements with HSM's in hydrogen atmosphere. However, instead of a reduction of the force upon hydrogenation we observed a significant increase in the force, especially at large separation. This leads us to believe that the strong interaction is some kind of electrostatic force caused by the adsorption of the hydrogen molecules on the surfaces. These fascinating results are presented in chapter 4.

1.5 A new force sensor

During my research on the Casimir effect, our group invented a new optical fiber force sensor. This invention was triggered by a technical problem related

to the optical lever force detection as used in our AFM. The laser light that is used to detect the deflection of the cantilever is not entirely reflected by the cantilever, therefore part of the light hits the sample and is reflected from there into the detector. This second light path interferes with the original one coming from the cantilever, giving rise to spurious detection signals. We have therefore used a single mode optical fiber to guide the laser light inside its $7\ \mu\text{m}$ core and carved a cantilever out of the end of the fiber itself. Since the cantilever is placed directly on top of the fiber core, and it is significantly wider than the core, all light is reflected back into the fiber; no light reaches the sample. The deflection of this carved out cantilever is measured interferometrically by examining the amount of light traveling backwards into the fiber. The detection precision of this technique is comparable to the AFM optical lever readout. The versatility of this sensor, however, is huge. We have already demonstrated that it can be used for measurements of temperature, sample stiffness, index of refraction, hydrodynamic forces and Casimir forces, and used it for AFM topography and detection of chemical species [45–49]. The sensor is fabricated with a Focused Ion Beam (FIB) milling device and a FIB micrograph of such a device is shown in Fig. 1.3. Because of its all-optical design, the sensor is especially suitable for use in critical environments like explosive gases and ultra-low temperatures.

In chapter 5, we present our efforts to measure the Casimir force using a fiber-top force sensor. To increase the sensitivity with respect to a normal rectangular beam cantilever (as shown in Fig. 1.3), we fabricated a torsional device from the end of the fiber. The sensitivity of this device turned out to be very good, i.e. comparable to the resolution of our AFM-based setup, but we were unable to perform Casimir measurements with the device; most likely the gas flow resulting from the oscillation of the bottom plate in our measurement technique caused erratic motion of the torsional cantilever, thus rendering it useless. The electrostatic calibration measurements (with plate oscillation turned off) worked without flaw though.

To overcome this limitation, we scaled up the device and fabricated the cantilever from a ferruled fiber, instead of just a fiber [50]. A ferrule is a block of glass (typically 5 mm diameter and 5 mm height) with a hole in the center in which the optical fiber is glued. This allows us to machine a long cantilever with reasonably low spring constant. This ferrule-top sensor was then used to measure the Casimir force with high precision between two gold surfaces. These measurements are presented in chapter 5.

Currently, the group is employing these ferrule-top sensors for AFM design [51], stiffness measurements, humidity measurements, biochemical detection, and fluid flow experiments, opening up an entire new field of research.

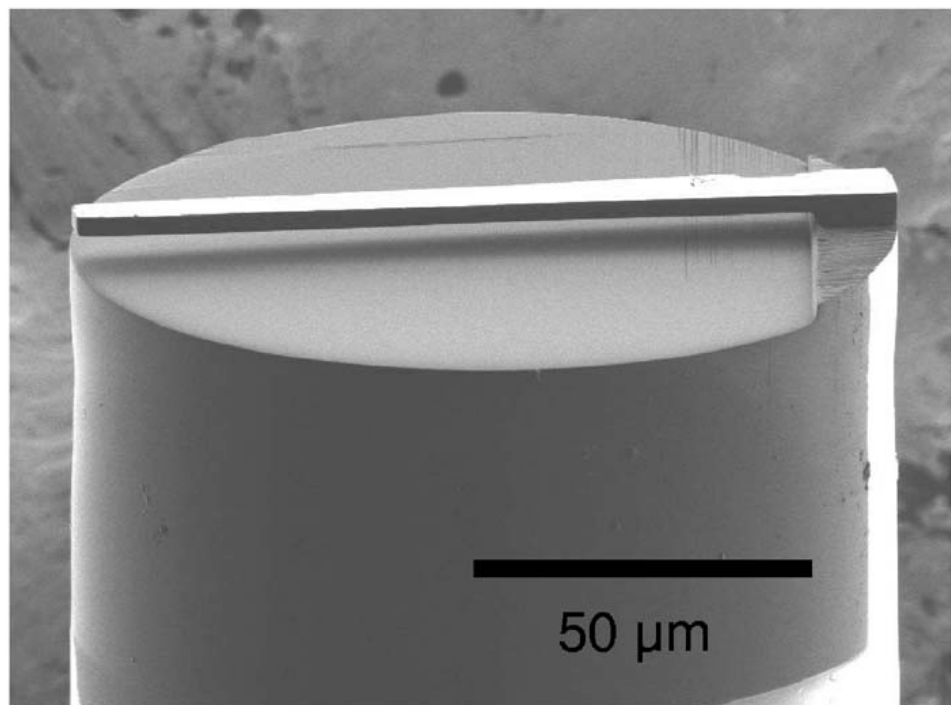


Figure 1.3: Focused Ion Beam (FIB) micrograph of a fiber-top cantilever. The light is guided by the fiber core, which is located in the center of the fiber, directly below the cantilever.

Chapter 2

Calibration with the electrostatic force

2.1 Introduction

To accurately calibrate our Casimir force setup, we have chosen to use the electrostatic interaction. This interaction is easy to control by applying external voltages to the interacting surfaces, and is well understood after two centuries of physics research. It is therefore not surprising to see that most Casimir force setups in the world are in fact calibrated using the electrostatic interaction [30, 32, 35, 36, 52, 53]. In 2008, however, a research group from Dartmouth College presented measurements in which the distance dependence of the electrostatic force was not matching the theoretical law. Motivated by this finding, we gathered systematic measurements of the electrostatic interaction with our setup, and showed that we do not observe this anomaly. Our data agree very well with the theoretical predictions, and thus allow us to indeed use the electrostatic interaction to calibrate our instrument. In section 2.2, we describe our findings concerning the behavior of the electrostatic force.

Secondly, in the last couple of years, more and more groups have identified a possible problem in their measurements. Although it is well known that one has to supply a bias voltage to the surfaces to cancel the electric field generated by the difference in surface work functions, it is new that this bias voltage needs to be distance dependent in order to minimize the electric field in the gap. We have also observed this effect, and it is treated briefly in section 2.2. Since no explanation for this distance dependent bias voltage has been found until now, we have explored this strange behavior in more detail, addressing both time dependence (drifts) and separation dependence individually. These results are presented in section 2.3.

Note that in this chapter $\omega \equiv \omega_1$, because only one modulation is used, and that $S_{2\omega}$ is defined as peak-to-peak instead of amplitude like in the rest of the thesis.

2.2 No anomalous scaling in electrostatic calibrations for Casimir force measurements

Abstract – In a recent paper (Phys. Rev. A **78**, 020101(R) (2008)), Kim *et al.* have reported a large anomaly in the scaling law of the electrostatic interaction between a sphere and a plate, which was observed during the calibration of their Casimir force setup. Here we experimentally demonstrate that this behavior is not universal. Electrostatic calibrations obtained with our setup follow the scaling law expected from elementary electrostatic arguments, even when the electrostatic voltage that one must apply to minimize the force (typically ascribed to contact potentials) depends on the separation between the surfaces.

Casimir force experiments are routinely used to set new limits on Yukawa corrections to the Newtonian gravitational attraction between surfaces at sub-micron separation (see [54] and references therein). To strengthen those constraints, new experiments must provide data with errors smaller than any other previous measurement. With claims reaching 0.19% relative experimental errors at a 95% confidence level [54], it is important to ask whether there exists any technical challenge or physical mechanism that might impede any further improvement in this important field.

In a recent paper [38], Kim *et al.* have reported a systematic effect observed during the calibration of their Casimir force setup that might represent a severe limitation to the development of future experiments on the Casimir effect, and that, in some extent, might have been overlooked even in previously reported high accuracy measurements. They observed that the electrostatic force gradient between a $\simeq 30$ mm radius spherical mirror and a metallic plate scales with surface separation d like $\simeq 1/d^{1.7}$, which represents a 15% deviation on the exponent with respect to the $1/d^2$ behavior expected from elementary electrostatic calculations. If this anomaly were confirmed to be a general phenomenon for metallic surfaces at very close separations, all the arguments used to calibrate high accuracy Casimir force setups, which relies on elementary analysis of the electrostatic attraction between the two surfaces, would be invalidated *, with severe consequences on the results of those experiments. Driven by these considerations, we have performed a high precision experiment to investigate the electrostatic force between a sphere and a plate in the separation range from $\simeq 100$ nm to $\simeq 2$ μm .

The main goal of this paper is to test the validity of:

$$F = -\frac{\varepsilon_0 \pi R (V + V_0)^2}{d}, \quad (2.1)$$

where F is the electrostatic force expected between a spherical surface of radius R and a plate kept at a separation d with $d \ll R$, and where ε_0 is the permittivity of vacuum, V is the applied voltage, and $-V_0$ represents the voltage that one has to apply to obtain minimal electrostatic force (typically ascribed to contact potentials) [26].

In the apparatus used for this experiment (see Fig. 2.1), the sphere is directly glued under the hanging end of a micromachined cantilever (the force sensor), which is then mounted inside the measuring head of a commercial atomic force microscope (AFM). The plate is anchored to a custom-designed mechanical stage, which is fixed underneath the AFM head. The mechanical stage allows one to bring the plate in close proximity with the sphere, and to perform measurements of the force as a function of separation.

*This argument does not apply to Casimir force experiments between surfaces in liquids [13], which, however, have not been used to set new limits on Yukawa corrections to gravity.

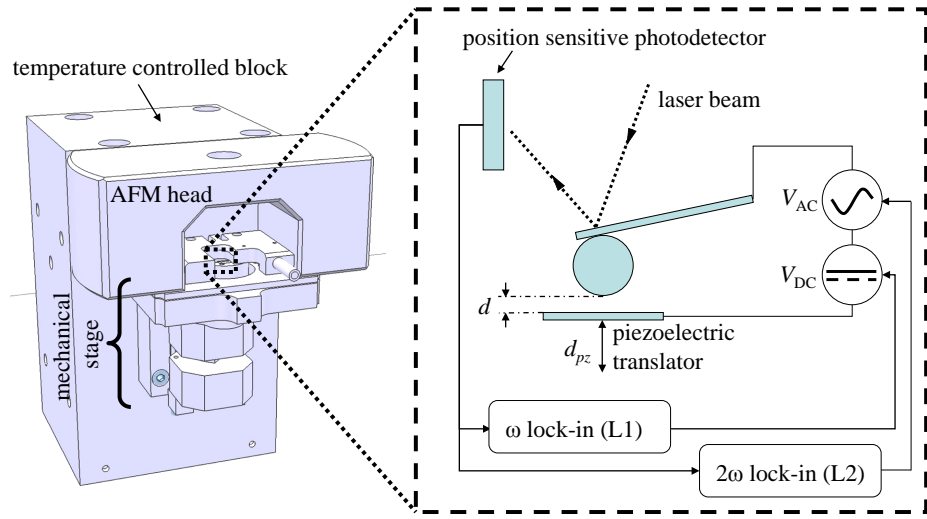


Figure 2.1: Schematic view of the experimental apparatus.

The force sensor used in this experiment is a rectangular Si cantilever ($525 \times 35 \times 4 \mu\text{m}^3$) with nominal spring constant $k \simeq 0.9 \text{ N/m}$. A $100 \mu\text{m}$ radius polystyrene divinylbenzene sphere (Duke Scientific) is attached to the free end of the cantilever with UV curable glue. The cantilever and the sphere are then coated with a 10 nm Ti adhesion layer and a 200 nm Au film by magnetron sputtering. A similar coating is also deposited onto the plate – a $5 \times 2 \text{ mm}^2$ polished sapphire slide. The AFM head is a low-noise Veeco Multimode, which exploits standard optical lever techniques to measure deflections of the cantilever with 0.1 nm precision over a 50 kHz bandwidth. The mechanical stage consists of a stick-slip motor (Attocube) and a piezoelectric translator (PI). The stick-slip motor is moved only at the beginning of the experiment to bring the plate within a few microns from the sphere, while the separation between the two surfaces during the actual experiment is varied with the piezoelectric translator. This translator, which is controlled by a capacitive feedback loop, has been calibrated by the manufacturer against traceable standards. Its resolution is reported to be equal to 50 pm. The mechanical stage and the AFM head are anchored to a 1 dm^3 aluminum block that is maintained at a temperature $\simeq 10 \text{ K}$ above room temperature by means of a feedback controlled heating system. The block is mounted on a commercial active anti-vibration stage (Halcyonics), which is placed inside a 1 m^3 acoustic isolation box. Finally, this box is placed on an optical table inside a temperature controlled

room.

In order to measure the dependence of the electrostatic force between the sphere and the plate as a function of their separation, we apply an oscillating voltage $V = V_{DC} + V_{AC} \sin(\omega t)$. Using Hooke's law and Eq. 2.1, the signal S of the photodetector of the AFM head can be written as

$$S = \gamma \frac{F}{k} = -\frac{\gamma \varepsilon_0 \pi R}{kd^p} \left[(V_0 + V_{DC})^2 + \frac{V_{AC}^2}{2} + 2(V_0 + V_{DC})V_{AC} \sin(\omega t) - \frac{V_{AC}^2 \cos(2\omega t)}{2} \right], \quad (2.2)$$

where k is the spring constant of the cantilever and γ is a parameter that translates cantilever deflection into signal (expressed in V/m). Note that we have added an exponent p to the denominator: our goal is to verify whether $p = 1$ or not. The signal S contains two static components and two periodic components at angular frequencies ω and 2ω . The static components of the signal represent the static deflection of the cantilever, which, as we will show later, is always smaller than 0.2 nm, and will thus be neglected. The two periodic components can be used to fully characterize the electrostatic interaction. For this reason, the photodetector is connected to two lock-in amplifiers operating at frequencies ω (L1) and 2ω (L2), as illustrated in Fig. 2.1. From Eq. 2.2, one can see that the output of L1 is proportional to $V_0 + V_{DC}$. One can thus create a negative feedback loop where L1 generates V_{DC} in such a way that it keeps $V_0 + V_{DC}$ small, as typically done in Kelvin probe force microscopy [40]. The loop gain G of the current experiment varies from 10^3 (at $\simeq 2\mu\text{m}$ separation) to 10^4 (at $\simeq 100\text{nm}$ separation). Because $V_{DC} = -\frac{G}{G+1}V_0$ and $|V_{DC}| < 50\text{mV}$ in all our measurements, the feedback loop certainly compensates V_0 down to $|V_{DC} + V_0| < 50\ \mu\text{V}$. Thus, one can assume $V_{DC} = -V_0$ for all practical purposes. We stress that the purpose of this feedback loop is two-fold: the compensation voltage V_{DC} is measured accurately at all distances and the static deflection of the cantilever is minimized by effectively zeroing the first term of the expansion in Eq. 2.2. As far as L2 is concerned, note that its peak-to-peak value is given by:

$$S_{2\omega} = \frac{\gamma \varepsilon_0 \pi R}{kd^p} V_{AC}^2 \equiv \alpha V_{AC}^2, \quad (2.3)$$

where α is proportional to the curvature of the parabola described by Eq. 2.1, which can be obtained as $S_{2\omega}/V_{AC}^2$. Therefore, by examining the measured values of α as a function of d one can verify whether $p = 1$ or not. To obtain α as a function of d , we start by placing the plate a few micron away from the sphere. We then move the plate towards the sphere in discrete steps. For each position, we measure $S_{2\omega}$ for a properly chosen value of V_{AC} . At first, one might think to simply keep V_{AC} constant during the whole run. However, it

is more convenient to reduce V_{AC} such that $S_{2\omega}$ stays constant as the surfaces approach, because, in this way, the relative random error of α is equal for all separations: $\sigma_\alpha/\alpha = \sigma_{S_{2\omega}}/S_{2\omega}$ (if we assume that the random error on V_{AC} is negligibly small). Therefore, before we move the plate to the next measurement point, we use the values of α measured in the same run at larger separations to estimate the value that α should assume in the next position, and we set the new value of V_{AC} accordingly [†]. This procedure does not by any means introduce systematic errors on α , which is still evaluated as $\alpha = S_{2\omega}/V_{AC}^2$, where $S_{2\omega}$ is the actual value measured by L2. Systematic errors on V_{AC} can also be ruled out, because we calibrated the digitally controlled function generator before starting the experiment.

In the current experiment, L2 has a 24dB/octave low pass filter with a 1 s RC time, and data are acquired with 5 s integration time at every position. We use an $S_{2\omega}$ set-point that corresponds to a peak-to-peak cantilever movement at 2ω of roughly 0.3 nm [‡]. With this set-point, V_{AC} varies between 450 mV at $d \simeq 2 \mu\text{m}$ to 100 mV at $d \simeq 100 \text{ nm}$. This corresponds to a static deflection of the cantilever at $V_{DC} = -V_0$ of roughly 0.15 nm, which is thus negligible. To minimize drifts of the amplitude response $S_{2\omega}$ due to potential changes of the resonance frequency of the cantilever, we work in the quasi-static regime, setting $\omega/2\pi$ to 72.2 Hz [§], which is much smaller than the resonance frequency of the force sensor (1.65 kHz, as obtained with an independent measurement). The total measurement consists of 184 runs over 1050 minutes.

In Fig. 2.2 we show the value of α as a function of the extension of the piezoelectric stage d_{pz} (see Fig. 2.1) for one randomly chosen run. If we neglect the static deflection of the cantilever, the actual separation between the surfaces d is given by $d = d_0 - d_{pz}$, where d_0 is the initial separation, which is *a priori* unknown. To validate whether $p = 1$, we fit the data with an equation of the form

$$\alpha = \frac{\kappa}{(d_0 - d_{pz})^p}, \quad (2.4)$$

where d_0 and $\kappa = \frac{\gamma\varepsilon_0\pi R}{k}$ are free parameters. The fits are performed using standard χ^2 minimization algorithms, for which it is necessary to first estimate the error on the data. This is done by measuring α at a fixed d_{pz} for 120 minutes. The results are shown in Fig. 2.3. The data distribute along a smooth curve that is not constant because of drifts in d_0 and/or κ [¶]. In the inset, we plot a histogram of the relative difference between the data points and

[†]To avoid that data at very large separations influence the estimate of V_{AC} at closer distances, we only use the 8 closest points to estimate the next value of α .

[‡]To determine this value, we first independently determined the value of γ . A description of the technique used to determine γ goes beyond the aim of the paper, and, for the sake of brevity, is omitted. We refer the reader to section 3.3.

[§]This frequency is determined by a Deliyannis-Friend filter in the ω feedback loop.

[¶]Later in the text, we show that the drift in κ is negligible on the scale of Fig. 2.3.

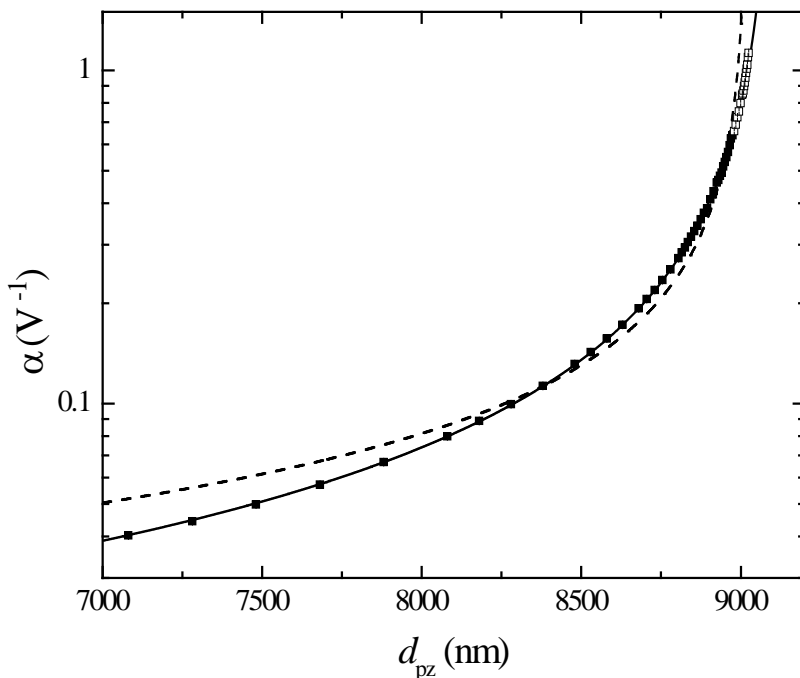


Figure 2.2: Plot of α (see Eq. 2.3) as a function of the position of the piezoelectric translator for run number 107. The error bars on the data are within the dimension of the symbol. Black squares indicate data that are used for the analysis. Open squares are data that are excluded from the analysis. The continuous line shows the fitting curve obtained with elementary electrostatic arguments ($\alpha \propto 1/d$). The dashed line represents the best fit obtained on the basis of the anomalous behavior observed in [38] ($\alpha \propto 1/d^{0.7}$).

the smoothed curve. One can clearly see that α follows a normal distribution with a standard deviation of 0.56%; the relative error in a single measurement of α is thus 0.56%. Note that this error represents an uncertainty of 600 fm in the determination of the root-mean-square motion in response to the varying potential difference V_{AC} . Using this relative error, we repeat the fit three times: letting p as a free parameter, and forcing $p = 1$ (as elementary electrostatic calculations suggest) or $p = 0.7$ (as found in [38]). If p is a free parameter, one obtains $p = 1.005 \pm 0.004$ with reduced χ^2 equal to 1.19. The fit with $p = 1$ gives rise to a comparable value of reduced χ^2 ($\chi^2 = 1.21$). The fit with $p = 0.7$, on the contrary, produces a reduced χ^2 of 411. Our data thus follow the behavior expected from elementary electrostatic arguments. It is important to stress that these values are obtained analyzing all data except those for which $d < 120$ nm (see the open squares of Fig. 2.2). If those data are included, the χ^2 quickly increases. This is not surprising because, at small separations (smaller than $\simeq 120$ nm), the Casimir force bends the cantilever so much that, within the precision of the current experiment, one cannot assume $d = d_0 - d_{pz}$ anymore.

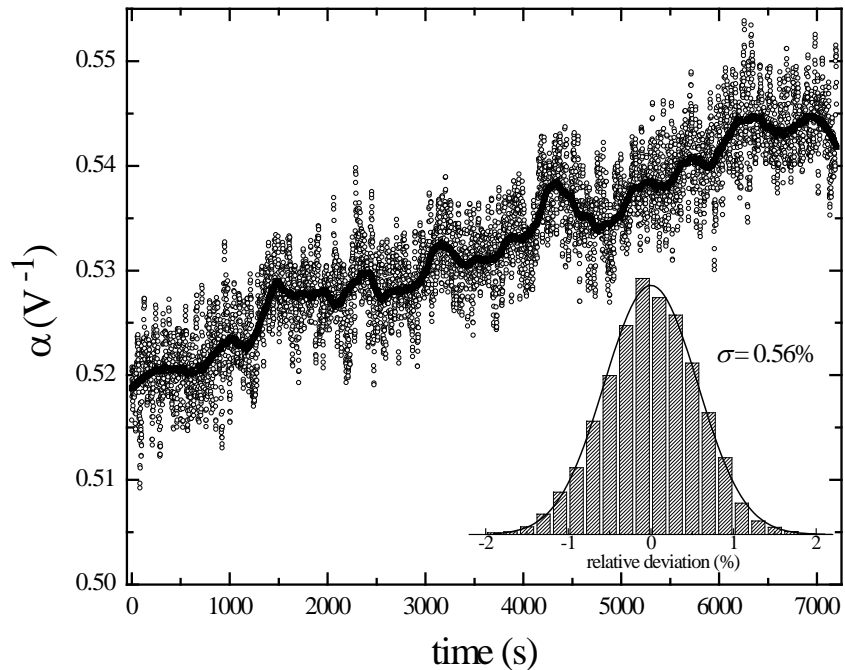


Figure 2.3: Plot of α (see Eq. 2.3) as a function of time for a fixed value of d_{pz} . The thick line represents a smoothed curve that accounts for the drifts in our setup during this measurement. The inset shows a histogram of the relative difference between the data points and the smoothed curve, together with a Gaussian fit.

To make our claim more robust, we fit each single data set with $p = 1$

and analyze the behavior of the reduced χ^2 . For the sake of computational convenience, we rewrite Eq. 2.4 as

$$\frac{1}{\alpha} = \frac{1}{\kappa} (d_0 - d_{pz}). \quad (2.5)$$

To avoid systematic errors due to the bending of the cantilever at small separations, we apply again a mask to the closest $N - 41$ data points, where N is the total number of points in a single run (similar to Fig. 2.2). The relative error on α is so small, that $1/\alpha$ also follows a normal distribution (with 0.56% relative error). The average reduced χ^2 over 182 runs (two runs are outliers with χ^2 values of 4.8 and 2.9) is 1.03, and the χ^2 values are distributed with a standard deviation of 0.23 ^{||}. The anomalous scaling law observed in [38] is thus not a universal behavior.

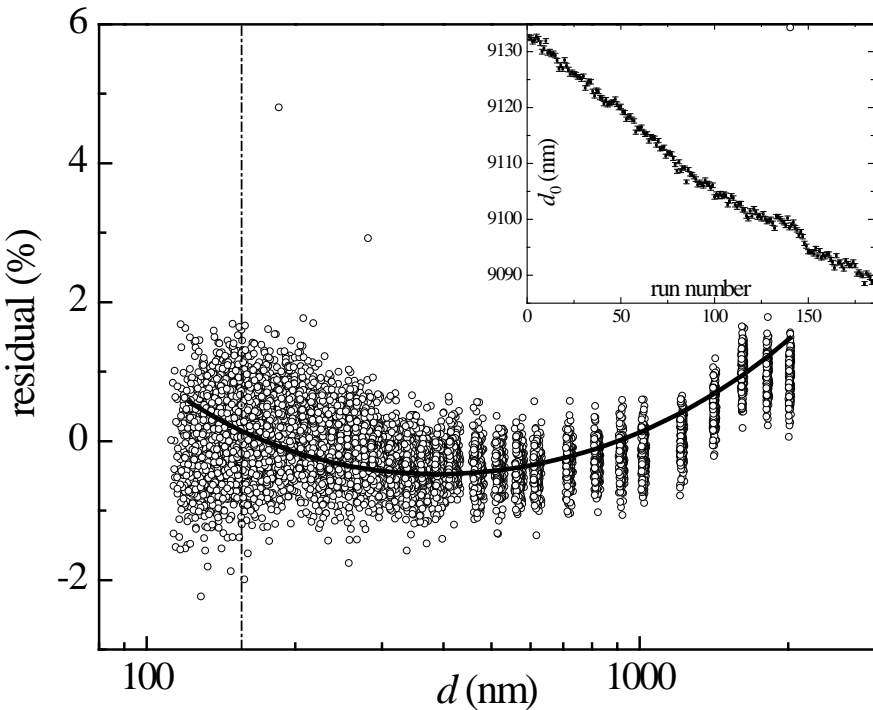


Figure 2.4: Residuals of the fits with $p = 1$ plotted as a function of separation. The continuous line represents the expected deviations due to the use of the proximity force approximation instead of the whole analytical equation. The dashed line indicates the separation at which the data of Fig. 2.3 were taken. Inset: value of the initial separation between the sphere and the plate as a function of run number as obtained by fitting the data on the basis of elementary electrostatic arguments.

Now that the $p = 0.7$ behavior is ruled out, it is interesting to plot the

^{||}Note that the value of the reduced χ^2 for run 107 is actually higher than the average χ^2 of all runs. The data presented in Fig. 2.2 are thus certainly not among the ones that better match the theory.

residuals of the fits with $p = 1$. From this plot, reported in Fig. 2.4, it is evident that our data systematically deviate from the fit, with maximum deviation of $\simeq 1\%$. This behavior is due to the fact that eq. 2.1 is based on the use of the so-called *proximity force approximation* (PFA) [21]. Using the complete analytical equation for the electromagnetic force between a sphere and a plate [55] to calculate the average residual expected from a fit with eq. 2.5 (with κ and d_0 as free parameters), one obtains the continuous line of Fig. 2.4. Note that, although the difference between the complete analytical equation and the PFA goes to zero as separation decreases, Fig. 2.4 does not show this behavior. This is due to the fact that we are fitting a linear function (eq. 2.5) to slightly curved data. From the same figure, one can also see that the random errors at larger separations are actually smaller than that used in the fits (0.56%), which was measured at $d \simeq 150$ nm (see dashed line of Fig. 2.4). This justifies the fact that the fit with eq. 2.1 and $p = 1$ gave $\chi^2 \simeq 1$ even if a not completely correct theoretical model was used.

We want to stress that such an excellent agreement can only be obtained if the experimental apparatus is exceptionally stable. In the inset of Fig. 2.4, we plot the initial separation d_0 obtained from the fits of all 184 runs. The total drift in d_0 is 45 nm over 1050 minutes. This means that our setup drifts only $\simeq 40$ pm/min (compared to 1 nm/min in [36]), or 0.24 nm drift per measurement run (compared to $\simeq 60$ nm per run in [38]). From the fits, we also observe that the other fit parameter κ drifts 1.1% over 1050 minutes. This corresponds to 0.001%/min or 0.006% per run, and is likely due to a change of γ caused by a slow drift of the laser spot over the photodetector of the AFM head. The effects of both drifts are negligible in one measurement run.

The authors of [38] noticed that, in their setup, the voltage needed to minimize the force depends on the separation between the surfaces. In Fig. 2.5 we plot V_{DC} as a function of d for the data set shown in Fig. 2.2, where d_0 was determined by fitting α as a function of d_{pz} with $p = 1$. Also in our measurements, the compensation voltage clearly depends on d , varying by $\simeq 6$ mV over 2 μm . This behavior is reproduced in the other 183 measurement runs. In the inset of the figure, we plot V_{DC} at $d \simeq 275$ nm as a function of run number. Although the drift of V_{DC} during the 1050 minutes of the entire experiment is of comparable magnitude as the dependence on separation for a single run, it is clear that the dependence of V_{DC} on d cannot be caused by a drift of V_{DC} with time. As one can see from the inset of Fig. 2.5, the drift in V_{DC} from one run to the next is certainly much smaller than the difference observed, within one run, as a function of distance (i.e., 6 mV).

Interestingly, the data seem to distribute along a curve that goes like $a \log d + b$ (reduced $\chi^2 = 0.8$). A similar behavior has been recently reported in an experiment between Ge surfaces [56]. A rigorous explanation of the origin of the dependence of V_{DC} on d goes beyond the purpose of this paper. Still, our measurements, together with the results of [56] and [38], suggest that it is

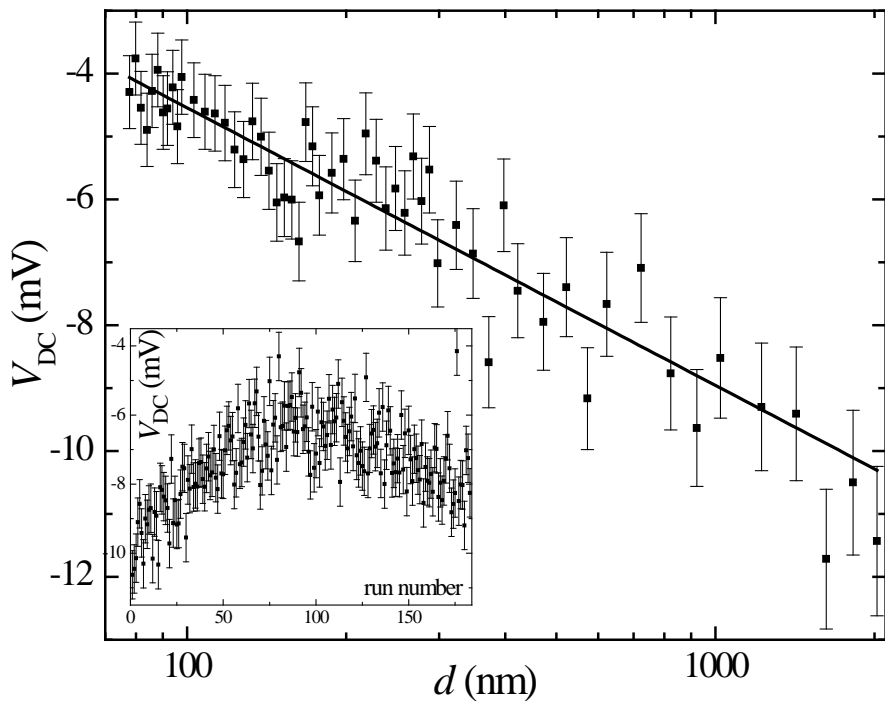


Figure 2.5: Electrostatic compensation voltage as a function of sphere-to-plate separation for run 107. The continuous line represents the best fit with $V_{DC} = a \log d + b$ (reduced $\chi^2 = 0.8$, $a = -4.4 \pm 0.2$ mV, $b = 4.3 \pm 0.6$ mV, d in nm). The initial separation between the sphere and the plate is obtained from the continuous line of Fig. 2.2. Each error bar represents the standard deviation of the gaussian distribution of the 184 values of V_{DC} at that separation. Inset: V_{DC} at $d \simeq 275$ nm as a function of run number.

indeed of fundamental importance to measure V_{DC} for all values of d , as in [38], and, previously, in [32]. Furthermore, since our calibration follows elementary electrostatic arguments, we conclude that, in general, it is not sufficient to check the scaling of α with d to rule out the presence of a distance-dependent V_{DC} .

The authors thank F. Mul, J.H. Rector, R.J. Wijngaarden, and R. Griessen for useful discussions. This work was supported by the Netherlands Organisation for Scientific Research (NWO), under the Innovational Research Incentives Scheme VIDI-680-47-209. DI acknowledges financial support from the European Research Council under the European Community's Seventh Framework Programme (FP7/2007-2013)/ERC grant agreement number 201739.

2.3 Contact potentials in Casimir force setups: an experimental analysis

Abstract – We present an extensive study of the contact potential difference, V_0 , between a gold coated sphere and a gold coated plate kept in air at sub-micron separation. Our data confirms that, in ambient conditions, V_0 depends on both time and separation. We discuss the origin of the time dependence of V_0 and elaborate on its functional dependence on separation, d . Our data strongly support a $\log(d)$ hypothesis, but also show that in air this description is not quite complete. These effects might have important implications in the realm of Casimir force experiments.

^{||}This paper has been published: S. de Man, K. Heeck, R. J. Wijngaarden, and D. Ianuzzi, *J. Vac. Sci. Technol. B* **28**, C4A25 (2010)

2.3.1 Introduction

Measurements of the contact potential difference between conducting surfaces plays a peculiar role in Casimir force[18] experiments. Although in these experiments the actual value of the contact potential is not of direct interest, it has to be accurately counter biased in order to avoid residual electrostatic forces that would otherwise mimic the Casimir effect[26]. It was pointed out recently that in such experiments, where generally a sphere is brought into close proximity of a plate, the contact potential might depend on the separation between the interacting surfaces[38]. This finding was confirmed in an independent experiment[19], where it was also observed that the contact potential varies in time. The latter observation was also reported in [57], in which a torsion balance has been used to emulate the Laser Interferometer Space Antenna (LISA). In another recent experiment between Ge surfaces at small separation[52], again a separation dependent contact potential was measured. All these observations triggered interest in whether one has to take into account the variation of the contact potential in the analysis of Casimir force experiments or not, and which theoretical model should be used to describe the experimental findings[56, 58].

In this paper, we present a series of experiments in which we have investigated the behavior of the contact potential between a sphere and a plate under ambient conditions. Measurements as a function of time seem to indicate that water layers adsorbed at the surfaces play an important role. Measurements as a function of separation reveal a clear dependence that we hope will trigger the development of new theoretical models for the description of the contact potential in Casimir force setups.

2.3.2 Experimental details

Our experimental setup is designed to measure the Casimir force between a sphere and a plate at sub-micron separation. The setup can simultaneously measure the electrostatic force, the Casimir force, the hydrodynamic force, and the contact potential between the two interacting surfaces[20]. To determine the contact potential, we employ a modified Kelvin probe force microscopy[40] scheme. The sphere is attached to an Atomic Force Microscope (AFM) cantilever and mounted inside an AFM head to detect the bending of the cantilever in response to external forces. A planar sample is mounted in front of the sphere on a piezoelectric translator to vary the separation between the two surfaces. We apply an AC potential difference between the surfaces at a low frequency (much below the free mechanical resonance frequency of the probe) and use a lock-in amplifier to detect the response of the cantilever at that frequency. The output of the lock-in amplifier closes a negative feedback loop that compensates the contact potential[19]. The contact potential can then be recorded as a function of time at fixed separation or as a function of

the distance between the interacting surfaces.

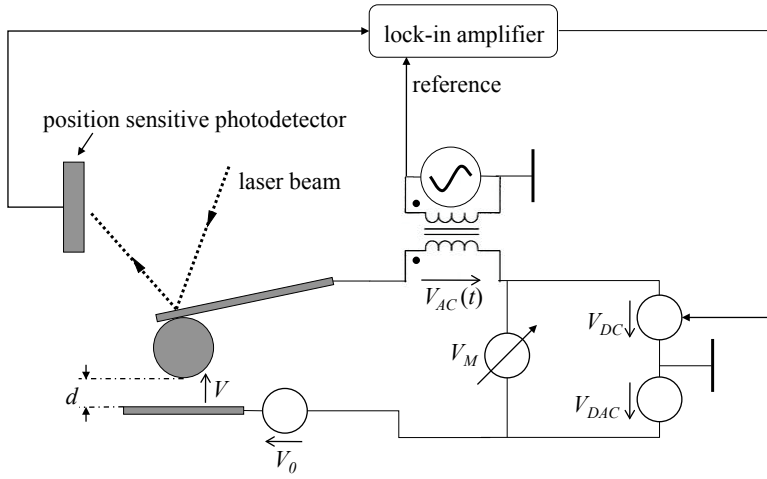


Figure 2.6: Schematic drawing of the electronic circuit of the contact potential measurement. See text for details.

More in detail, a 100 μm radius polystyrene sphere is attached to a 1 N/m AFM cantilever. The probe is then coated with a Ti adhesion layer followed by a 100 nm Au film. The planar sample is a polished sapphire substrate coated in the same deposition run as the sphere. The probe is mounted inside a Veeco Multimode AFM head. The flat sample is anchored to a capacitive feedback controlled piezoelectric scanner in front of the sphere (see Fig. 2.6), which allows one to accurately vary the separation between the sphere and the plate. For a detailed description of the calibration procedure that translates relative piezo displacements into absolute surface separation, we refer the reader to [19].

The sphere and the plate are electrically isolated from the setup, and are connected to a separate electronic circuit as depicted in Fig. 2.6. The potential difference across the interacting surfaces, V , is equal to the sum of the contact potential, V_0 , a low frequency (72.2 Hz) AC voltage, $V_{AC}(t)$, the counter bias voltage generated by the lock-in amplifier, V_{DC} , and a computer controlled DAC power supply, V_{DAC} . V_0 represents the net electrostatic potential caused by the contact potential difference between the two interacting surfaces. $V_{AC}(t)$ is supplied via a transformer to eliminate any spurious contribution that may otherwise arise from DC drift in the output voltage of the function generator.

V_{DAC} allows the lock-in amplifier to work in its optimal range (i.e. close to zero output voltage), as will be explained more in detail later in the text. A voltmeter (ADC with buffer amplifier), V_M , is used to measure the total DC counter bias $V_{DC} + V_{DAC}$. All our experiments are conducted in air at ambient pressure and room temperature.

We will now explain in detail the working principle of the counter biasing negative feedback loop that we use to measure the contact potential. The electrostatic force between a sphere and a plate for very small surface separations, d , can be obtained with the proximity force approximation[41]:

$$F(d) = 2\pi R u_{pp}(d), \quad (2.6)$$

where R is the radius of the sphere ($R \gg d$) and $u_{pp}(d)$ is the potential energy between two parallel plates per unit area. The potential energy per unit area for a parallel plate capacitor is

$$u_{pp}(d) = -\frac{1}{2} \frac{CV^2}{A} = -\frac{1}{2} \frac{\varepsilon_0 V^2}{d}, \quad (2.7)$$

where V is the potential difference between the plates, ε_0 is the permittivity of vacuum and A is the plate area. The minus sign comes from the fact that, under the condition of fixed applied voltage, the potential energy is the sum of the electric field energy and the work done by the power supplies [59]. Eq. 2.6 thus reads

$$F(d) = -\frac{\varepsilon_0 \pi R V^2}{d}. \quad (2.8)$$

From Kirchhoff's loop rule, we obtain $0 = V + V_{AC}(t) + V_{DC} + V_{DAC} + V_0$ (see Fig. 2.6). Consequently

$$F(d) = -\frac{\varepsilon_0 \pi R (V_0 + V_{AC} \cos(\omega t) + V_{DC} + V_{DAC})^2}{d}, \quad (2.9)$$

where we have substituted $V_{AC}(t) = V_{AC} \cos(\omega t)$. It is evident that Eq. 2.9 contains a single AC component at ω , namely

$$F_\omega(d) = -\frac{2\varepsilon_0 \pi R}{d} (V_0 + V_{DC} + V_{DAC}) V_{AC} \cos(\omega t). \quad (2.10)$$

Since the frequency of our AC voltage (72.2 Hz) is much lower than the resonance frequency of the probe (2 kHz), the cantilever can easily follow the modulation and the response is in phase and given by Hooke's law. The output of the AFM optical triangulation readout (see Fig. 2.6) at radial frequency ω is thus

$$S_\omega(d) = -\frac{2\gamma \varepsilon_0 \pi R}{kd} (V_0 + V_{DC} + V_{DAC}) V_{AC} \cos(\omega t). \quad (2.11)$$

where γ is the sensitivity of the optical lever readout and k is the spring constant of the cantilever (1 N/m). The root-mean-square of this signal is

measured by the lock-in amplifier, amplified with gain G , and outputted as V_{DC} :

$$V_{DC} = -\frac{2G\gamma\varepsilon_0\pi RV_{AC}}{\sqrt{2}kd}(V_0 + V_{DC} + V_{DAC}). \quad (2.12)$$

Let us denote the loop gain $\frac{2G\gamma\varepsilon_0\pi RV_{AC}}{\sqrt{2}kd} = G_L$; its value varies from 10^3 to 10^4 in a typical experiment[19], but could be made much higher by increasing V_{AC} . Then Eq. 2.12 can be simplified to

$$V_{DC} = -\frac{G_L}{G_L + 1}(V_0 + V_{DAC}). \quad (2.13)$$

From Eq. 2.13 one can see that, as mentioned earlier, V_{DAC} can be adjusted to keep the output of the lock-in amplifier, V_{DC} , small. Rewriting Eq. 2.13, we see that

$$V_0 = -(V_{DC} + V_{DAC}) - \frac{V_{DC}}{G_L} = -V_M - \frac{V_{DC}}{G_L}, \quad (2.14)$$

where V_M is the readout of the voltmeter as shown in Fig. 2.6. Since we kept $|V_{DC}| < 50$ mV and $G_L > 3 \cdot 10^3$ in all experiments presented here, V_M measures directly the contact potential V_0 up to a systematic offset < 17 μ V (this offset does depend on d though, as G_L increases with decreasing d). Because this offset is very small, we assume $V_M = -V_0$ in the rest of the paper.

It is noteworthy that, as long as $|V_{DC}/G_L| \ll |V_M|$, any drift in V_{DAC} or in the output amplifier of the lock-in is automatically compensated by the feedback mechanism. Therefore, any variation we observe in V_M must be caused by changes in V_0 .

It is interesting to note that we feed the output of the lock-in amplifier directly into the electronic circuit of Fig. 2.6, instead of using a PID controller. When the lock-in is operated with a 6dB/octave filter roll-off, then the single time constant in the feedback loop ensures stability. However, due to the large loop gain G_L , one has to equip the lock-in amplifier with a rather large external time constant τ_{RC} , because the effective time constant of the loop is τ_{RC}/G_L . To minimize noise in V_{DC} , we typically use a τ_{RC} on the order of 10^3 seconds.

2.3.3 Results and discussion

In this section we present two sets of contact potential data acquired during several months of force measurements using gold surfaces, and we discuss their dependence on time and surface separation.

Time dependence

The first data set contains 1944 measurement runs in which the surface separation is changed from $d = 1.1$ μ m to $d = 60$ nm in 50 steps. The data were collected in a continuous experiment from a Friday afternoon until Monday

afternoon 10 days later (the relevance of this detail will become clear). In Fig. 2.7 we plot V_0 at a particular value of d ($d = 275$ nm) as a function of run number (black squares). The white continuous line represents a smoothed curve that indicates the trend of the drift in V_0 . It is evident that from the start of the measurement it takes a couple of days until the value of the contact potential has stabilized. This rather slow convergence is compatible with the observations in [57]. After this initial settling at roughly run 500, V_0 develops an oscillatory behavior with a 24 hour periodicity, except for the weekend where the oscillation is absent. On Monday morning, however, it clearly sets in again. V_0 data at other separations show exactly the same temporal behavior.

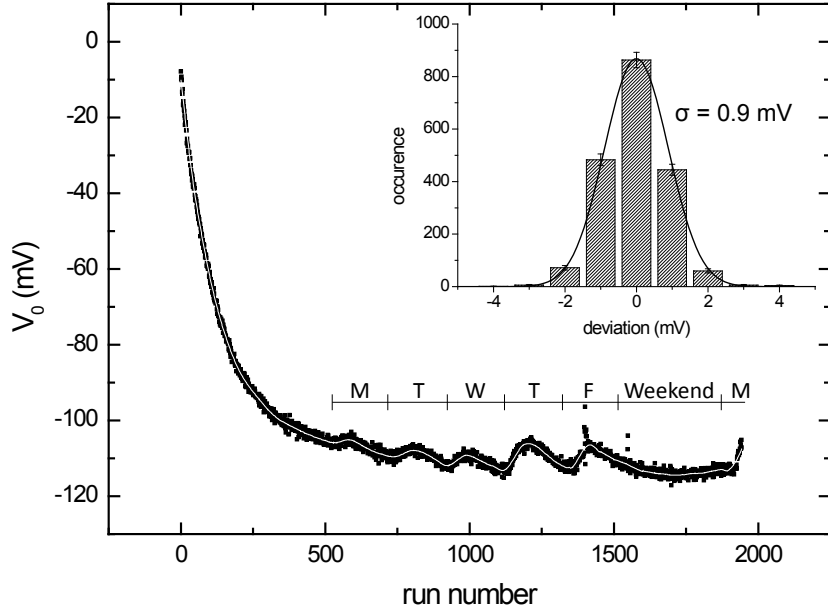


Figure 2.7: Measurements of the contact potential V_0 between two gold surfaces separated by 275 nm during 10 consecutive days as a function of measurement run number (black squares). The continuous white line represents the same data, but smoothed with a 100 points moving window second order Savitsky-Golay filter. After an initial stabilization period V_0 starts to oscillate with a 24 hour rhythm, except for the weekend. Inset: Histogram of the deviation between the data points and the smoothed curve, fitted with a Gaussian. The best fit has a standard deviation of 0.9 mV.

We want to emphasize that our measurements of V_0 are gathered in a setup that works in air at ambient conditions. Our force apparatus is actively stabilized at 300 K and placed inside an acoustic isolation box. Inside the box, several silica gel packs help to lower the relative humidity of the air. Just before we start a measurement series, the acoustic isolation box has been open

for some time to allow for sample placement and AFM optical lever alignment. After closing the acoustic isolation chamber, the air inside the box is getting warmer (because of the heating due to the temperature stabilization system) and less humid (because of the silica gel packs). We speculate that the slow decrease in V_0 in the first couple of days is caused by a change in the thickness and composition of the adsorbed water films covering our surfaces, as a consequence of the constant increase of temperature and decrease of humidity. After 2 days, the air inside the box reaches an equilibrium and the exponential behavior ceases.

The daily oscillation of roughly 10 mV that we observe at a later stage must somehow be caused by a change in the temperature of the laboratory, which is oscillating strongly in winter (the central heating system of the building is switched off during the nights and weekends and isolation is poor). Voltage variations in the electrical leads and connections due to the Seebeck effect are unlikely, simply because the oscillations are too big: typical thermo-couple coefficients are around tens of $\mu\text{V}/\text{K}$ and can thus never account for more than 1 mV of V_0 oscillation. However, the variation of the temperature of the laboratory slightly alters the temperature of the air inside the box because the box does not provide sufficient thermal isolation. This temperature variation of the air that is in contact with the investigated surfaces might induce changes in the properties of the adsorbed water layers.

Separation dependence

In [19], we investigated the dependence of the V_0 data on separation for one specific measurement run out of a measurement series containing 184 runs. It is interesting to analyze more deeply the data presented in [19], and assess the separation dependence for all measurement runs. First, in Fig. 2.8, we plot V_0 versus d for another, randomly chosen, single run. The straight line is the best fit of a function $V_0(d) = a \log(d) + b$ to the data, resulting in a reduced χ^2 of 0.93. To understand whether we can extract some systematic properties of V_0 from the 184 data sets, we fitted the function $V_0(d) = a \log(d) + b$ to all of them. In inset a, we plot the offset fit parameter, b , as a function of time (we have removed run 176 because it is an outlier). In this data there is not such a strong drift in V_0 with time as in Fig. 2.7, because the acoustic isolation box was already closed for quite some time before the data of Fig. 2.8 were gathered; the initial settling of V_0 had already taken place before the first run. In inset b of Fig. 2.8, we plot the slope a of the fits as a function of run number, where the error bars denote the errors on the fit parameter as propagated through the fit procedure. It seems that a does not depend on time. If we fit a constant to these data, though, we obtain a reduced χ^2 of 1.4, which means that it is quite unlikely that the model is correct given the fact that we have 182 degrees of freedom. Therefore, we have either underestimated the

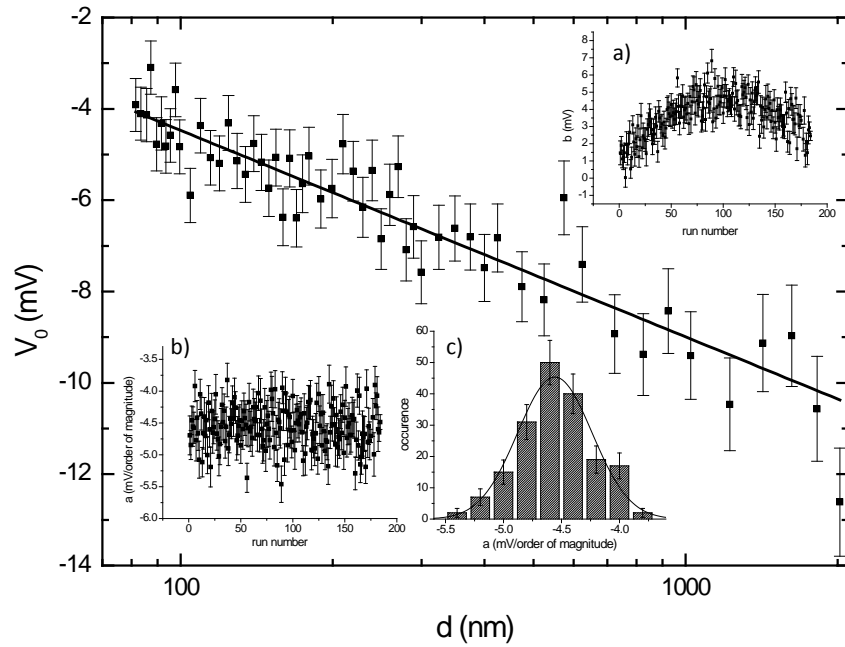


Figure 2.8: Re-analysis of the data published in [19]. The main figure shows the distance dependence of V_0 of a single measurement run from the 184 data sets of [19]. The line indicates the best fit with a logarithmic function $V_0(d) = a \log(d) + b$ (reduced $\chi^2 = 0.93$, $a = -4.5 \pm 0.3$ mV/order of magnitude, $b = 4.6 \pm 0.6$ mV and d in nm) **a**, Plot of the variation in time of the fit parameter b . **b**, Plot of the time dependence of the fit parameter a **c**, Histogram of all obtained values for a . The best fit with a Gaussian resulted in $a = -4.6 \pm 0.6$ mV.

error on a or there is a hidden dependence of V_0 on time. The first option is not really feasible, because the reduced χ^2 values of the logarithmic fits distributed neatly around 1, and the error on a is just calculated from this fit procedure. The second hypothesis would indicate that there is a dependence of a on run number, albeit in a random way (there is no apparent functional dependence visible in Fig. 2.8 a). We speculate that such a random contribution to the V_0 scaling properties may be related to the actual measurement procedure. Namely, during a measurement run, where we start at large separation and decrease d in successive steps, we reduce the excitation voltage V_{AC} to keep the electrostatic force constant (see [19]). At the end of the run we retract the piezoelectric stage quickly while the V_{AC} excitation voltage is still at the lowest setting (as we were at the closest point). After a few seconds, the next run is started and the V_{AC} value is increased again to reach the same electrostatic force as we used in the run before. This procedure leads to a significant drop in electrostatic field strength in between measurement runs. It could be that this fast change of field strength causes the adsorbed water layer and its contaminants to rearrange on the surfaces. Fig. 2.8 c presents all the obtained values of a in a histogram. The Gaussian fit resulted in a value for a of -4.6 ± 0.6 mV/order of magnitude. It is interesting to note that the values of a follow a normal distribution, which then indicates that, although there is a random run-to-run variation in a (by which we mean a *real* variation and not one that merely follows from the statistical uncertainties in the V_0 measurements), this run-to-run randomness of a follows a normal distribution.

To complete the analysis, it is interesting to check whether the data presented in Fig. 2.7 also depend on the separation between the interacting surfaces. In order to assess the precision of our data, we have smoothed the V_0 data with a second order Savitsky-Golay filter with a 100 points moving window and plotted the resulting curve as the white line in Fig. 2.7. Then we have created a histogram of the deviations between the actual data and the smooth line and fitted a Gaussian function with the standard deviation as the only fit parameter, as shown in the inset of Fig. 2.7. The resulting standard deviation is 0.9 mV, which is thus the statistical error in a single V_0 measurement at $d = 275$ nm. Because the loop gain of our negative feedback loop depends on separation, the precision in the measurement of V_0 is separation dependent: the precision increases when the separation decreases. Therefore, we have repeated the described procedure for 5 other values of d (covering the entire measurement range) and then fitted the size of the statistical error as a function of separation with an exponential that seemed to describe the general trend well. In the continuing analysis, we can now use this fit function to obtain the statistical error in V_0 at any separation within the analyzed range.

Similarly to Fig. 2.8, we plot the contact potential versus the surface separation for a randomly chosen run (run 1000) on a semi-logarithmic scale in Fig. 2.9. The continuous line is a fit to the data assuming a $V_0 = a \log(d) + b$

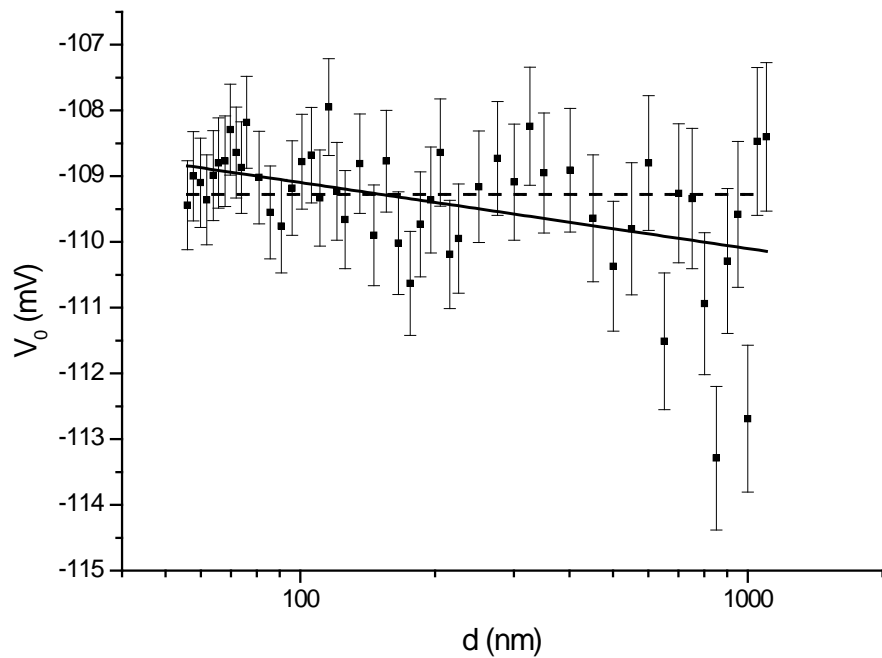


Figure 2.9: Contact potential V_0 as a function of surface separation d for run 1000 from the data set of Fig. 2.7. The continuous line represents the best fit with a function of the form $V_0(d) = a \log(d) + b$ (reduced $\chi^2 = 0.93$, $a = -1.0 \pm 0.3$ mV/order of magnitude, $b = -107.1 \pm 0.7$ mV and d in nm). The dashed line shows the best fit for a separation independent V_0 hypothesis (reduced $\chi^2 = 1.13$ and $V_0 = -109.3 \pm 0.1$ mV).

functional dependence (reduced $\chi^2 = 0.93$), whereas the dashed line assumes simply a constant contact potential (reduced $\chi^2 = 1.13$). Although the reduced χ^2 values of both fits are quite close to 1, one can see by eye that the residuals related to the dashed fit show a systematic behavior for large d , indicating that a constant contact potential does not model the data well. The residuals belonging to the $\log(d)$ behavior are clearly more random, but it would be quite bold to claim that the model is correct. A better formulation would be to state that with the relatively big statistical error compared to the total variation of V_0 in Fig. 2.9, we cannot exclude the logarithmic dependence on separation.

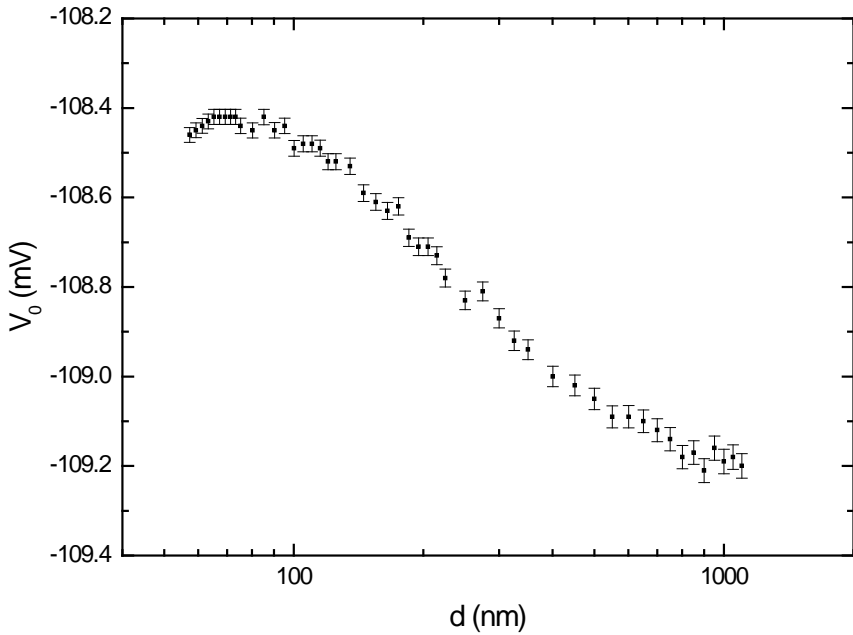


Figure 2.10: Contact potential V_0 as a function of surface separation d , obtained by averaging all but the first 250 runs from the data set of Fig. 2.7.

It is thus clear that an improvement in the precision of V_0 could lead to more conclusive statements regarding its dependence on separation. Since the data were acquired during more than a week, there is ample room to employ averaging procedures. We have therefore averaged the last 1694 measurement runs and plotted the resulting mean V_0 values in Fig. 2.10. We have excluded the first 250 runs from the averaging procedure because of their strong drift (see Fig. 2.7). Although the total variation in V_0 is of course still small at a little less than 1 mV, the high precision in the mean values of V_0 reveals a definite trend in the data**. For $d > 100$ nm, V_0 seems to scale logarithmically

**In this experiment, G_L varies from $4.3 \cdot 10^3$ at $d = 1 \mu\text{m}$ to $1.6 \cdot 10^4$ at $d = 60 \text{ nm}$.

with separation, in agreement with the observations in [38] and [19]. For $d < 100$ nm, however, the trend is clearly altered. We would therefore like to conclude that in these experiments there is certainly a logarithmic contribution in the function $V_0(d)$, but there are definitely other components too.

2.3.4 Conclusions

We have reported systematic measurements of the contact potential difference between a gold coated sphere and a gold coated plate kept in air at sub-micron separation. Our data confirm that the contact potential in Casimir force experiments can depend on both separation and time, and seem to indicate that water layers on the interacting surfaces play an important role in the electrostatic interaction between conducting surfaces in ambient conditions. We hope that our findings will trigger new theoretical investigations on the behavior of contact potentials in Casimir force experiments.

Acknowledgments

The authors thank J. H. Rector, F. Mul, and R. Griesssen for useful discussions, and the ESF Research Network CASIMIR for providing visit grants. This work was supported by the Netherlands Organisation for Scientific Research (NWO), under the Innovative Research Incentives Scheme VIDI-680-47-209. D.I. acknowledges financial support from the European Research Council under the European Community's Seventh Framework Programme (FP7/2007-2013)/ERC grant agreement 201739.

Therefore, the systematic error in V_0 varies from < 12 μ V to < 3 μ V with $|V_{DC}| < 50$ mV (see Eq. 2.14). The effect of this systematic error can thus at most be a tilt in the data of ± 9 μ V over the whole d range, which is still negligible compared to the observed variation in V_0 .

Chapter 3

Halving the Casimir force

3.1 Introduction

The strength of the Casimir interaction depends only on the separation between the objects and the dielectric properties of their surfaces and the intervening medium. As long as one does not work in liquids, the dielectric properties of the medium are essentially equal to those of vacuum, and one can only alter the interaction strength by tuning the material properties. To weaken the force, one has to use material properties that do not impose such strong boundary conditions on the electromagnetic quantum fluctuations in the gap. It is thus necessary to use materials that are not electrically conductive over a wide part of the electromagnetic spectrum. On the other hand, however, it would not make much sense to use insulators, because, although the Casimir force is supposed to be small, electric forces generated by trapped charges on the surfaces would be so strong that the total force between the objects would be much larger than the Casimir force between metals. Therefore, an ideal material would be DC conductive enough to prevent charge accumulation, but transparent enough for infrared and optical frequencies to significantly reduce the Casimir interaction. In section 3.2 we describe an experiment that shows that by using a transparent conductive oxide, typically used for touch screens in semiconductor industry, one can halve the Casimir force with respect to the gold-gold interaction.

In section 3.3, we expand the description of the experiment presented in section 3.2, and discuss in full detail the experimental technique and characterization of the samples. This section also treats the experimental errors and data analysis, as well as a new method to determine the spring constant of the force sensor using the fourth harmonic of the electrostatic excitation voltage at ω_1 . This section is the most complete description of our experimental setup, and can be used as a reference for future use. Concerning the experimental details of the residual potential compensation circuit, the best description is in section 2.3.

3.2 Halving the Casimir force with Conductive Oxides

Abstract – The possibility to modify the strength of the Casimir effect by tailoring the dielectric functions of the interacting surfaces is regarded as a unique opportunity in the development of Micro- and NanoElectroMechanical Systems. In air, however, one expects that, unless noble metals are used, the electrostatic force arising from trapped charges overcomes the Casimir attraction, leaving no room for exploitation of Casimir force engineering at ambient conditions. Here we show that, in the presence of a conductive oxide, the Casimir force can be the dominant interaction even in air, and that the use of conductive oxides allows one to reduce the Casimir force up to a factor of 2 when compared to noble metals.

This paper has been published: S. de Man, K. Heeck, R. J. Wijngaarden, and D. Iannuzzi, *Phys. Rev. Lett.* **103**, 040402 (2009). It was highlighted in P. Ball, *News and Views*, *Nature Materials* **8**, 705 (2009).

The mechanical parts of Micro- and NanoElectroMechanical Systems (MEMS and NEMS) are often designed to work at separations where the Casimir effect [18] might play a relevant role [1–4]. It is thus commonly believed that, if one could suitably engineer the strength of the Casimir force, unprecedented opportunities would come available for the development of conceptually new MEMS and NEMS [5–7, 14]. The most simple approach to tailor the Casimir force is to properly choose the materials of which the interacting surfaces are made. According to the Lifshitz theory [23], the interaction between two objects depends on their dielectric functions. Transparent dielectrics, for example, attract less than reflective mirrors. This property may be used to reduce the Casimir attraction whenever the design requires a smaller short range interaction. It is however fair to say that, for the vast majority of applications, MEMS and NEMS operate in air, where surfaces tend to accumulate trapped charges. Those charges give rise to a strong electrostatic interaction that cannot be compensated by a counterbias voltage and that typically overcomes the Casimir force. It is thus difficult to imagine that the Casimir force can play an important role in MEMS and NEMS operating in air, unless all surfaces are coated with noble metals to reduce the forces due to surface charges to negligible levels. In that case, however, there is not much room to tune the strength of the Casimir interaction because the diversity in the dielectric functions of different metals is simply not large enough [30]*. As a matter of fact, to date, there is no experiment that shows that, in air, the Casimir force can still be tuned significantly while remaining the dominant interaction mechanism.

In this Letter we present a precise measurement of the Casimir force between a gold coated sphere and a glass plate coated with either a thick gold layer or a highly conductive, transparent oxide film. The experiment was performed in air, and no electrostatic force due to residual trapped charges was observed over several weeks of measurements in either case. The decrease of the Casimir force due to the different dielectric properties of the reflective gold layer and the transparent oxide film resulted to be as high as $\simeq 40\% - 50\%$ at all separations (from $\simeq 50$ to $\simeq 150$ nm). Our experiment shows that, in the presence of a conductive oxide layer, the Casimir force can still be the dominant interaction mechanism even in air, and indicates that, whenever the design might require it, it is possible to tune the Casimir attraction by a factor of 2.

Our experimental set-up is designed to perform precise measurements of surface forces between a $100\ \mu\text{m}$ radius sphere and a plate as a function of their separation (see Fig. 3.1 and [19]). The sphere is glued onto the hanging end

*An unsuccessful attempt to change the Casimir force in gas is reported in [32]. $\simeq 1\%$ tunability of the Casimir force in vacuum was shown in [60]. $\simeq 20\%$ tunability of the Casimir force was observed in [33]; this method is not practical, because the interaction strength strongly varies on the local thickness of the film (see [36]). $\simeq 30\%$ variations of the Casimir force were observed in [61]; also this strategy is not practical for MEMS in air, because the passivation layer is not stable under atmospheric conditions.

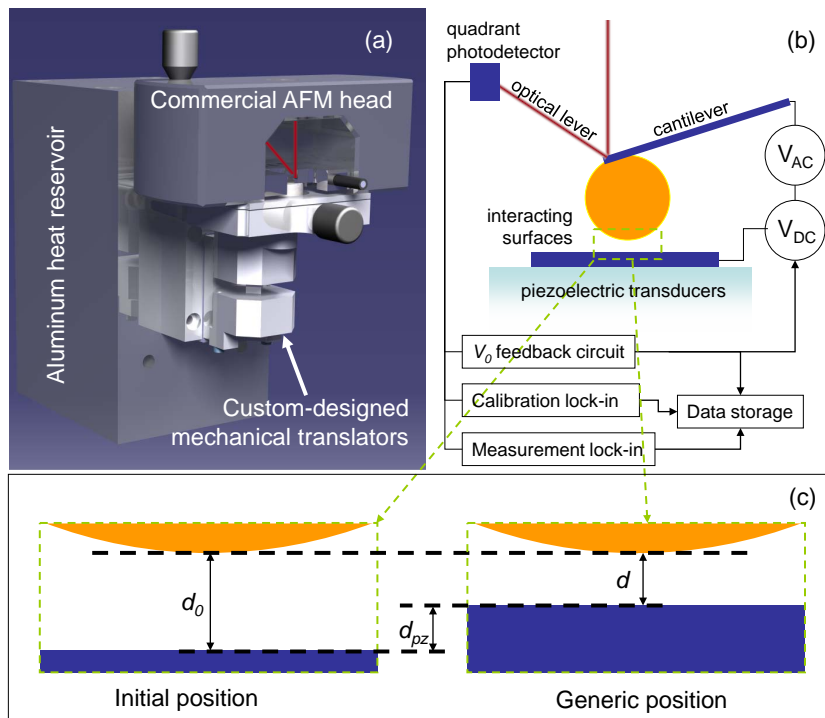


Figure 3.1: **a**, Drawing of the experimental set-up. **b**, Schematic representation of the working principle of the experimental technique. **c**, Definition of d_0 (initial separation), d_{pz} (movement of the piezoelectric stage), and d (separation between the two surfaces).

of a micromachined cantilever (spring constant ≈ 1 N/m, resonance frequency (with the sphere attached) ≈ 1.9 kHz). The plate is mounted on a capacitive feedback controlled piezoelectric transducer that allows one to accurately vary the separation between the sphere and the plate in discrete steps. Any force acting between the two surfaces results in a bending of the cantilever that is detected by the optical lever of a commercial Atomic Force Microscope (AFM) head [†]. The set-up is kept at a fixed temperature to reduce mechanical drifts and is placed on an active anti-vibration stage inside an acoustic isolation box to decouple the force sensor from external vibrations.

Precise Casimir force measurements typically require careful analysis of three crucial issues. First, even when both the sphere and the plate are coated with metallic films, there might still exist an electrostatic potential difference V_0 between the two surfaces that gives rise to a residual electrostatic force. This force must be actively canceled by counter biasing V_0 with an externally applied voltage. Second, although the relative displacements of the piezoelectric transducer that moves the plate, d_{pz} , are precisely controlled, the separation between the two interacting surfaces at the start of the measurement, d_0 , is *a priori* unknown (see Fig. 3.1). Therefore, the absolute separation $d = d_0 - d_{pz}$ has to be obtained from a calibration procedure. Third, the electronic signal coming out of the AFM head must be converted into force. It is thus necessary to calibrate the instrument with a controlled force. To address these problems, we have designed a measurement technique that allows one to simultaneously: (i) compensate for the residual potential, (ii) calibrate the set-up, and (iii) measure the Casimir force (see [19] and section 3.3). In a nutshell, in each calibration/measurement run the plate is moved in discrete steps from d_0 to a minimum value of d (just before contact with the sphere). A calibrated AC electrostatic potential is applied between the sphere and the plate at a frequency ω_1 much lower than the resonance frequency of the force sensor ($\frac{\omega_1}{2\pi} = 72.2$ Hz). This AC excitation is used to drive a feedback circuit that compensates for the residual voltage V_0 , and, simultaneously, generates an electrostatic force that makes the cantilever oscillate at $2\omega_1$. The amplitude of the oscillations, measured with a lock-in amplifier (calibration lock-in in Fig. 3.1b), are recorded as a function of d_{pz} , and are then used to calibrate the instrument and extract d_0 . At the same time, a transducer mechanically coupled to the piezoelectric translator makes the plate move around d_{pz} with an amplitude of 3.85 ± 0.08 nm at a frequency ω_2 , which is again much lower than the resonance frequency of the force sensor ($\frac{\omega_2}{2\pi} = 119$ Hz) [‡]. In the presence of a force that depends on separation (e.g., the Casimir force), the cantilever bends in phase with the modulation of d . The amplitude of the in-phase oscillation,

[†]Measurements of surface forces between a sphere and a plate with an AFM were first reported in [34]. Its utilisation for large range forces between metals was first introduced in [35].

[‡]A similar technique was introduced in [62].

measured with another lock-in amplifier (measurement lock-in in Fig. 3.1b), is proportional to the derivative of the force with respect to d . Furthermore, the presence of the cushion of air between the two surfaces gives rise to a hydrodynamic force that depends on the velocity with which the plate moves. The signal produced by this force manifests itself at the same frequency at which d is modulated, but with a phase rotated by 90 degrees. This contribution does not influence the output of the in-phase component and can be measured independently with the same lock-in amplifier. The integration times of the lock-in amplifiers are 8 s for every value of d_{pz} . A typical measurement run consists of $\simeq 50$ d_{pz} set-points in the measurement range $50 < d < 1100$ nm, and takes roughly 7 minutes. The cantilever responses to the modulations at ω_1 and ω_2 are < 80 pm (root-mean-square) during the entire experiment. All force measurements are performed in air at atmospheric pressure, temperature 300 K, and 29% relative humidity.

In this Letter we present two experiments performed with the same sphere and two different plates. The sphere is a polystyrene sphere with nominal radius 100 μm coated with a Ti adhesion layer followed by a 100 nm Au film (surface roughness 3.8 nm RMS). The plate used in the first experiment is a polished sapphire substrate coated with a metallic film similar to the one deposited on the sphere (surface roughness 0.8 nm RMS). The plate used in the second experiment is a float glass substrate with a 190 nm Indium Tin Oxide (ITO, $\text{In}_2\text{O}_3:\text{Sn}$) sputtered thin film on top (PGO CEC010S, typically $8.5 \Omega/\square$, or, equivalently, $\rho = 1.6 \cdot 10^{-4} \Omega\text{cm}$, total surface roughness 4 nm RMS). We have measured the reflection and transmission spectra of both plates in the wavelength range $180 \text{ nm} < \lambda < 2.5 \mu\text{m}$, and observed that the optical properties of our films are in agreement with the literature [63, 64].

Fig. 3.2a presents measurements of the force between the sphere and the plates coated with either Au or ITO [§]. The experimental data represent the spatial derivative of the total force (normalized by the sphere radius R), which is the sum of the Casimir interaction, a Coulomb interaction induced by the presence of trapped charges (if any), and an electrostatic attraction due to the AC calibration potential. The strength of the latter can be estimated from the simultaneous calibration procedure (see section 3.3). From Fig. 3.2, it is evident that this electrostatic contribution, which is anyway equal in both experiments (within 2%), is small compared to the total force signal. The black lines in Fig. 3.2a are computations of the Casimir force using the Lifshitz theory [41] with dielectric functions calculated as in [64] (for ITO) and [65] (for Au); the electrostatic force due to the calibration potential is added to the theory in order to compare with the raw data. The calculation of the Casimir

[§]Our estimate of d_0 relies on the *proximity force approximation* [41], which is only valid for $d \ll R$. This assumption is not entirely correct in the probed separation range [19] and results in a systematic error in d_0 of $\simeq 1.4$ nm. Still, the corresponding underestimate of the separation is equal for both Au-Au and Au-ITO, and can thus be neglected in the comparison.

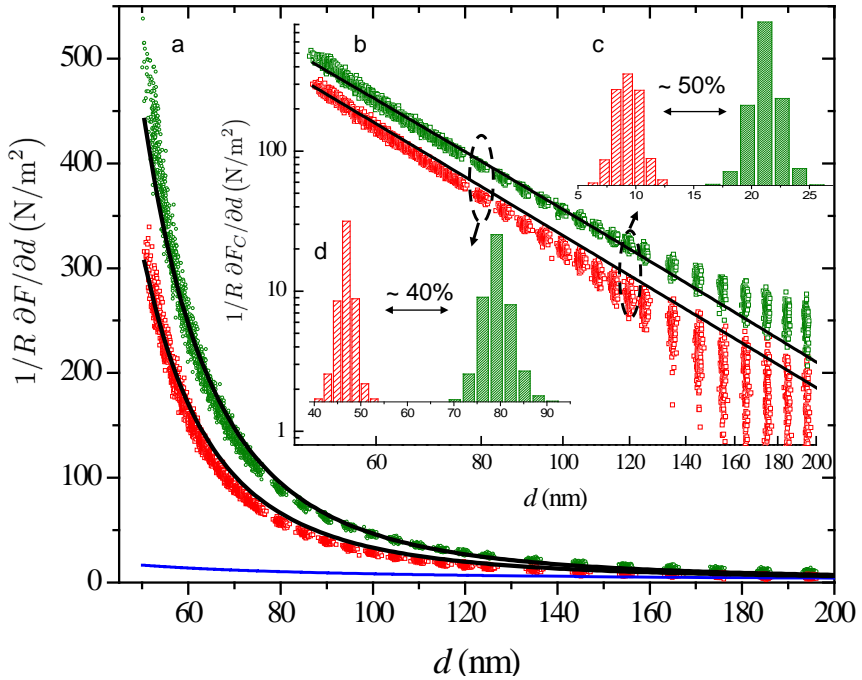


Figure 3.2: **a**, Spatial derivative of the total force as a function of absolute surface separation for the Au-Au (green squares) and Au-ITO (red squares) interactions for randomly chosen subsets of the data (150 out of 580 for both cases). The blue line represents the derivative of the electrostatic force caused by the simultaneous calibration procedure (common to both the gold and ITO measurements). The black lines indicate the calculated Casimir forces with the electrostatic background added. **b**, Spatial derivative of the Casimir force, with the electrostatic background subtracted from the data. The black lines correspond to the calculations of the Casimir force. **c**, Histograms of 580 force measurements for Au-Au and Au-ITO at $d = 120$ nm. **d**, Same as c, but for $d = 80$ nm.

force should only be considered approximate, because the dielectric functions of the samples are not known precisely [66], and no surface roughness corrections are applied. Still, the agreement between the calculation and the data shows that the Casimir effect largely dominates any Coulomb interaction that would have been otherwise observed in the presence of a significant amount of trapped charges. Fig. 3.2b shows the data and theory on a double logarithmic scale, where we have subtracted the electrostatic background due to the AC calibration potential using the simultaneously obtained calibration data. At small separations $d < 60$ nm, both data sets curve upwards, which might be a sign of surface roughness effects. At separations $d > 120$ nm, the experimental data for the Au-Au Casimir interaction start to deviate significantly from the theory because of an artefact caused by reflections from the optical lever light by the sample. This reflected light reaches the photodetector and causes a background signal that is not related to any force. This artefact is common to all optical lever based AFM techniques, and the related signal is typically assumed to be linear in the piezo extension and subtracted from the data accordingly [35]. Because the reflectivities of our two samples are so different, we prefer to refrain from such a procedure, and present the data as is. In Figs. 3.2c and d we show histograms of all the obtained measurements for the derivative of the Casimir force for two specific separations ($d = 120$ nm and $d = 80$ nm). The histograms at $d = 80$ nm can be described by Gaussians with a standard deviation of roughly 5%, which means that our method provides a precision in the mean measured Casimir force derivative of 0.2%. It is evident from the histograms that the spatial derivative of the Casimir force between a Au and an ITO surface is roughly $\simeq 40\% - 50\%$ smaller than between two Au surfaces. In our geometry (i.e., for separations much smaller than the radius of the sphere), the spatial derivative of the force is proportional to the pressure between two parallel plates [41]. We can thus conclude that the Casimir pressure that one would measure between a Au plate kept parallel to an ITO plate would be roughly $\simeq 40\% - 50\%$ smaller than in the case of two Au plates.

Even though the agreement between the theoretical prediction and the measurement of the Casimir force in both situations is good, one might still argue that the observed decrease could be mimicked by drifts in d_0 . For both measurements series, we gathered 580 data sets continuously, which allows us to directly assess the run-to-run drift of d_0 . Due to the temperature stabilization of our setup, the mechanical drift is very small at $\simeq 0.1$ nm and $\simeq 0.2$ nm per run for the Au-Au and the Au-ITO experiments, respectively. We conclude that the decrease of the Casimir force cannot be ascribed to drifts in d_0 . We have also verified that the electrostatic force used to calibrate the instrument and extract d_0 follows what expected from elementary electrostatic arguments, as suggested in [38] and discussed in [19]. Concerning the compensation voltage, we observed that V_0 varies approximately 1 mV and 3 mV over the complete measurement range in the Au-Au and Au-ITO cases, respec-

tively [¶]. These slight variations of V_0 do not compromise the measurement of the Casimir force at the current level of sensitivity.

Finally, the different surface roughnesses of the sphere and the plates also influence the strength of the Casimir effect. Since both experiments are conducted with the same sphere, the difference in the observed Casimir force can never be due to the surface roughness of the sphere. Second, we recall that the surface roughness of the ITO sample is larger than that of the Au substrate. Since surface roughness enhances the Casimir force [67] we note that, if it played a role in the probed separation range, it would lead to a stronger interaction between Au and ITO than between two Au surfaces, contrary to the measurements presented in Fig. 3.2.

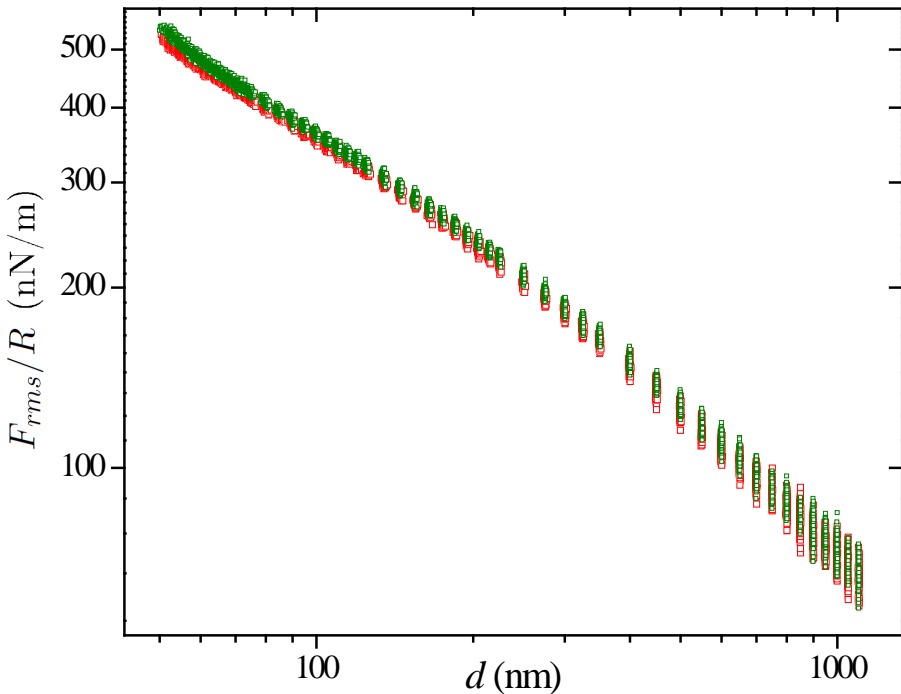


Figure 3.3: Hydrodynamic force acting on the sphere as a function of the absolute separation d for Au-Au (green squares) and Au-ITO (red squares), for the data sets shown in Figs. 3.2a and b.

To make our claim even more robust, we can now compare the hydrodynamic force observed during the two experiments. Because the geometrical configuration of the experiment is equal in both cases, we expect to measure the same hydrodynamic force. The results are shown in Fig. 3.3. It is clear that the hydrodynamic force is very similar in both cases, although there exists a slight discrepancy between the two curves ($\simeq 2\%$). Since both curves

[¶]The value of V_0 at $d = 100$ nm during the entire experiment drifts from -106 mV to -103 mV for Au and from 72 mV to 50 mV for ITO.

are parallel on a double logarithmic scale, we conclude that this discrepancy cannot be ascribed to a difference in the calibration of d_0 . Therefore, we rule out that the large difference in the Casimir force reported in Fig. 3.2 be due to an error in the determination of d_0 .

In conclusion, we have demonstrated that an ITO coating of one of the two surfaces is sufficient to readily create situations where the Casimir force is still the dominant interaction mechanism regardless the presence of air in the surroundings. Since ITO is transparent over a wide range of frequencies, the Casimir attraction is up to a factor of 2 smaller when compared to the case of the Au-Au interaction, leaving ample room for Casimir force engineering even at ambient conditions, where MEMS and NEMS typically operate.

This work was supported by the Netherlands Organisation for Scientific Research (NWO), under the Innovational Research Incentives Scheme VIDI-680-47-209. The authors thank A. Baldi, F. Mul, U. Mohideen, J. H. Rec tor, B. Dam, and R. Griessen for useful discussions, and the ESF Research Network CASIMIR for providing visit grants. S. M. acknowledges financial support from the Kavli Institute for Theoretical Physics (NSF PHY05-51164). D.I. acknowledges financial support from the European Research Council under the European Community's Seventh Framework Programme (FP7/2007-2013)/ERC grant agreement 201739.

RELAXING THE VACUUM

There are few topics in physics more prone to misrepresentation than the Casimir force. In popular discourse, the term is commonly preceded by 'ghostly', as though there is something barely credible about the manifestation of an attractive interaction between two surfaces separated by a vacuum. Interpretations in terms of virtual particles or suppressed quantum fluctuations of the electromagnetic field only encourage that view. But regarded as the familiar dispersion force resulting from induced dipoles, 'slowed down' by the finite speed of photons, the Casimir force becomes altogether more prosaic.

All the same, proposals to alter its influence — to engineer it — have about them something of the marvellous, as though the inescapable exigencies of nature are somehow being cheated. This possibility, however, was already implicit in Evgeny Lifshitz's recasting of the Casimir force in 1956, when he worked out the theory for real materials with finite dielectric permittivity (that's to say, finite conductivity). It's easy to see from Lifshitz's theory that, for certain choices of plate materials and media separating them, the Casimir force can actually be made repulsive. All the same, it wasn't until earlier this year that the right combination of materials — silica, gold and an

organic liquid — was found¹. (It's often overlooked that a classical analogue of this repulsive force, due to density fluctuations of a fluid at its critical point between two surfaces, was seen some time ago in superfluid helium².)

This raises the prospect of 'quantum levitation' and of ultralow friction and contactless bearings for micro- and nanoelectromechanical systems (MEMS and NEMS, respectively). But the reality is trickier. The choice of materials, for example, is commonly dictated by other engineering considerations. Transparent dielectric surfaces such as silica will in themselves reduce the Casimir attraction relative to reflective metals, even if they don't alter its sign. But they also have a tendency to accumulate surface charges in air, which, on non-conductive media, cannot be dissipated and create a strong electrostatic attraction. A thin film of noble metal such as gold will allay that issue, but at the expense of constraining the dielectric function and leaving little scope for tuning the Casimir force.

Davide Iannuzzi and colleagues at the University of Amsterdam have now shown that it is possible to combine the best of both worlds³. Conductive transparent metal oxides such as indium tin oxide (ITO), indispensable for semiconductor display technology, offer amenable dielectric properties



PHILIP BALL

while dispersing surface charges in air. The researchers have used a customized atomic-force microscope to measure the force between a gold-coated polystyrene microbead and a flat surface coated with gold or ITO. In both cases, the Casimir force clearly dominates over any residual Coulombic force in ambient conditions for separations down to about 60 nm. But for ITO the attractive force is about a factor of two smaller. This, they say, should leave plenty of scope for tailoring the interaction in MEMS/NEMS applications. It's an intriguing example of how the right choice of materials can alter the basic physics. □

References

1. Munday, J. N., Capasso, F. & Parsegian, V. A. *Nature* **457**, 170–173 (2009).
2. Garcia, R. & Chan, M. H. W. *Phys. Rev. Lett.* **88**, 086101 (2002).
3. de Man, S., Heeck, K., Wijngaarden, R. J. & Iannuzzi, D. *Phys. Rev. Lett.* **103**, 040402 (2009).

Figure 3.4: P. Ball, *News and Views*, *Nature Materials* **8**, 705 (2009)

3.3 Halving the Casimir force with conductive oxides: experimental details

Abstract – This work is an extended version of a paper published last year in Physical Review Letters [S. de Man *et al.*, Phys. Rev. Lett. **103**, 040402 (2009)], where we presented measurements of the Casimir force between a gold coated sphere and a plate coated with either gold or an indium-tin-oxide (ITO) layer. The experiment, which was performed in air, showed that ITO is sufficiently conducting to prevent charge accumulation, but still transparent enough to halve the Casimir attraction when compared to gold. Here, we report all the experimental details that, due to the limited space available, were omitted in the previous article. We discuss the performance of our setup in terms of stability of the calibration procedure and reproducibility of the Casimir force measurement. We also introduce and demonstrate a new technique to obtain the spring constant of our force sensor. Furthermore, we present a thorough description of the experimental method, a comprehensive explanation of data elaboration and error analysis, and a complete characterization of the dielectric function and of the surface roughness of the samples used in the actual experiment.

[¶]This paper has been published: S. de Man, K. Heeck, and D. Iannuzzi, *Phys. Rev. A* **82**, 062512 (2010)

3.3.1 Introduction

It is well known that the Casimir effect [18] strongly depends on the dielectric function of the interacting surfaces [23, 41]. Transparent dielectrics, for example, attract less than highly reflective metals. Dielectric materials, however, tend to accumulate isolated charges. Those charges give rise to an electrostatic force that easily overcomes the Casimir interaction.

In a recent paper [20], we have presented measurements of the Casimir force between a gold coated sphere and a plate coated with either gold or an Indium-Tin-Oxide (ITO, $\text{In}_2\text{O}_3:\text{Sn}$) layer. The experiment, which was performed in air, showed that ITO is sufficiently conducting to prevent charge accumulation, but still transparent enough to halve the Casimir attraction when compared to gold.

The experiment was carried out by means of a quite complicated novel technique that, due to the limited space available, was not thoroughly explained in our previous work. We believe it is important to extend that work and provide the community with all the details of the experimental technique and data analysis, which is the purpose of this paper.

This paper is organized as follows. First, we describe the experimental setup and discuss general issues one has to tackle to perform Casimir force measurements. Then we discuss the experimental technique we developed to simultaneously calibrate the setup and measure the Casimir force gradient, and derive in detail the specific forms of all our calibration and measurement signals. Second, we illustrate a new method to determine the spring constant of our force sensor. Third, we present experimental results on the general performance of our setup, namely the stability of the calibration procedure, the reproducibility of the force gradient measurements, and the spring constant determination. Fourth, we present the Casimir force measurements for the gold-gold and gold-ITO interactions, and show measurements of the dielectric functions and surface topographies of our surfaces. Finally we compare the hydrodynamic forces for the two sets of experiments.

3.3.2 Experimental setup

Description

Our experimental setup is designed to precisely measure surface forces between a $100\ \mu\text{m}$ radius sphere and planar samples at ambient pressure. The sphere is attached to a micromachined cantilever (spring constant roughly $1\ \text{N/m}$) whose deflection in response to external forces can be measured with pm sensitivity by a commercial Atomic Force Microscope (AFM) detection head (Veeco Multimode); the detection system is formed by a laser beam that reflects from the free end of the cantilever and hits a position sensitive photodetector (see Fig. 3.5). The sphere-cantilever assembly is coated with a Ti adhesion layer

and a 100 nm Au film. The planar sample is mounted on a two-stage mechanical translator formed by a stick-slip piezoelectric motor (Attocube) and a feedback controlled piezoelectric transducer (Physik Instrumente) to vary the separation between the sphere and plate surfaces. The stick-slip motor is used for coarse approach (travel range 6mm), while the feedback controlled transducer executes the fine distance scanning (range 12 μm , closed loop resolution 50 pm). Both the detection head and the two-stage mechanical translator are anchored to a 10 cm³ Al block that is actively temperature stabilized at 300 K to reduce mechanical drift from differential thermal expansion of the components. The Al block is screwed onto an active anti-vibration table (Halcyonics), which is placed inside an anechoic chamber. This chamber lies onto a heavy marble optical table that is located in a temperature controlled laboratory.

Three crucial issues

In a Casimir force measurement, there are three crucial issues that have to be dealt with.

First, even if one would electrically connect both interacting surfaces, there exists an electrostatic potential difference V_0 due to the different work functions of the surfaces. Since work functions of surfaces depend on quite a number of parameters, like crystal growth orientation and adsorbates, typically there even exists a potential difference between surfaces made out of the same material. This electrostatic potential difference gives rise to a force that is generally stronger than the Casimir force. To avoid this problem, most Casimir force setups rely on a counterbias circuit that is used to apply $-V_0$ to the surfaces in order to have no residual electrostatic force.

Second, even in setups where the distance between the sphere and the plate is varied with a feedback controlled piezoelectric transducer, one has only knowledge of the relative position changes and not of the absolute separation between the surfaces. It is thus mandatory to find the initial separation d_0 with a calibration procedure. Because the distance dependence of the electrostatic force between a sphere and a plate is known exactly, most modern setups use this force to extract d_0 .

Third, the instrument has to be calibrated with a known force. Again, one can use the electrostatic interaction to calibrate photodetector voltage versus force. We have developed a measurement scheme that solves all three issues at the same time.

Force modulation measurements

We present a measurement technique that makes use of simultaneous detection of both calibration signals (based on the electrostatic force) and the Casimir force. The motivation for this approach is the benefit of absolute certainty that the calibration parameters always correspond to the measured forces because

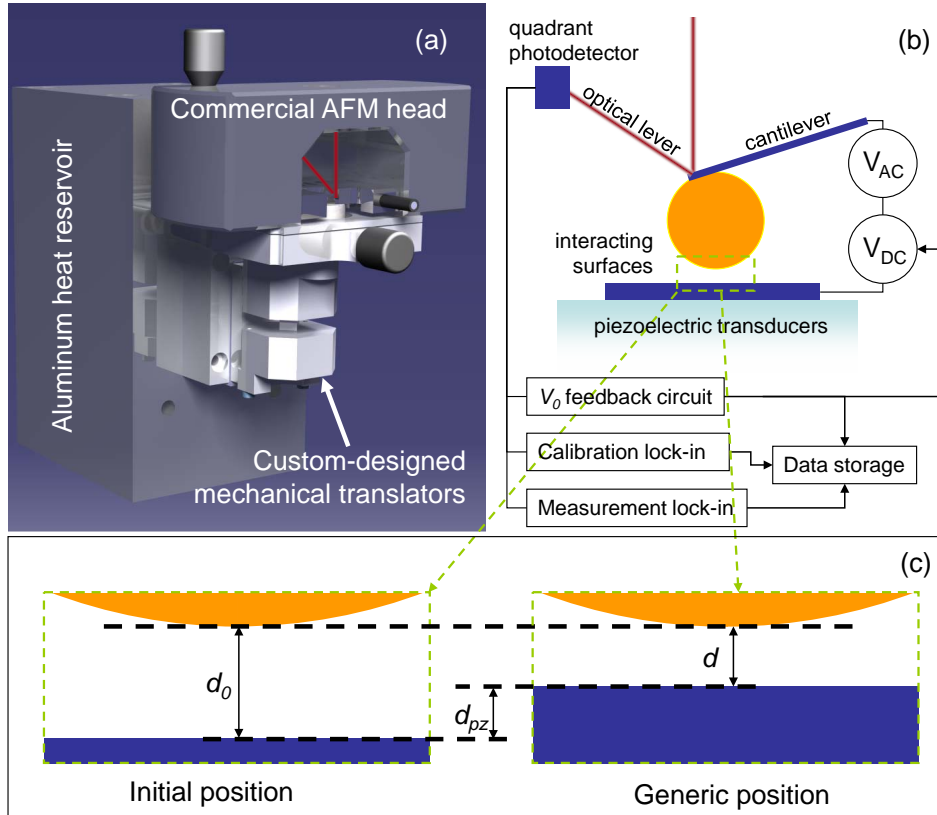


Figure 3.5: **a**, Drawing of the experimental setup used to perform precise measurements of the Casimir force between a $100 \mu\text{m}$ radius sphere and a plate. The aluminum block acts as a heat reservoir to keep the temperature of the setup constant. The instrument is based on a commercial AFM head that is, together with a custom-designed mechanical translator, mounted on the aluminum block. **b**, Schematic representation of the working principle of the experimental technique. The V_0 feedback circuit allows one to measure and compensate the residual voltage present between the sphere and the plate. The calibration lock-in amplifier is used to calibrate the instrument and to find the initial separation between the two surfaces d_0 . The measurement lock-in amplifier performs the measurements of the Casimir force gradient and the hydrodynamic force. **c**, Definition of the initial separation d_0 , the movement of the feedback controlled piezoelectric stage d_{pz} , and the non-modulated separation between the surfaces $d = d_0 - d_{pz}$ as used in the Taylor expansion that leads to Eqs. 3.2 to 3.7.

they are acquired simultaneously; it is thus impossible to have inconsistent calibration and force data due to time-related drifts or other events. In order to achieve this goal, we have separated the calibration and Casimir signals in frequency space: the signals are modulated at distinct frequencies that can be de-modulated individually with lock-in amplifiers.

Modulating an electrostatic interaction is extremely easy: one just has to apply a time-dependent potential difference to the sphere and the plate (V_{AC} in Fig. 3.5 b). We thus apply an oscillating voltage $V_{DC} + V_{AC} \cos(\omega_1 t)$ between the sphere and the plate, where V_{DC} is used to compensate for the contact potential difference V_0 [19]. Unfortunately, modulating the Casimir force is a lot more challenging as its strength depends only on geometry and dielectric properties of the surfaces. On the other hand, of course, the strong distance dependence of the Casimir force can be used to modulate its strength considerably. Therefore, we chose to add a small modulation of the form $\Delta d \cos(\omega_2 t)$ to the piezoelectric transducer displacement d_{pz} , as previously introduced in [62]. When the sphere and plate surfaces are separated by a distance d , we have the following three forces acting on the sphere: $F(V, d, \omega_2, \Delta d) = F_E(V, d) + F_C(d) + F_H(d, \omega_2, \Delta d)$ where $F_E(V, d)$ is the electrostatic force for externally applied potential difference V , $F_C(d)$ is the Casimir force, and $F_H(d, \omega_2, \Delta d)$ is the hydrodynamic force due to the moving air caused by the oscillatory motion of the plate. These forces induce a bending of the cantilever F/k according to Hooke's law, where k is the spring constant of the cantilever. The output of the optical lever read-out S is then changed by $\Delta S = \gamma F/k$, where the sensitivity of the read-out is characterized by the calibration factor γ . We will now develop the full form of this signal ΔS .

Following elementary electrostatic arguments, one can show that the electrostatic force between a plane and a sphere of radius R is given by

$$F_E(V, d) = -\frac{\varepsilon_0 \pi R (V + V_0)^2}{d}, \quad (3.1)$$

where ε_0 is the permittivity of vacuum, V is the externally applied voltage, V_0 is the contact potential difference between the two surfaces, and $d \ll R$ (i. e. within the *proximity force approximation* (PFA) [41]). To evaluate the total signal ΔS , we substitute $V = V_{DC} + V_{AC} \cos(\omega_1 t)$ and incorporate the distance modulation $\Delta d \cos(\omega_2 t)$. We then approximate the photodetector signal with a first order Taylor expansion for small excursion $\Delta d \cos(\omega_2 t)$ around $d = d_0 - d_{pz}$ (see Fig. 3.5 c):

$$\Delta S(t) \simeq S_0 + S_{\omega_1} \cos(\omega_1 t) + S_{2\omega_1} \cos(2\omega_1 t) + S_{\omega_2}^I \cos(\omega_2 t) + S_{\omega_2}^Q \sin(\omega_2 t) + S_{\text{rem}}(t), \quad (3.2)$$

where

$$S_0 = -\frac{\gamma\epsilon_0\pi R \left[(V_0 + V_{DC})^2 + V_{AC}^2/2 \right]}{k(d_0 - d_{pz})} + \frac{\gamma}{k} F_C(d_0 - d_{pz}), \quad (3.3)$$

$$S_{\omega_1} = -\frac{2\gamma\epsilon_0\pi R (V_0 + V_{DC}) V_{AC}}{k(d_0 - d_{pz})}, \quad (3.4)$$

$$S_{2\omega_1} = -\frac{\gamma\epsilon_0\pi R}{k(d_0 - d_{pz})} \frac{V_{AC}^2}{2}, \quad (3.5)$$

$$S_{\omega_2}^I = -\frac{\gamma\epsilon_0\pi R \left[(V_0 + V_{DC})^2 + V_{AC}^2/2 \right] \Delta d}{k(d_0 - d_{pz})^2} - \frac{\gamma}{k} \left. \frac{\partial F_C}{\partial d} \right|_{d_0 - d_{pz}} \Delta d, \quad (3.6)$$

$$S_{\omega_2}^Q = \frac{\gamma}{k} F_H(d_0 - d_{pz}, \omega_2, \Delta d), \quad (3.7)$$

$F_C(d_0 - d_{pz})$ is the Casimir force at separation $d_0 - d_{pz}$, $S_{\text{rem}}(t)$ contains the cross terms at frequencies like $\omega_1 \pm \omega_2$ and $2\omega_1 \pm \omega_2$ and the gradient of the hydrodynamic force at $2\omega_2$, and we have neglected the effect of the cantilever deflection on the distance between the surfaces. Since the remaining terms in S_{rem} are located at different frequencies than our measurement signals, they do not interfere with the lock-in measurements of S_{ω_1} , $S_{2\omega_1}$, $S_{\omega_2}^I$ and $S_{\omega_2}^Q$. S_{rem} will thus be neglected in the rest of the paper.

Eq. 3.2 is only valid if the force sensor can follow the modulations of the force without picking up phase delays. It is thus convenient to operate in the quasi-static regime, which also ensures that the amplitude response of our cantilever at the various measurement frequencies does not vary. For these reasons, we set $\omega_1/2\pi = 72.2$ Hz and $\omega_2/2\pi = 119$ Hz, which are both much lower than the resonance frequency of the force sensor (1.9 kHz, quality factor $\simeq 75$ in air). Furthermore, we have not included the elastic component of the hydrodynamic interaction in $S_{\omega_2}^I$. According to [68], the compression effect is small as long as $\sigma_{\text{sphere}} = \frac{4\eta\omega_2 R}{pd} < 1$, where η is the viscosity of air and p is the air pressure. In our experiment, $\sigma_{\text{sphere}} \leq 10^{-3}$, so the elastic component can be neglected and we only have to consider the dissipative part of $F_H(d, \omega_2)$. Since a dissipative effect depends on velocity $v = \partial d / \partial t = \omega_2 \Delta d \sin(\omega_2 t)$, it will manifest itself as a cantilever oscillation at ω_2 with a corresponding detector signal $S_{\omega_2}^Q$ that is 90 degrees rotated with respect to $S_{\omega_2}^I$.

Electrostatic calibration

The first task of the electrostatic calibration procedure is to compensate for the presence of the contact potential difference V_0 between the two interacting surfaces. Since S_{ω_1} is proportional to $V_0 + V_{DC}$ (see Eq. 3.4), we can create a negative feedback loop in which a lock-in amplifier at ω_1 generates V_{DC} in such

a way that S_{ω_1} vanishes, i.e. $V_{DC} = -V_0$ [19, 39]. The stability of this feedback loop is guaranteed by a single large time constant. In the current experiment, the systematic error in the compensation voltage is negligible ($|V_0 + V_{DC}| < 50 \mu\text{V}$), and the statistical error is $\simeq 1 \text{ mV}$. This feedback scheme is similar to Kelvin probe force microscopy [40], and allows one to measure V_0 at all sphere-plane separations. Even more, the automatic compensation of V_0 leads to the zeroing of the $(V_0 + V_{DC})$ terms in Eqs. 3.3 and 3.6, greatly simplifying the measurement scheme.

The periodic component of ΔS at $2\omega_1$, $S_{2\omega_1}$, measured with a second lock-in amplifier (the calibration lock-in in Fig. 3.5 b), is used to calibrate the force sensitivity and to find the initial separation between the surfaces d_0 . We define

$$\alpha = \frac{\gamma \varepsilon_0 \pi R}{k (d_0 - d_{pz})}. \quad (3.8)$$

According to Eq. 3.5, α can be experimentally obtained from $\alpha = 2 |S_{2\omega_1}| / V_{AC}^2$. In this way, we have essentially performed an AC measurement of the curvature of the electrostatic parabola, instead of using multiple DC measurements with different applied voltages [32]. We measure α as a function of d_{pz} by varying the extension of the capacitive feedback controlled piezoelectric transducer (see Fig. 3.5c) in discrete steps. We then fit Eq. 3.8 to these α data. This procedure allows us to calibrate the separation at the start of the measurement d_0 and the force sensitivity $\kappa = \gamma \varepsilon_0 \pi R / k$ for each measurement run. We then use the estimate of d_0 to adjust the initial value of d_{pz} of the next measurement run in order to have all runs start at the same separation. To avoid large electrostatic forces at small separations, we reduce V_{AC} as the surfaces approach such that $S_{2\omega_1}$ stays nearly constant at a value that corresponds to a root-mean-square electrostatic force of $\simeq 50 \text{ pN}$ [19].

Casimir force measurement

We use a third lock-in amplifier (the measurement lock-in in Fig. 3.5 b), locked at ω_2 , to measure the Casimir force. The phase of this lock-in amplifier is aligned to the actual motion of the plate by examining the signal from a dedicated fiber optic interferometer (not shown in Fig. 3.5). The same interferometer is used to calibrate the amplitude Δd of the separation modulation. We see from Eq. 3.6 that the in-phase component $S_{\omega_2}^I$ contains both an electrostatic contribution and the gradient of the Casimir force F_C at the current separation. Since $V_0 + V_{DC} = 0$ by the V_0 feedback circuit, Eq. 3.6 simplifies to

$$S_{\omega_2}^I = -\frac{\gamma \varepsilon_0 \pi R}{k (d_0 - d_{pz})^2} \frac{V_{AC}^2}{2} \Delta d - \frac{\gamma}{k} \left. \frac{\partial F_C}{\partial d} \right|_{d_0 - d_{pz}} \Delta d. \quad (3.9)$$

Combining Eqs. 3.5 and 3.9, one obtains

$$S_{\omega_2}^I = \frac{S_{2\omega_1}}{d_0 - d_{pz}} \Delta d - \frac{\gamma}{k} \frac{\partial F_C}{\partial d} \Big|_{d_0 - d_{pz}} \Delta d. \quad (3.10)$$

Since the absolute separations $d_0 - d_{pz}$ and $S_{2\omega_1}$ are known from the simultaneous electrostatic calibration (and Δd is calibrated too), one can calculate the value of the first term of Eq. 3.10. Using the force sensitivity $\kappa = \gamma \varepsilon_0 \pi R / k$ obtained from the calibration, we can finally get the Casimir force gradient:

$$\frac{1}{R} \frac{\partial F_C}{\partial d} = \frac{\varepsilon_0 \pi}{\kappa} \left(\frac{S_{2\omega_1}}{d_0 - d_{pz}} - \frac{S_{\omega_2}^I}{\Delta d} \right). \quad (3.11)$$

It is interesting to note that we obtain the Casimir force gradient divided by the sphere radius R , because we have calibrated the instrument with the electrostatic force which scales linearly in R (see Eq. 3.1). However, within the PFA, the gradient of the force between a sphere and a plate relates directly to the pressure between two parallel plates P_{pp} as long as $d \ll R$:

$$\frac{1}{R} \frac{\partial F_C}{\partial d} = 2\pi P_{pp}(d), \quad (3.12)$$

where $P_{pp}(d)$ can be calculated with the Lifshitz theory [23] and depends only on the dielectric properties of the interacting surfaces. Therefore, we can directly compare our $1/R \partial F_C / \partial d$ data to theory, without any need to know the precise radius of the sphere.

Furthermore, by using a quadrature lock-in amplifier at ω_2 , we can obtain $S_{\omega_2}^Q$ together with $S_{\omega_2}^I$. We can thus measure the hydrodynamic interaction between the sphere and the plate simultaneously with, but independently from, the Casimir force gradient.

Determination of deflection sensitivity and cantilever spring constant

So far, we have neglected the bending of the cantilever in the assessment of the distance between the sphere and plate surfaces. This is valid as long as the forces are relatively weak and the spring constant of the cantilever is relatively high. Of course, the nominal spring constant of the cantilever is supplied by the manufacturer, but the addition of a glued sphere and metal coating influence the stiffness. Therefore, we have developed a technique to measure the spring constant with the electrostatic force. Furthermore, this method also allows us to extract the deflection sensitivity γ of the optical lever readout; we can then convert photodetector signal ΔS into cantilever deflection F/k . This technique might be useful for AFM force measurements in general.

To obtain the cantilever spring constant and the deflection sensitivity, we apply a relatively large V_{AC} between the sphere and the plate. Exactly like described above in the electrostatic calibration section, we keep the electrostatic

force at $2\omega_1$ constant, but now at roughly 2 nN RMS instead of 50 pN RMS, by reducing V_{AC} while increasing the piezoelectric transducer extension d_{pz} in discrete steps. This strong force will reduce the sphere plate distance, and we therefore have to solve the following implicit equation for the electrostatic force

$$F_E = -\frac{\varepsilon_0\pi RV^2}{d_0 - d_{pz} + F_E/k} \quad (3.13)$$

where, since we have already dealt with the contact potential difference V_0 with the feedback circuit, V just refers to the AC component of the applied voltage. For the sake of simplicity, we have omitted the piezo modulation at ω_2 from this derivation, as it does not affect the results. Eq. 3.13 has two solutions for F_E , and the physically correct one reads

$$F_E = -\frac{1}{2} \left[k(d_0 - d_{pz}) - \sqrt{k^2(d_0 - d_{pz})^2 - 4k\varepsilon_0\pi RV^2} \right]. \quad (3.14)$$

If we Taylor expand this expression for small cantilever deflection (which means small force and small applied voltage V), and use $\Delta S = \gamma F/k$, we obtain

$$\Delta S = -\frac{\gamma\epsilon_0\pi RV^2}{k(d_0 - d_{pz})} - \frac{\gamma\epsilon_0^2\pi^2 R^2 V^4}{k^2(d_0 - d_{pz})^3} + O(V^6). \quad (3.15)$$

Substituting $V = V_{AC} \cos(\omega_1 t)$ and neglecting the higher order terms yields a detector signal

$$\Delta S(t) \simeq S_0 + S_{2\omega_1} \cos(2\omega_1 t) + S_{4\omega_1} \cos(4\omega_1 t), \quad (3.16)$$

where S_0 is the DC component and the amplitudes of the two AC components are given by

$$S_{2\omega_1} = -\frac{\gamma\epsilon_0\pi RV_{AC}^2}{2k(d_0 - d_{pz})} - \frac{\gamma\epsilon_0^2\pi^2 R^2 V_{AC}^4}{2k^2(d_0 - d_{pz})^3} \quad (3.17)$$

and

$$S_{4\omega_1} = -\frac{\gamma\epsilon_0^2\pi^2 R^2 V_{AC}^4}{8k^2(d_0 - d_{pz})^3}. \quad (3.18)$$

$S_{2\omega_1}$ is already measured by our electrostatic calibration lock-in amplifier, and we simply add another lock-in amplifier locked at $4\omega_1$ to detect $S_{4\omega_1}$.

The second term in Eq. 3.17 is much smaller than the first term and can be neglected. We then find that

$$V_{AC} \sqrt{\frac{S_{2\omega_1}}{S_{4\omega_1}}} = 2\sqrt{\frac{k}{\epsilon_0\pi R}}(d_0 - d_{pz}), \quad (3.19)$$

which means that we can obtain k/R by fitting Eq. 3.19 to data of $V_{AC} \sqrt{S_{2\omega_1}/S_{4\omega_1}}$ as a function of relative piezo displacement d_{pz} . Apart from the resulting

knowledge on the cantilever spring constant (the sphere radius is roughly known), we also obtain the deflection sensitivity γ by combining the value of k/R with the one of $\kappa = \gamma \varepsilon_0 \pi R/k$ determined by the analysis of the simultaneously acquired α data (as described in the electrostatic calibration procedure).

3.3.3 Results and Discussion

We have divided our experimental results into two parts. In the first part, we describe the precision and stability of the electrostatic calibration procedure and comment on the reproducibility of the Casimir force gradient detection in a set of 580 measurement runs between two gold coated surfaces. Also, we present a single dataset obtained with a large electrostatic force between the sphere and the plate that allows us to check the validity of Eq. 3.6 (and Eq. 3.11 as well), and to obtain the spring constant of our cantilever and the deflection sensitivity of the optical lever readout. In the second half, we combine the Casimir force measurements between the two gold surfaces with measurements between a gold surface and a surface coated with ITO ($\text{In}_2\text{O}_3:\text{Sn}$), as presented in [20], adding details that, for the sake of brevity, were previously omitted. Furthermore, we obtain the hydrodynamic forces for both measurement sets and compare the results.

General performance

We will now analyze the 580 measurement runs between two gold surfaces obtained during nearly 72 hours of continuous data acquisition. In this experiment, the separation between the surfaces is varied in discrete steps with the feedback controlled piezoelectric transducer, and a typical measurement run consists of $\simeq 50$ d_{pz} set points in the measurement range $50 < d < 1100$ nm. The lock-in measurements are obtained with 24 dB roll-off low-pass filter settings with 1 s RC time. The waiting time for every value of d_{pz} is 8 s, and a complete run takes roughly 7 minutes. The $S_{2\omega_1}$ set point corresponds to a cantilever movement of approximately 50 pm RMS. The distance modulation is set to $\Delta d = 3.85 \pm 0.08$ nm, and the in-phase and out-of-phase cantilever responses at ω_2 are < 80 pm RMS during the entire experiment. All force measurements are performed in air at atmospheric pressure, temperature 300 K, and 29% relative humidity.

Concerning the electrostatic calibration, we have to fit our α data with Eq. 3.8 to obtain the initial separation d_0 and the force sensitivity κ . Due to the fact that we hold $S_{2\omega_1}$ constant by reducing V_{AC} , the relative statistical error in α is constant (see reference [19]) and was measured to be $\simeq 0.7\%$. We have verified that α follows Eq. 3.8, as suggested in [38] and discussed in [19]. In Fig. 3.6 and Fig. 3.7, we present the fitted values for d_0 and κ and analyze their stability in time. Fig. 3.6 a shows all the values of d_0 for the 580 runs

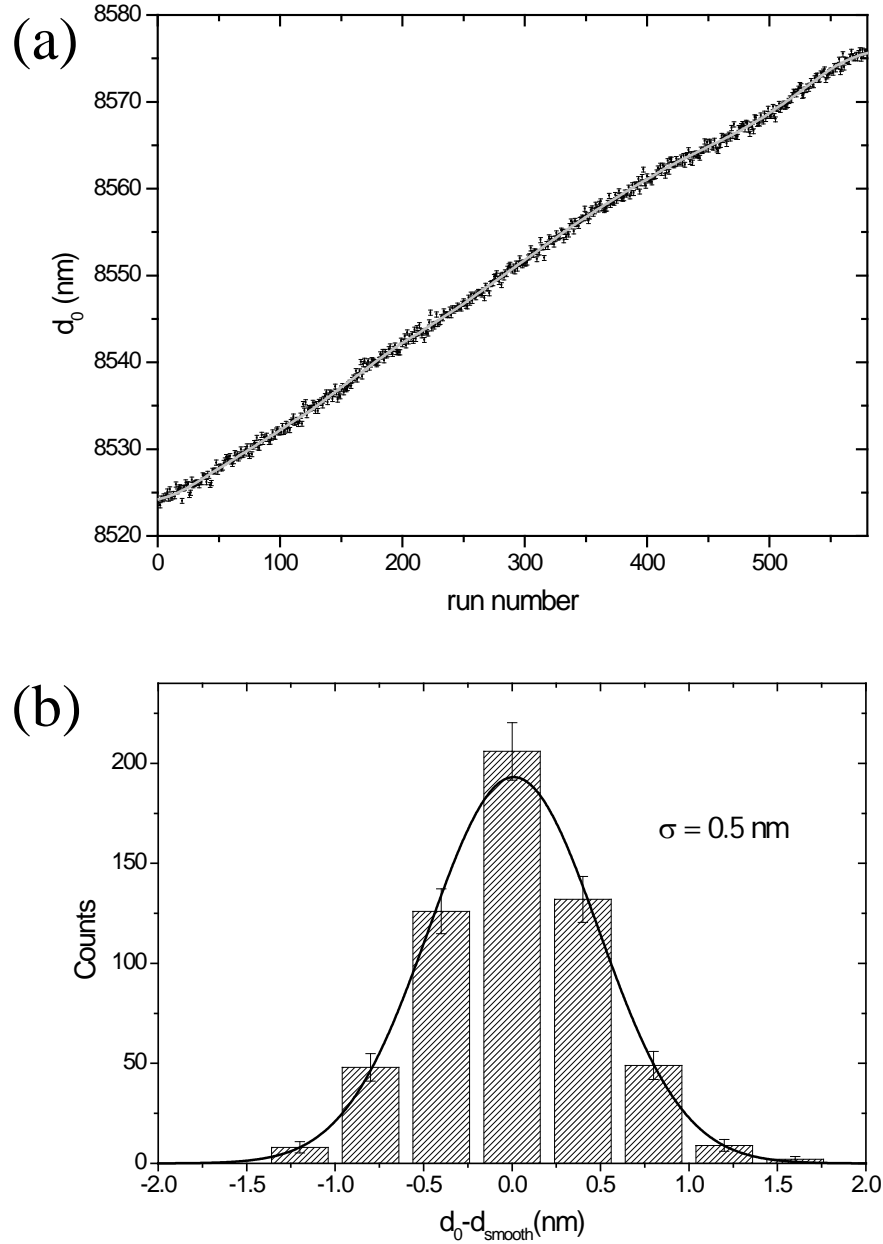


Figure 3.6: Mechanical stability of the experimental setup. **a**, Mechanical drift in the initial separation d_0 as a function of run number for all 580 Au-Au measurement runs. The error bars are determined by propagation of the error on α into the estimate of d_0 by the fit with Eq. 3.8. The grey line represents a trend line that accounts for the slow thermal drift of the setup. **b**, Histogram of the differences between the measured d_0 values and the grey line of a. The line represents the best Gaussian fit, resulting in a 0.5 nm standard deviation.

with error bars as propagated from the error on α . The grey line represents the smooth thermal expansion of the setup, and is estimated by smoothing the data with a 100 point moving window second order Savitsky-Golay filter. The total mechanical drift of our setup is 52 nm in 72 hours, which is less than 1 nm per hour and less than 0.1 nm per measurement run. Clearly, we can neglect the mechanical drift in our assessment of separation between the surfaces in a single run. In Fig. 3.6 b, we plot a histogram of the difference between the d_0 data and the smoothed grey line of Fig. 3.6 a. These differences are clearly normally distributed with a standard deviation of 0.5 nm. Therefore, in these experimental runs, we could determine the separation between the sphere and plate surfaces with 0.5 nm precision. This estimate of the precision in the measurement of d_0 is insensitive to the precise form and size of the smoothing window.

Fig. 3.7 a shows all the values of the force sensitivity κ that we obtained from the fit to our electrostatic calibration data. The error bars are calculated by propagating the errors on α . The grey line is a smoothed trend line that represents slow variations in κ over time, obtained by smoothing the data with a 200 point moving window second order Savitsky-Golay filter. There is clearly no long-term drift in the force sensitivity, which shows that our setup is very stable. In Fig. 3.7 b, we plot a histogram of the relative deviations between our κ data and the smooth grey line of Fig. 3.7 a. These deviations are normally distributed with a standard deviation of 0.2%, and are insensitive to the specifics of the smoothing window. We have thus determined the force sensitivity of the setup for every single measurement run with a precision of 0.2%.

In Fig. 3.8 we present measurements of the total force gradient

$$\frac{1}{R} \frac{\partial F}{\partial d} = -\frac{\varepsilon_0 \pi}{\kappa} \frac{S_{\omega_2}^I}{\Delta d} \quad (3.20)$$

as a function of the non-modulated separation $d = d_0 - d_{pz}$ (see Fig. 3.5 c). This force gradient should, according to Eq. 3.11, obey

$$\frac{1}{R} \frac{\partial F}{\partial d} = \frac{1}{R} \frac{\partial F_C}{\partial d} + \frac{1}{R} \frac{\partial F_E}{\partial d} \quad (3.21)$$

with

$$\frac{1}{R} \frac{\partial F_E}{\partial d} = -\frac{\varepsilon_0 \pi}{\kappa} \frac{S_{2\omega_1}}{d_0 - d_{pz}}. \quad (3.22)$$

In Fig. 3.8 a, the data points represent the $-\varepsilon_0 \pi S_{\omega_2}^I / (\kappa \Delta d)$ data points and the solid line shows the electrostatic force gradient as obtained with Eq. 3.22 from the $S_{2\omega_1}$ values of the simultaneous electrostatic calibration procedure. For clarity, we have shown only 150 measurement runs out of the total 580. It is clear that in the distance range that our setup is sensitive for the Casimir force,

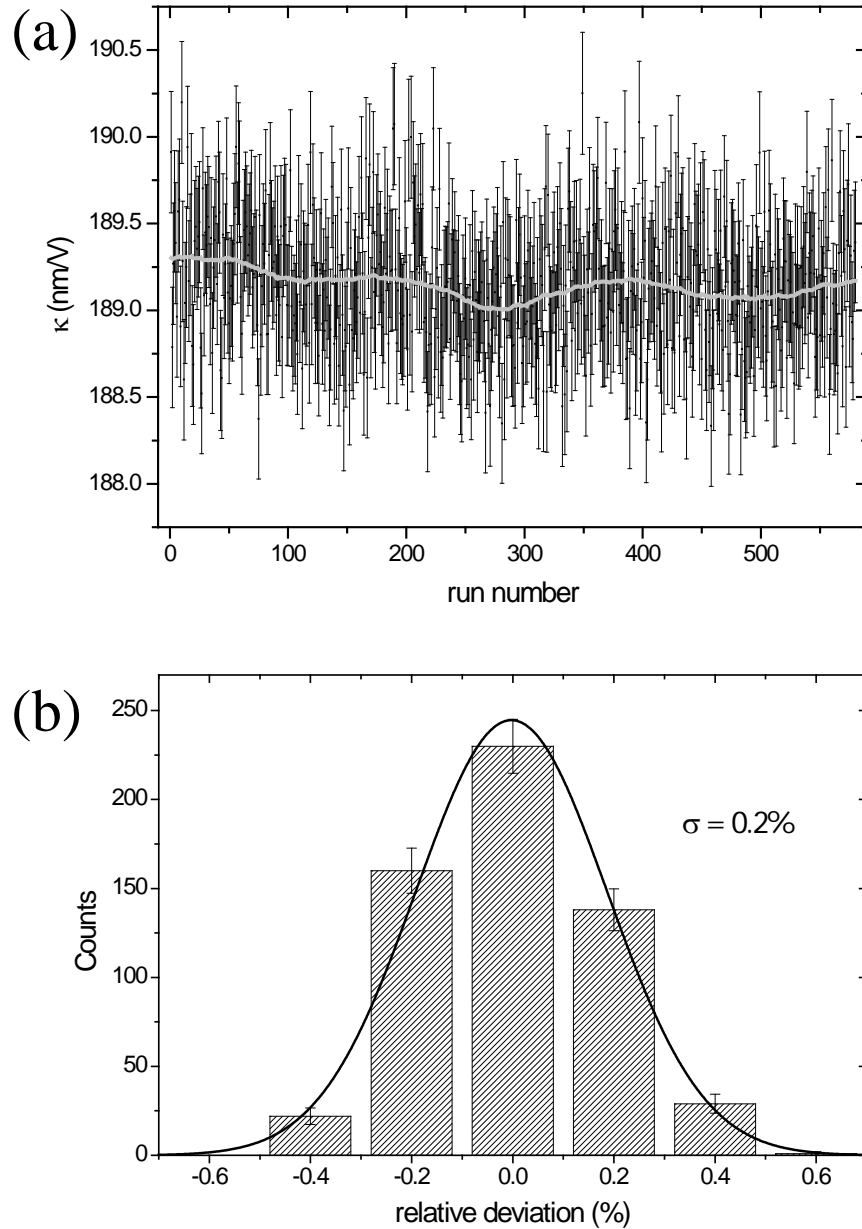


Figure 3.7: Stability of the electrostatic calibration. **a**, All 580 obtained values for the force calibration constant κ as a function of run number. The error bars are calculated by propagating the error on α . The grey line is a smooth trend line that accounts for slow variations. **b**, Histogram of the relative deviations of the κ data from the trend line in c. The Gaussian fit has a standard deviation of 0.2%.

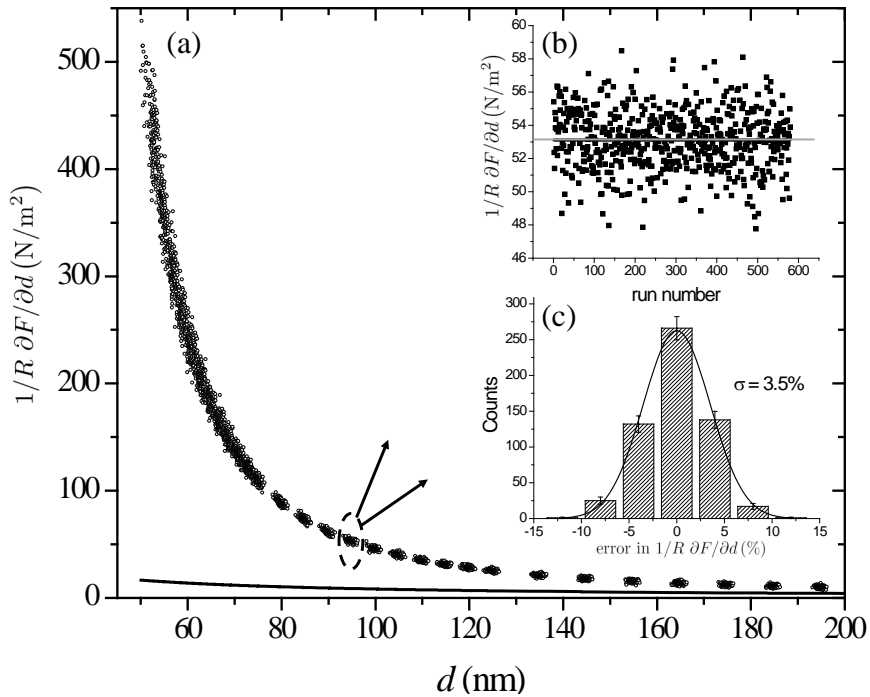


Figure 3.8: **a**, The data points represent measurements of the total force gradient as a function of separation between the sphere and plate surfaces for 150 measurement runs out of a total of 580 runs. The line shows the electrostatic force gradient associated to the simultaneous calibration procedure. **b**, Plot of all 580 force gradient measurements obtained for $d \simeq 95$ nm as a function of time. The grey line represents the average force gradient. **c**, Histogram of all the relative deviations between the single force gradient measurements around 95 nm and the average force gradient. The Gaussian fit has a standard deviation of 3.5%.

the electrostatic force gradient caused by the simultaneous electrostatic calibration is small compared to the Casimir force gradient. To assess the stability of our force gradient measurement, we have plotted all 580 $1/R \partial F / \partial d$ data points gathered around 95 nm from our 580 measurement runs in Fig. 3.8 b. Our data do not show any drift in time, which means that the setup is stable. The grey line represents the average of the data points. In Fig. 3.8 c, we plot a histogram of all the relative deviations of the data with respect to the average. These deviations are normally distributed with a standard deviation of 3.5%, which corresponds to a standard deviation in the measurement of the force gradient of 1.85 N/m^2 . This value represents an overestimate of the noise though, because the data are obtained at slightly different separations; the exact position of a data-point depends on the estimate of d_0 coming from the previous measurement run. Since the error in the determination of d_0 is 0.5 nm (see Fig. 3.6 b), the data are horizontally scattered with a standard deviation of 0.5 nm. For $d \simeq 95 \text{ nm}$, the local slope of the data in Fig. 3.8 a is approximately $1.3 \text{ Nm}^{-2}/\text{nm}$, which translates this scatter in d into a force gradient scatter of 0.65 N/m^2 . Therefore, the actual precision in a single force gradient data point around 95 nm is 1.75 N/m^2 , if we assume that both the force gradient noise and the scatter in separation are uncorrelated.

From the electrostatic calibration results, we could have also estimated the noise in the force gradient measurement. In fact, the noise in $S_{2\omega_1}$ is $30 \mu\text{V}$ RMS with a 1 s RC time. The force gradient signal at ω_2 is located at a comparable frequency, therefore the noise will be quite the same. If we substitute our measured values of κ and Δd into Eq. 3.20, we see that we would have expected the noise in $1/R \partial F / \partial d$ to be 1.62 N/m^2 . But we have not taken into account yet the 0.5 nm error in the separation that arises from the estimate of d_0 . For $d \simeq 95 \text{ nm}$, this results in an additional statistical error of 0.65 N/m^2 in the force gradient at this distance. The combined error, assuming the force gradient and distance errors are uncorrelated, is then 1.75 N/m^2 for $d \simeq 95 \text{ nm}$, which agrees perfectly with the data of Fig. 3.8.

Since our Casimir force gradient measurement consists of measuring the total force gradient and subtracting the electrostatic force gradient (see Eq. 3.11), it is interesting to investigate the accuracy in the assessment of $1/R \partial F_E / \partial d$. For that, we have gathered a new dataset with a relatively strong electrostatic interaction (high V_{AC}) between the sphere and the plate. When we combine the high V_{AC} total force gradients with measurements obtained with low V_{AC} , we can get

$$\frac{1}{R} \frac{\partial F}{\partial d} \bigg|_{V_{AC}>} - \frac{1}{R} \frac{\partial F}{\partial d} \bigg|_{V_{AC}<} = \frac{1}{R} \frac{\partial F_E}{\partial d} \bigg|_{V_{AC}>} - \frac{1}{R} \frac{\partial F_E}{\partial d} \bigg|_{V_{AC}<} \quad (3.23)$$

because the Casimir force gradient is equal in both cases and drops out. Even more, any other systematic effects present in the force gradient measurement that do not depend on V_{AC} , like, for example, laser light that reflects from the

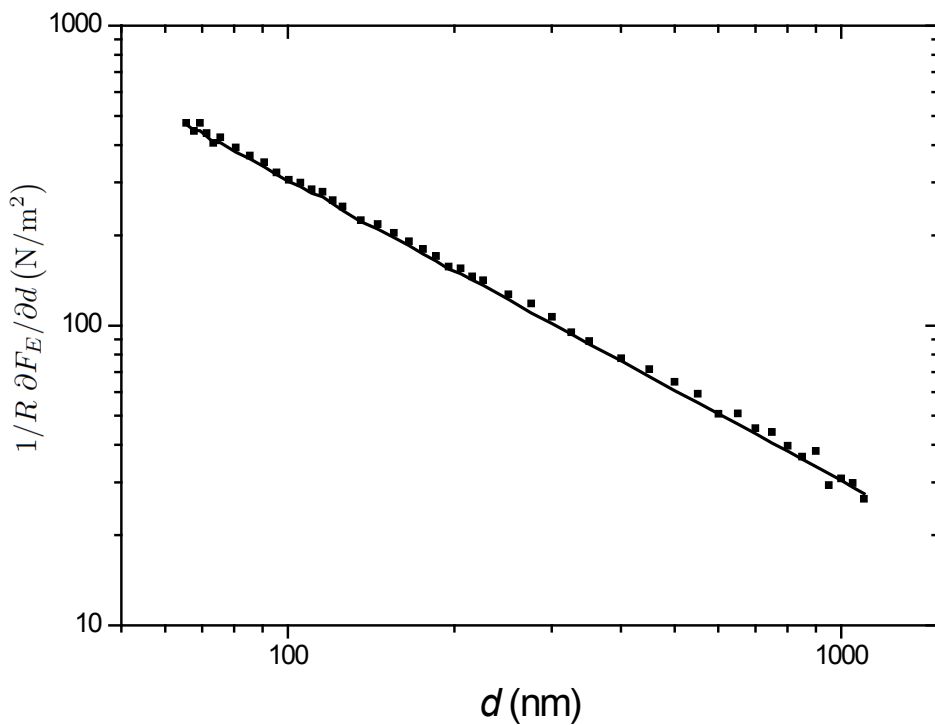


Figure 3.9: Plot of the electrostatic force gradient difference between a measurement run performed with a strong electrostatic interaction and a run performed with a weak electrostatic force. Data are plotted as a function of separation. The line corresponds to the electrostatic force gradient obtained from the calibration signal. See text for details.

planar sample and hits the photodetector, are also cancelled in this way. The right-hand-side of Eq. 3.23 can be calculated with Eq. 3.22, and we can thus assess the validity of the latter and, consequently, of Eq. 3.11. In Fig. 3.9, we have plotted the difference in total force gradients (obtained with Eq. 3.20) as a function of distance. The solid line represents the difference in calculated electrostatic force gradients (Eq. 3.22), determined with the corresponding sets of $S_{2\omega_1}$ data. Although the agreement between the two electrostatic force gradients is good (there are no adjustable parameters), there exists a slight discrepancy between the two curves. The measured total force gradient difference is systematically about 3% higher than the values calculated from $S_{2\omega_1}$. If this discrepancy means that there is a small error in the determination of the electrostatic force gradient, then the measurement of the Casimir force gradient is almost unaffected. For example, for all $d < 120$ nm the electrostatic force gradient is always $< 25\%$ of the total force gradient, which results in an error of $< 1\%$ in the measurement of the Casimir force gradient. If, on the other hand, the mismatch is caused by the uncertainty in the determination of Δd with the dedicated fiber optic interferometer, then our Casimir force gradients are affected by a 3% systematic error. Nevertheless, this systematic error will not hamper the comparison between force gradient data obtained with different samples, as we always use the same Δd .

To measure the deflection sensitivity of the readout and the spring constant of the cantilever, we follow the procedure outlined above. In essence, we apply a big potential difference between the sphere and the plate, record both the cantilever deflection signal at $2\omega_1$ and $4\omega_1$ as a function of relative piezo-electric transducer displacement d_{pz} , and fit Eq. 3.19 to those data. In Fig. 3.10, we plot $V_{AC}\sqrt{S_{2\omega_1}/S_{4\omega_1}}$ as a function of d_{pz} for such a single dataset. The straight line represents the best fit with Eq. 3.19 (reduced $\chi^2 = 0.25$). The error bars were determined by measuring the absolute error in $S_{2\omega_1}$ and assuming that the error in $S_{4\omega_1}$ is equal and independent from the error in $S_{2\omega_1}$. This is not entirely correct, because some sources of error, like for example fluctuations in d , will lead to correlated variations in $S_{2\omega_1}$ and $S_{4\omega_1}$. We have thus overestimated the error in $V_{AC}\sqrt{S_{2\omega_1}/S_{4\omega_1}}$, which leads to a reduced $\chi^2 < 1$. Anyhow, the slope of the data allows us to extract $k/R = (11.12 \pm 0.06) \cdot 10^3$ N/m² (the uncertainty is obtained by setting reduced $\chi^2 = 1$). When we combine this value of k/R with the simultaneously determined $\kappa = 191.3 \pm 0.2$ nm/V, we find that $\gamma = (7.64 \pm 0.04) \cdot 10^7$ V/m. With this value of γ , we can now establish that the $S_{2\omega_1}$ set point we used for this dataset corresponds to a cantilever motion of 2 nm RMS at $2\omega_1$. It is interesting to observe that this 2 nm modulation of the separation d at $2\omega_1$ gives rise to a measurable signal at $4\omega_1$ even at 1 μ m distance. Furthermore, if we use the approximately known sphere radius of 100 μ m, we obtain the spring constant of our cantilever $k = 1.1$ N/m. As the nominal spring constant before sphere attachment and gold coating was 0.9 N/m, the value we find with this electrostatic method is very reasonable.

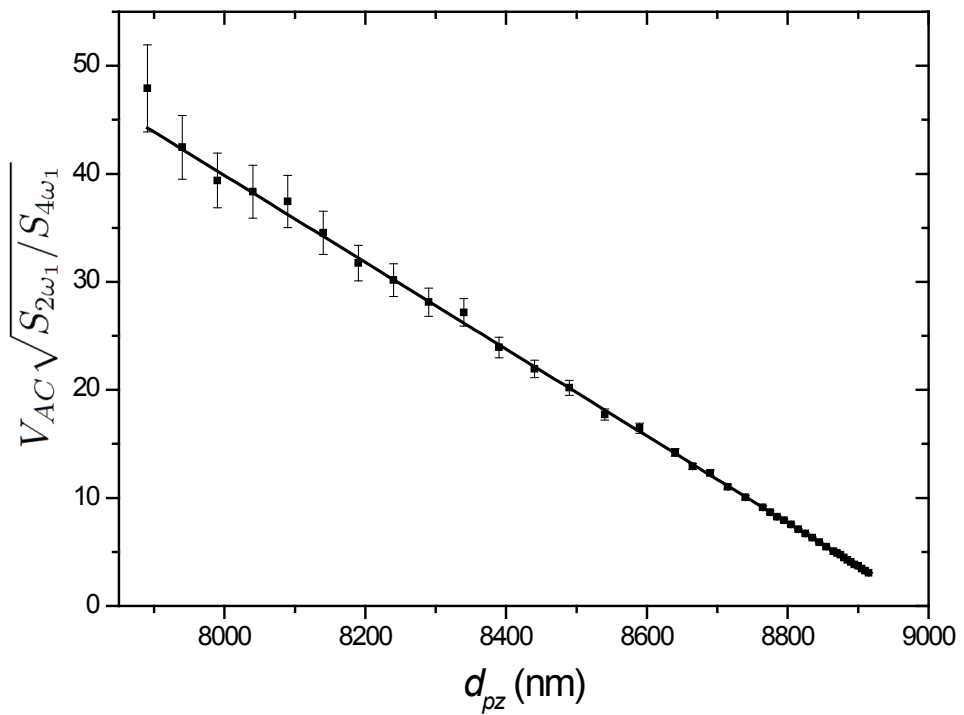


Figure 3.10: Plot of $V_{AC} \sqrt{S_{2\omega_1}/S_{4\omega_1}}$ as a function of piezoelectric transducer extension. The line represents the best fit of the data with Eq. 3.19 (reduced $\chi^2 = 0.25$). The slope of the fit can be used to obtain the cantilever spring constant and the deflection sensitivity γ .

With the deflection sensitivity calibrated, we can now assess the total cantilever bending and the precision in the measurements of the cantilever deflection. In the measurement runs presented in Figs. 3.6, 3.7 and 3.8, we used an $S_{2\omega_1}$ set point of 4 mV RMS, which corresponds to a cantilever motion of 52 pm RMS. Therefore, the static bending of the cantilever due to the electrostatic calibration procedure is 74 pm (see Eqs. 3.3 and 3.5). Anyway, this static bending is constant during the measurement run and it is thus automatically taken into account in the estimate of d_0 . The cantilever oscillations at ω_2 caused by the total force gradient and the hydrodynamic interaction are < 80 pm RMS for these measurement runs, which means that the corresponding static bending is < 113 pm. It is thus evident that we can safely neglect the static bending of the cantilever in our data analysis. Since the noise in $S_{2\omega_1}$ is 30 μ V RMS, the precision in the detection of the cantilever deflection is 400 fm RMS with our 1 s RC time (24 dB low-pass filter). This means that our setup has an RMS sensitivity of 1 pm/ $\sqrt{\text{Hz}}$ at $2\omega_1/2\pi = 144.4$ Hz.

Halving the Casimir force

We now present a comparison between two experiments performed with the same gold coated 100 μ m radius sphere and two different plates. The first experiment is conducted with a polished sapphire substrate coated with a gold film similar to the one deposited on the sphere. The general performance of our setup was discussed above by analyzing this first experiment. The second experiment consists of 580 measurement runs in which the plate is replaced by a float glass substrate with a sputtered ITO thin film on top (PGO CEC010S, typically $8.5 \Omega/\square$, or, equivalently, $\rho = 1.6 \cdot 10^{-4} \Omega\text{cm}$). After purchase, this sample has been exposed to air for more than two years before our measurements were performed.

Fig. 3.11 shows the Casimir force gradient between the two pairs of surfaces (Au-Au in green triangles, Au-ITO in red squares) [20]. In Fig. 3.11 a, we plot the force gradients as a function of separation on a double logarithmic scale for randomly chosen subsets of the data (150 out of 580 for both cases). Both datasets are obtained with the exact same settings for the electrostatic calibration and the force gradient measurement, and the Casimir force gradient is obtained from Eq. 3.11. The black lines indicate the theoretical force gradient, as will be explained below. Figs. 3.11 b and c present two histograms of all 580 Casimir force gradient measurements for both Au-Au and Au-ITO at separations $d = 120$ nm and $d = 80$ nm, respectively. It is clear that the interaction strength with the ITO sample is considerably reduced with respect to the gold plate.

Note that our estimate of d_0 , and thus d , relies on the simple form of Eq. 3.1 and is only valid for $d \ll R$ (PFA). This assumption is not entirely correct in the probed separation range [19] and results in a systematic error in d_0 of

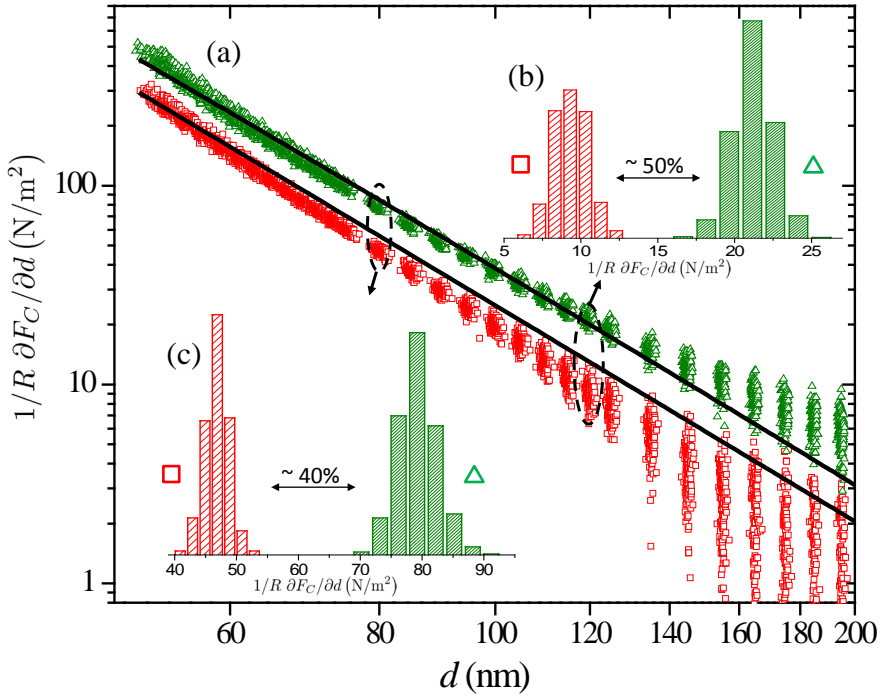


Figure 3.11: **a**, Casimir force gradient as a function of separation for the Au-Au (green triangles) and Au-ITO (red squares) interactions for randomly chosen subsets of the data (150 out of 580 for both cases) plotted on a double logarithmic scale, with the common electrostatic background subtracted from the data. The black lines correspond to the calculated Casimir interactions. **b**, Histogram of all 580 force measurements for both the Au-Au and Au-ITO measurements at $d = 120$ nm. The difference in Casimir force gradient is $\simeq 50\%$ between the gold and ITO measurements. **c**, Same as b, but for $d = 80$ nm. At this separation, the difference in the force gradient is $\simeq 40\%$.

about 1.4 nm. Still, the corresponding underestimate of the separation is equal for both the measurements with Au and ITO, and can thus be neglected in the comparison of the two experiments.

Concerning the compensation voltage, we observed that V_0 varies approximately 1 mV and 3 mV over the complete measurement range in the Au-Au and Au-ITO cases, respectively. These slight variations of V_0 do not compromise the measurement of the Casimir force at the current level of sensitivity. The value of V_0 drifts in time from -106 to -103 mV for Au-Au and from 72 to 50 mV for Au-ITO at $d = 100$ nm. It is also important to note that, during the whole duration of the experiment, we never observed any problem with electrostatic charging of the Au or ITO layers, which would have most likely resulted in erratic behavior of α and/or V_0 .

In order to compare the obtained Casimir force gradients with theoretical predictions, we have investigated the dielectric properties of our surfaces. In Fig. 3.12, we show the reflection and transmission spectra of the two plates, measured from the thin film side, in the frequency range from 0.5 to 6.5 eV. The black continuous lines represent the reflection and transmission spectra calculated from the literature. For Au, we used the values reported in [63]. The imaginary part of the dielectric function of ITO is constructed from a sum of Drude and Tauc-Lorentz models with the parameters from [64]. The real part of the dielectric function is calculated with direct Kramers-Kronig integration. The thickness of the ITO thin film is fitted by examining the interference fringes in the reflection and transmission spectra (taking into account the refractive index of the material) and turned out to be 190 nm, which is close to the typical thickness reported by the manufacturer (180 nm). The agreement between the spectroscopic measurements and these literature values is reasonable in the probed energy range. We want to stress that for Au there are no adjustable parameters whatsoever in Fig. 3.12, and that for ITO only the thickness was fitted. These results allow us to estimate the Casimir force expected in the two cases (Au and ITO) and compare the calculation with our measurements (see Eq. 3.12).

The theoretical Casimir interaction is calculated with the Lifshitz equation using the dielectric properties of our surfaces. For Au, we have extrapolated the data of [63] with a Drude model ($\omega_p = 9.0$ eV and $1/\tau = 0.035$ eV from [27]). For ITO, we used the model from [64] for all frequencies. The computed force gradient is plotted as the black lines in Fig. 3.11. The agreement between data and theory is reasonable, although we do seem to obtain different powers for data and theory. At small separation, the experimental curves are bending upwards, which is a sign of surface roughness effects [67]; the theoretical curves were calculated for perfectly smooth surfaces. Furthermore, the Au-Au data tend to give rise to a stronger force at large distance compared to theory, which is most likely caused by an artifact common to many AFM force measurements: the laser light is reflected from the planar sample into the photodetector giving

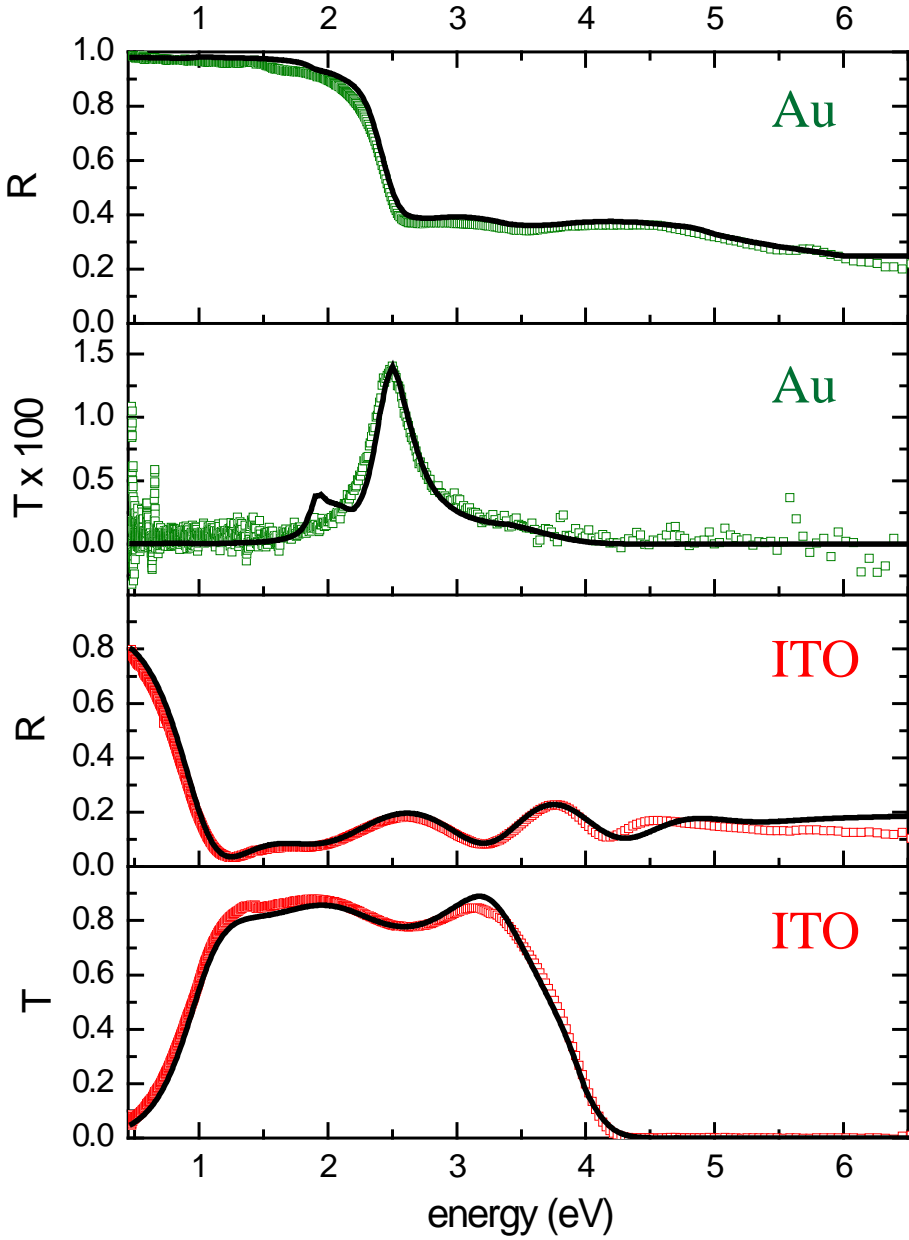


Figure 3.12: Measured reflection (R) and transmission (T) spectra as a function of photon energy for the Au on sapphire (green data) and ITO on float glass (red data) samples. The continuous black lines are calculations of the reflection and transmission spectra expected for our samples (no fit parameters except ITO layer thickness), using handbook data for gold [63] and a model from [64] for ITO. The transmission spectra for gold are zoomed in because the maximum transmission (around 2.5 eV) is only 1.4%. The calculation of the transmission spectrum of the ITO sample is quite sensitive to the choice of dielectric properties of the float glass for photon energies above 4 eV. The black lines describe the measured data reasonably enough to allow for calculations of the Casimir force.

rise to a background signal. In the Casimir force gradient method presented here, this artifact results, in first order, to an offset in the data; this explains the upwards trend of the data for large d . Although the precise distance dependence and strength of this artifact is unknown, we estimate from the force gradient data at large separation ($d > 500$ nm) that the associated systematic error is certainly < 2 N/m². In the case of the Au-ITO measurements, such a background signal is a lot smaller because ITO does not reflect well the laser light (see Fig. 3.12 at $\omega = 1.9$ eV). To explain the mismatch, it is therefore more likely that the model we used for the dielectric properties [64] is too metallic at low energy and that, consequently, the calculated Casimir interaction is too strong especially at large d .

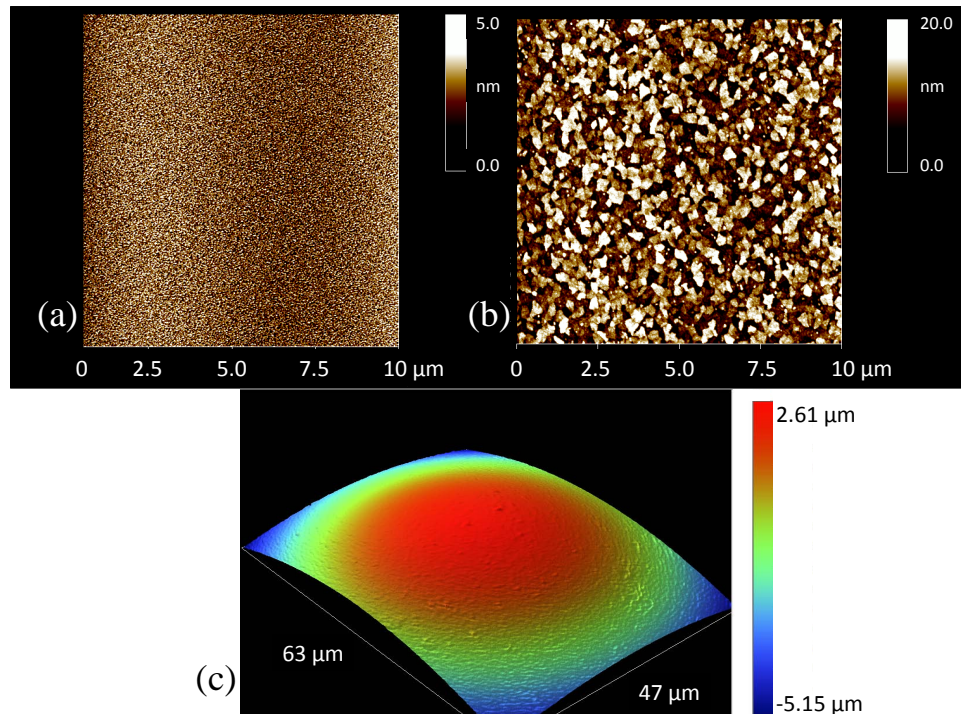


Figure 3.13: **a,b** AFM topography scans (10 by 10 μm) of the surfaces of the Au on sapphire and ITO on float glass samples, respectively. The surface roughness for the gold sample is 0.8 nm RMS, while the ITO plate has a surface roughness of 4 nm RMS. **c**, Optical profiler scan of the bottom of the gold coated polystyrene sphere that is attached to the cantilever for our force measurements. The surface roughness of the sphere is 3.8 nm RMS.

So far, we have neglected the effects of surface roughness in our analysis. In Fig. 3.13, we show topology measurement of our surfaces. Figs. 3.13 a and b are AFM tapping-mode scans (10 by 10 μm) of the Au on polished sapphire and ITO on float glass samples, respectively. The gold sample has an RMS surface roughness of 0.8 nm, while the ITO coated plate has a roughness of 4 nm RMS. Fig. 3.13 c presents a height profile of the surface of the sphere

bottom obtained with an optical profiler. Since the cantilever is mounted at a 15 degrees angle with respect to the planar sample surface (this is typical in AFM design), the top of this profile does not correspond to the area of closest approach in a force measurement. However, this height profile does give us the ability to estimate the surface roughness of the sphere, resulting in a value of 3.8 nm RMS.

Since we used the same sphere in both sets of measurements, the surface roughness of the sphere can never cause the observed difference in Casimir force gradients between the Au-Au and Au-ITO cases. Furthermore, we recall that surface roughness tends to enhance the strength of the Casimir interaction [67]. It is therefore impossible that the different surface roughnesses of the two planar samples is responsible for the difference reported in Fig. 3.11, because the ITO sample is considerably rougher than the gold coated sapphire substrate.

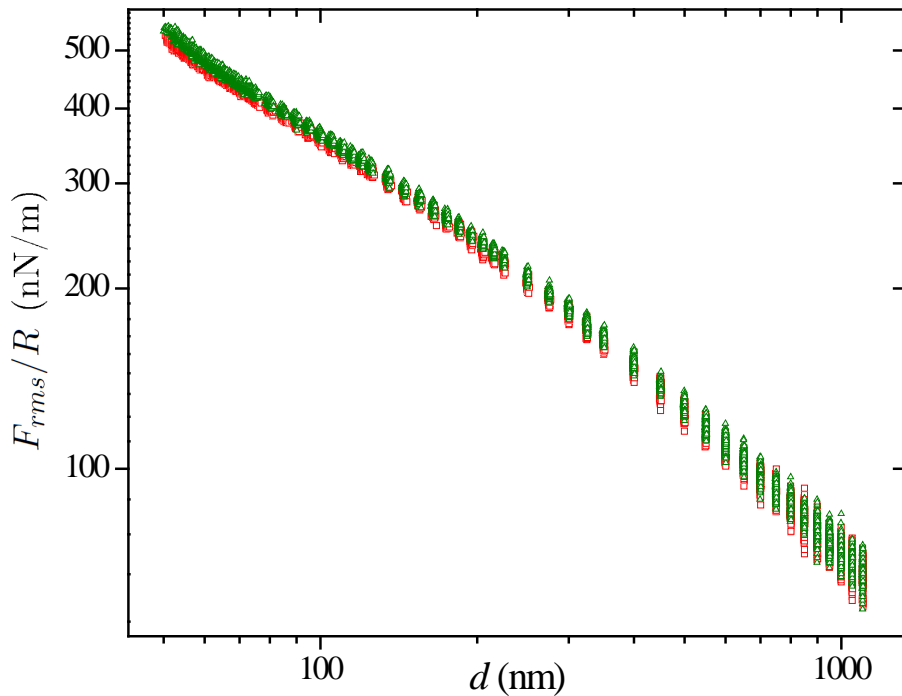


Figure 3.14: Hydrodynamic force (RMS) acting on the sphere as a function of separation for a subset of the data (150 out of 580 for both cases), caused by the oscillations of the plate surfaces at 119 Hz. The green triangles represent the force in the case of two gold-coated surfaces, while the red squares correspond to the Au-ITO interaction.

When we discussed the experimental details of our experiment, we mentioned the interesting feature that we can measure both the Casimir force gradient and the hydrodynamic force acting on the sphere with the same lock-

in amplifier at ω_2 . Fig. 3.14 shows the hydrodynamic force for both the Au-Au interaction (green triangles) and for the Au-ITO case (red squares). We have plotted the RMS force resulting from the 2.72 nm RMS oscillation of the plate at $\omega_2/2\pi = 119$ Hz. Both curves appear to change exponent at a separation of around 200 nm. This bending is caused by the slip of the air flow across the surfaces, i. e. the fluid velocity at the gas-solid interface is nonzero. This phenomenon is treated in [42] and the expressions derived in there describe our data satisfactorily. Concerning the comparison of the two sets of hydrodynamic data, it is clear that the hydrodynamic forces are very similar in the Au-Au and Au-ITO experiments. Still, there exists a small difference between the two curves of roughly 2%. This difference cannot be caused by an error in the determination of the initial separation d_0 , because both data sets are parallel on the double logarithmic plot. We suppose that the cause may lie in the different surface roughnesses of the Au and ITO samples that lead to different amounts of fluid slip over the sample surfaces.

It is worthwhile to compare our method for the detection of hydrodynamic forces with recent measurements obtained with AFM's [68, 69]. In [68], the cantilever with sphere is driven at its free resonance and the amplitude and phase of the cantilever motion are used to extract the hydrodynamic force. In [69], two methods were employed to measure the hydrodynamic interaction between a colloid sphere and a plate: measuring the static deflection of the cantilever during a fast approach of the planar sample and analyzing the thermal noise of the cantilever while slowly approaching the plate towards the sphere. In both papers, however, the separation between the two interacting surfaces was determined by bringing the sphere and plate into contact, a method that is prone to inaccuracies due to surfaces asperities (this is also reported in [69]). Since our method employs both a hydrodynamic force measurement and a precise calibration of the distance at the same time, we have developed a more reliable technique for hydrodynamic force measurements.

3.3.4 Conclusions

We have presented the experimental details of our Casimir force measurements between gold and ITO surfaces [20]. We have shown that the mechanical drift of our setup is less than 0.1 nm per measurement run and that our electrostatic calibration is performed with 0.2% precision. Force gradient data obtained over approximately 72 hours reveal no drift in the signal at all, confirming the high stability of the setup. Furthermore, we have introduced and demonstrated a new method to determine the spring constant of our cantilever and the deflection sensitivity of the AFM readout. We also presented our measurements of the Casimir and hydrodynamic interactions between the gold and ITO surfaces, and provided a complete characterization of our samples in terms of their dielectric properties and surface roughness.

Acknowledgments

The authors thank R. J. Wijngaarden, A. Baldi, F. Mul, and J. H. Rector for useful discussions. This work was supported by the Netherlands Organisation for Scientific Research (NWO), under the Innovational Research Incentives Scheme VIDI-680-47-209. DI acknowledges financial support from the European Research Council under the European Community's Seventh Framework Programme (FP7/2007-2013)/ERC grant agreement number 201739.

Chapter 4

Force measurements in gases

4.1 Introduction

In this chapter, we will discuss force measurements at short separation in the presence of different gases. Concerning the Casimir force, one can understand from the Lifshitz equation that the interaction strength, although it depends on the intervening medium between the interacting surfaces, is practically insensitive to the choice of gas (contrary to liquids). If one wants to tune the Casimir force with gases, it is thus mandatory to coat the interacting surfaces with materials whose surface dielectric properties depend on the specific gaseous surrounding. One of such materials are Hydrogen Switchable Mirrors (HSM): reflective metals that upon hydrogen absorption become transparent semiconductors or insulators. In 2004, Iannuzzi and co-workers at Harvard University performed Casimir force measurements between a gold plate and a sphere coated with a HSM in both argon and argon/hydrogen atmosphere. Unfortunately, they were unable to observe any change in the interaction strength upon hydrogen exposure. In Section 4.2 we perform a precise computation of the Casimir force between gold and HSM surfaces in both the hydrogen loaded and unloaded states, and show that the presence of a Pd capping layer covering the HSM dramatically reduces the difference in Casimir force for both states. In fact, this reduction is so strong, that the force contrast between both configurations is smaller than the resolution of the setup that was used in 2004, which clearly explains the negative result of the experiment.

The setup we describe in this thesis, however, is much more capable of Casimir force measurements in terms of stability and precision. We have therefore initiated a second round of Casimir force measurements with HSMs. In section 4.3, we present our force data between a Y/Pd HSM and a gold coated sphere. Interestingly, we were also unable to observe a decrease in the force upon hydrogen loading of the HSM, but found, on the contrary, a much stronger attractive interaction between the two surfaces in H_2 atmosphere. This strong interaction has most likely an electrostatic origin, and we will defend this claim by examining the distance dependence of the extra force and

of the contact potential.

The hydrodynamic interaction between the sphere and the plate depends, of course, also on which type of gas is present in the gap. In section 4.4, we present measurements of the hydrodynamic damping force in air, Ar, He, and SF₆. These gases span a wide range of mean free paths, by which we can effectively explore gas surface slip. In fact, although in He both the gas slip length and the mean free path are larger than the smallest gap size, it turns out that the continuous medium theory developed in 1973 by Hocking works flawlessly at these small separations.

4.2 On the use of Hydrogen Switchable Mirrors in Casimir force experiments

Abstract – Hydrogen Switchable Mirrors (HSMs) are shiny metals that become optically transparent upon exposure to hydrogen. The Casimir force between HSMs is thus supposed to be stronger in air than in hydrogen. A few years ago, an experiment designed to measure this effect gave an unexpected result (Iannuzzi D, Lisanti M and Capasso F 2004 *Proc. Nat. Ac. Sci. USA* **101** 4019–23): no change of the force was observed upon hydrogenation. Qualitative arguments show that this result is reasonable if HSMs do not switch at long wavelengths, where no measurements of the dielectric function are available. Because the exact composition of the mirrors used in that experiment is not known, a more quantitative comparison of the data with theory is not possible. Still, calculations of the Casimir force in the presence of similar HSMs of known composition might provide new insights for the interpretation of the experimental result and may suggest precious hints for the development of future analogous experiments. In this paper, we present calculations of the Casimir attraction between Mg_2Ni mirrors in air and in hydrogen. Our results clearly indicate that the modulation of the Casimir force with HSMs should be observable with modern set-ups.

4.2.1 Introduction

In the last decade, the literature dedicated to the Casimir effect [18] has been strongly influenced by a series of papers claiming the achievement of ultimate accuracy in the comparison of Casimir force experiments with theoretical predictions (see for example [70] and references therein). These papers have triggered a renewed interest in this field, stimulating a vivid discussion on the calculation of systematic errors of both experimental data and theoretical analysis. It is therefore not surprising that the large majority of modern experiments are performed using surfaces coated with thick, bulk-like metallic layers. From an experimental point of view, the use of metals offers the possibility to control and eliminate any residual electrostatic interaction that might disturb the measurements and increase the experimental uncertainty. Concerning the theoretical analysis of the data, the Casimir force between two objects is typically calculated by substituting the dielectric functions of their surfaces directly into the Lifshitz equation for van der Waals interaction [23]. The accuracy of the predicted results is thus strictly related to the degree of confidence with which those functions are known. The choice of bulk-like metallic films facilitates accurate calculations, because the dielectric functions of metals are known better than those of dielectrics. Measurements of Casimir forces between materials other than metals would thus not contribute to the discussion on the *accuracy issue*, giving rise to less impactful results.

It has been already recognized, however, that this trend represents a severe narrowing of the focus of modern literature [7, 32, 33, 71, 72]. The dependence of the Casimir force on the dielectric function of the interacting surfaces should not be considered only as an annoying detail that makes measurements and precise calculations more difficult. It should rather stimulate new experiments that explore the possibility of tailoring the Casimir effect using materials with suitably chosen dielectric functions.

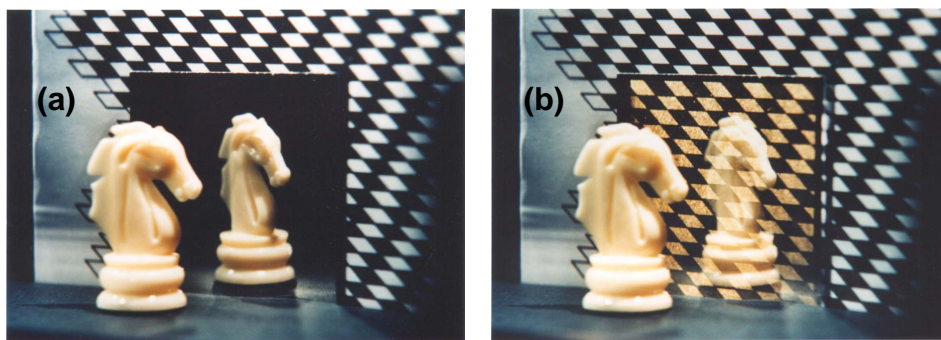


Figure 4.1: An image of a Hydrogen Switchable Mirror (a) before and (b) after exposure to hydrogen (courtesy of Ronald Griessen).

A few years ago, in the attempt to emphasize the importance of studies

that go beyond the accuracy issue, one of us (DI), in collaboration with M. Lisanti and F. Capasso, performed the first measurement of the Casimir force between Hydrogen Switchable Mirrors (HSMs) [32]. HSMs are materials that alter their dielectric properties upon hydrogen absorption [44] (see Fig. 4.1). They change from reflective conductors to transparent semiconductors or insulators when they are transferred from air to hydrogen. The effect is reversible; when the mirror is put back in air, it switches again to the reflective state. Because of this change of their optical properties upon hydrogen absorption and desorption, HSMs offer in principle the possibility to observe a reversible, *in-situ* change of the Casimir force between surfaces at fixed separation, a fascinating prospect from both a fundamental and technological point of view. According to the Lifshitz theory, the attraction between highly reflective metals is larger than the attraction between transparent dielectrics, which provide a less efficient confinement of the electromagnetic modes in the cavity formed by the two interacting surfaces. It should thus be possible to reduce the Casimir force between HSMs by exposing the mirrors to a hydrogen atmosphere; the force could then be brought back to higher values by replacing hydrogen with air. Surprisingly, the experiment reported in reference [32] was not capable of detecting any effect. In spite of the dramatic change of the optical properties of the mirrors, the Casimir force measured in hydrogen was not significantly different from that obtained in air. Due to the limited amount of information on the dielectric function of the HSMs used in the experiment, the authors could not present a rigorous theoretical calculation to compare with the data. Nevertheless, a mathematical exercise based on *ad hoc* materials with properly chosen dielectric functions made it possible to explain this unexpected result in terms of a counterintuitive property of the Lifshitz theory. Yet, a complete analysis of the magnitude of the effect is still missing, and one might wonder if there is a configuration for which a reversible change of the Casimir force between HSMs upon hydrogenation could be observed with modern experimental set-ups.

The goal of the present paper is to address this topic. First, we will briefly review the previous experiment and the mathematical arguments reported to explain the data. Then, we will discuss the switching properties of Mg_2Ni mirrors, HSMs with composition similar to the one used in the experiment. We will show that, although direct measurements of reflectivity and transmittivity are available only in a limited wavelength region, it is still possible to estimate the behavior of the dielectric function over a much broader spectrum by means of a simultaneous analysis of Hall effect and resistivity data. Finally, we will present the results of Casimir force calculation obtained by substituting these dielectric functions in the Lifshitz equation. We will demonstrate that the decrease of the attraction after hydrogenation of the mirrors is expected to be smaller than the sensitivity of the experiment discussed above, but sufficient to be observed with an updated version of that apparatus or with one of the

set-ups that, according to literature, can provide measurements of the Casimir force with 1% (or better) precision.

4.2.2 Casimir effect with Hydrogen Switchable Mirrors: previous experimental results

Measurements of the Casimir force using HSMs were reported in reference [32] (see also [71, 73]).

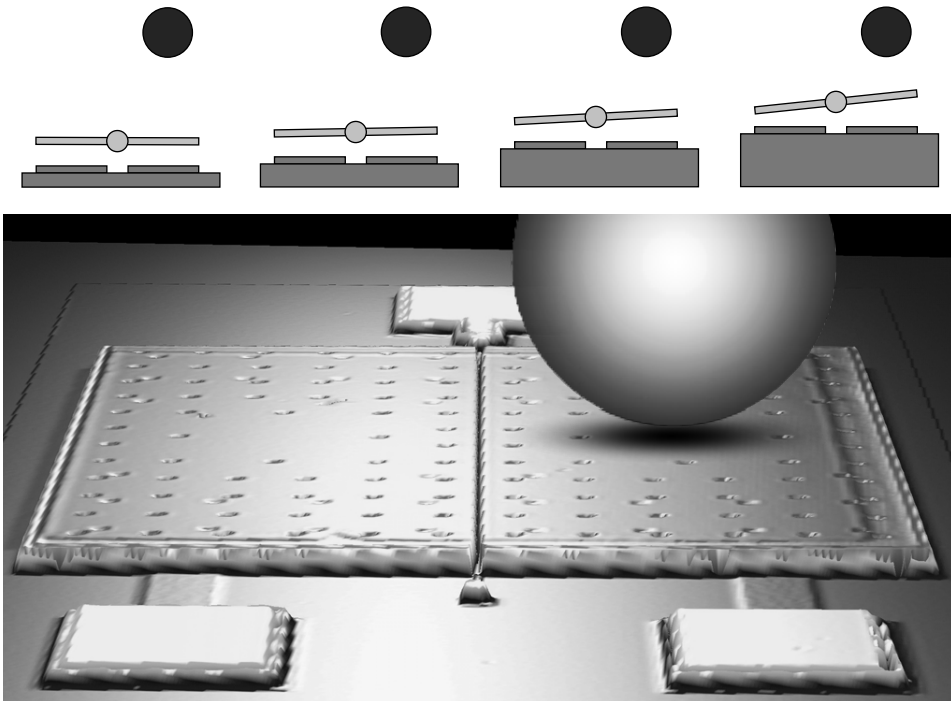


Figure 4.2: Schematic view of the experimental set-up that has been used for the measurement of the Casimir force between a gold coated plate and a sphere coated with a Hydrogen Switchable Mirror (not to scale) [32]. The four top panels illustrate the rotation of the micromachined *see-saw* in response of the Casimir interaction with the sphere.

The set-up used for the experiment is similar to the one originally developed at Bell Laboratories by H. B. Chan, F. Capasso, and their collaborators [2, 3] (see Fig. 4.2). The force sensor consists of a micromachined device that resembles a miniaturized *see-saw*. A polysilicon plate ($0.5 \times 0.5 \text{ mm}^2$ area), covered with a 5 nm thick chromium adhesion layer and a 200 nm thick gold coating film, is kept in suspension by means of two thin rods that depart from the middle point of two opposite sides of the plate and end onto a post anchored to the substrate. The two rods define the pivot axis of the *see-saw*. Two electrodes, located underneath the plate in a symmetric configuration with respect to the pivot axis, allow capacitive measurements of the rotation

of the top plate with accuracy on the order of 10^{-7} rad, which corresponds to a torque sensitivity of $\simeq 10^{-15}$ Nm.

The force sensor is mounted on top of a calibrated piezoelectric stage and aligned to a polystyrene sphere (100 μ m radius) in the position illustrated in Fig. 4.2. The separation between the sphere and the top plate of the see-saw can be varied by changing the voltage applied to the piezoelectric stage. For separations d smaller than $\simeq 400$ nm, the Casimir attraction between the sphere and the plate is sufficient to induce rotations of the see-saw that are larger than the experimental sensitivity. With this set-up, it is thus possible to carry out measurements of the Casimir force between the sphere and the plate from $d \simeq 400$ nm down to the jump-to-contact point, i.e., to that value of d where the restoring force of the torsional rods is not sufficient to overcome the attractive force between the two surfaces.

In this experiment, spheres were coated with a Pd-capped Mg-Ni HSM [74]. The mirror was fabricated by means of seven consecutive depositions of Mg-Ni layers, followed by a single deposition of a 5 nm thick palladium cap. Each Mg-Ni layer was obtained by evaporating a 2 nm thick nickel film on top of a 10 nm thick magnesium film. The palladium cap was added to promote hydrogen absorption [44], because, in the conditions of the Casimir force experiment (room temperature and less than atmospheric partial pressure of hydrogen) an uncapped HSM would have not spontaneously absorbed hydrogen. The presence of a metallic layer at the interface with the external environment had another important function, in that it allowed for the control of electrostatic interactions. In similar uncapped HSMs, the HSM-to-air interface quickly oxidizes. Accumulation of surface charges on the oxide film would have given rise to electrostatic forces that could have easily overcome the Casimir attraction. The deposition of the palladium cap on top of the HSM prevented this process to occur. Furthermore, the presence of a metallic interface, opportunely connected to a power supply, gave the possibility to control the potential difference between the two interacting surfaces, an essential element in all Casimir force experiments [25, 70].

Measurements of the Casimir force F_C between a HSM-coated sphere and the top plate of the see-saw were carried out as a function of separation d following the scheme described in reference [32]. We refer the reader to the original paper for a detailed explanation of the data acquisition technique. Here we only want to stress that this technique allows one to calibrate the set-up with electrostatic forces and to perform, simultaneously, F_C -versus- d measurements.

Measurements were carried out in air and in a 4% hydrogen-in-argon mixture at room temperature and nearly atmospheric pressure, and repeated using different spheres and force sensors. A comparison of the data obtained before and after hydrogen loading reveals that there was no significant change in the Casimir force upon hydrogenation of the HSM [32].

4.2.3 Casimir effect with Hydrogen Switchable Mirrors: qualitative analysis of the experimental results

The results reviewed above have been qualitatively explained in reference [32]. The dielectric function of Mg-Ni HSMs is known only in a wavelength region that approximately spans from $0.2 \mu\text{m}$ to $2.5 \mu\text{m}$ [74], where reflectivity switches from $\simeq 70\%$ to $\simeq 20\%$ upon hydrogenation. Very little information is available at longer wavelengths, where HSMs might not switch at all. It is thus important to understand whether those longer wavelengths contribute to the Casimir force between surfaces at sub-micron separation. If infrared modes are relevant and HSMs do not switch in the infrared spectrum, the decrease of the Casimir force might be too small to be observable with the experimental set-up described in the previous section. The following mathematical exercise demonstrates that infrared modes do play a significant role in the Casimir interaction at those distances, and that the change in the force upon hydrogenation is dramatically hampered if one assumes that these HSMs do not switch at long wavelengths.

The Casimir force between a plate made out of a material 1 and a sphere made out of a material 2 separated by a medium 3 can be calculated by plugging the dielectric functions of the interacting surfaces and of the intervening medium directly into the Lifshitz equation for van der Waals interaction [23]:

$$F_C(d) = \frac{\hbar R}{2\pi c^2} \int_0^\infty \int_1^\infty \varepsilon_3 p \xi^2 \left\{ \log \left[1 - \Delta_{31}^{(1)} \Delta_{32}^{(1)} e^{-x} \right] + \log \left[1 - \Delta_{31}^{(2)} \Delta_{32}^{(2)} e^{-x} \right] \right\} dp d\xi \quad (4.1)$$

where \hbar is the reduced Planck's constant, R is the radius of the sphere*, c is the speed of light in vacuum,

$$\Delta_{jk}^{(1)} = \frac{s_k \varepsilon_j - s_j \varepsilon_k}{s_k \varepsilon_j + s_j \varepsilon_k} \quad \Delta_{jk}^{(2)} = \frac{s_k - s_j}{s_k + s_j} \quad (4.2)$$

and

$$x = \frac{2d\sqrt{\varepsilon_3}\xi p}{c} \quad s_j = \sqrt{p^2 - 1 + \frac{\varepsilon_j}{\varepsilon_3}} \quad (4.3)$$

In Eqs. 4.1, 4.2 and 4.3, ε_j stands for the dielectric function evaluated at imaginary frequency, $\varepsilon_j(i\xi)$. This quantity is defined by the following relation:

$$\varepsilon_j(i\xi) = 1 + \frac{2}{\pi} \int_0^\infty \frac{\omega \varepsilon_j''(\omega)}{\omega^2 + \xi^2} d\omega \quad (4.4)$$

where $\varepsilon_j''(\omega)$ is the imaginary part of the dielectric function.

*Note that Eq. 4.1 relies on the *Proximity Force Approximation*, which is acceptable only if $R \gg d$

In the experiment described in the previous section, the intervening medium was either air or a hydrogen enriched gaseous mixture kept at room temperature and nearly atmospheric pressure. One can thus assume $\varepsilon_3(i\xi) = 1$ at all frequencies.

Following references [32, 71], we can now define an *ad hoc* material whose dielectric function (at real frequencies) is identical to that of gold, with the exception of a wavelength range that spans from λ_{min} to λ_{max} , where ε'' is assumed to be identical to zero. Using Eq. 4.1, we can then calculate the Casimir force between a sphere and a plate made out of this hypothetical material. If we assume that infrared modes do not contribute to the Casimir interaction, the values of ε'' at wavelengths larger than $\simeq 1 \mu\text{m}$ should not be of any relevance. The Casimir force expected for an *ad hoc* material with $\lambda_{min} = 1 \mu\text{m}$ and $\lambda_{max} = 200 \mu\text{m}$ should thus not differ from the attraction between two gold surfaces.

Calculations reveal that, on the contrary, the value of ε'' at long wavelengths is of great importance for a correct evaluation of the Casimir force at sub-micron separations. For $d = 100 \text{ nm}$, for example, the Casimir attraction between a sphere and a plate made out of an *ad hoc* material with $\lambda_{min} = 0.3 \mu\text{m}$ and $\lambda_{max} = 2.5 \mu\text{m}$ is only $\simeq 3\%$ smaller than that expected between gold surfaces. However, if one assumes $\lambda_{min} = 1 \mu\text{m}$ and $\lambda_{max} = 200 \mu\text{m}$, this difference becomes significantly higher, reaching $\simeq 35\%$.

This behavior is due to the fact that the Lifshitz equation (Eq. 4.1) is intimately connected to the dielectric function of the interacting materials calculated at imaginary frequencies, which can be obtained by means of Eq. 4.4. For every imaginary frequency $i\xi$, the imaginary part of the complex dielectric function ε'' is integrated over all real frequencies, with non-negligible contributions arising from a wide range of modes.

In the original paper [32], it was stressed that the theoretical discussion was not accounting for the presence of the thin palladium layer that was added on top of the HSM. The thickness of this coating film is smaller than the skin-depth and should intuitively not contribute significantly to the interaction. However, the authors suggested that a more rigorous calculation might reveal that this thin metallic layer plays a counterintuitive role. We will come back to this point in the next section.

4.2.4 Casimir effect with Hydrogen Switchable Mirrors: is the modulation of the force observable?

While the arguments reported above provide a reasonable qualitative explanation of the experimental results, it would be interesting to perform a rigorous comparison of the data with theory. Unfortunately, this is not feasible. It is known that the dielectric function of Mg-Ni HSMs strongly depends on their composition and on their hydrogen content upon hydrogenation [74]. Due to

the fabrication technique used in the experiment (consecutive deposition of thin layers of magnesium and nickel), it is not possible to establish the exact composition (neither before nor after hydrogenation) of those particular films, which might even have been non-homogeneous. Any attempt to provide a more quantitative comparison of the data with theory would inevitably be based on very rough approximations on the composition of the mirrors. These approximations would lead to ambiguous conclusions.

It is possible, however, to calculate the magnitude of the decrease of the Casimir force between similar HSMs of known composition. The results might provide a clear indication on the feasibility of an experimental observation of the effect, and might also emphasize potential problems that were not considered in the previous experiment.

To achieve this goal, we have calculated the Casimir attraction between a gold plate and a 100 μm radius sphere coated with a palladium capped Mg₂Ni mirror. The first step to perform the calculation is to evaluate the dielectric function of the HSM both in its reflective and in its transparent states (i.e., in air and in hydrogen, respectively).

It is known that, in the optical frequency range, HSMs can be well described by a Drude-Lorentz model [75]:

$$\varepsilon(\omega) = \varepsilon_\infty - \frac{\omega_p^2}{\omega^2 + i\frac{\omega}{\tau}} + \sum_j \frac{f_j}{\omega_{0j}^2 - \omega^2 - i\beta_j\omega} \quad (4.5)$$

The model includes a Drude contribution arising from the presence of free charge carriers with plasma frequency ω_p and relaxation time τ , and a series of Lorentz oscillators with strengths f_j , resonance frequencies ω_{0j} and damping terms β_j . Because Eq. 4.5 is analytic, the dielectric function at imaginary frequency can be simply obtained by substituting ω with $i\xi$:

$$\varepsilon(i\xi) = \varepsilon_\infty + \frac{\omega_p^2}{\xi^2 + \frac{\xi}{\tau}} + \sum_j \frac{f_j}{\omega_{0j}^2 + \xi^2 + \beta_j\xi} \quad (4.6)$$

The Drude-Lorentz parameters ω_p , τ , f_j , ω_{0j} , β_j , and ε_∞ for Mg₂Ni HSMs were obtained by Lohstroh *et al.*, who analyzed reflectivity and transmittivity measurements in the wavelength region spanning from ultraviolet to near infrared [76, 77]. According to their results, for mirrors in the reflective state (i.e., mirrors in air before exposure to hydrogen), one Lorentz oscillator and one Drude term are sufficient to reproduce the experimental data. For mirrors in the fully loaded transparent state (i.e., after complete hydrogenation, corresponding to Mg₂NiH_{4- δ} , with $\delta \simeq 0$), four Lorentz oscillators are necessary, but no Drude tail is needed[†]. Optical data, in fact, do not reveal any Drude-like

[†]We thank the authors for providing us with the values of the Lorentz parameters: $\varepsilon_\infty = 2.45$, $\sqrt{f_1} = 2.67$ eV, $\omega_{01} = 2.54$ eV, $\beta_1 = 0.40$ eV, $\sqrt{f_2} = 3.62$ eV, $\omega_{02} = 3.08$ eV, $\beta_2 = 0.69$ eV, $\sqrt{f_3} = 4.32$ eV, $\omega_{03} = 3.87$ eV, $\beta_3 = 1.40$ eV, $\sqrt{f_4} = 4.48$ eV, $\omega_{04} = 5.64$ eV,

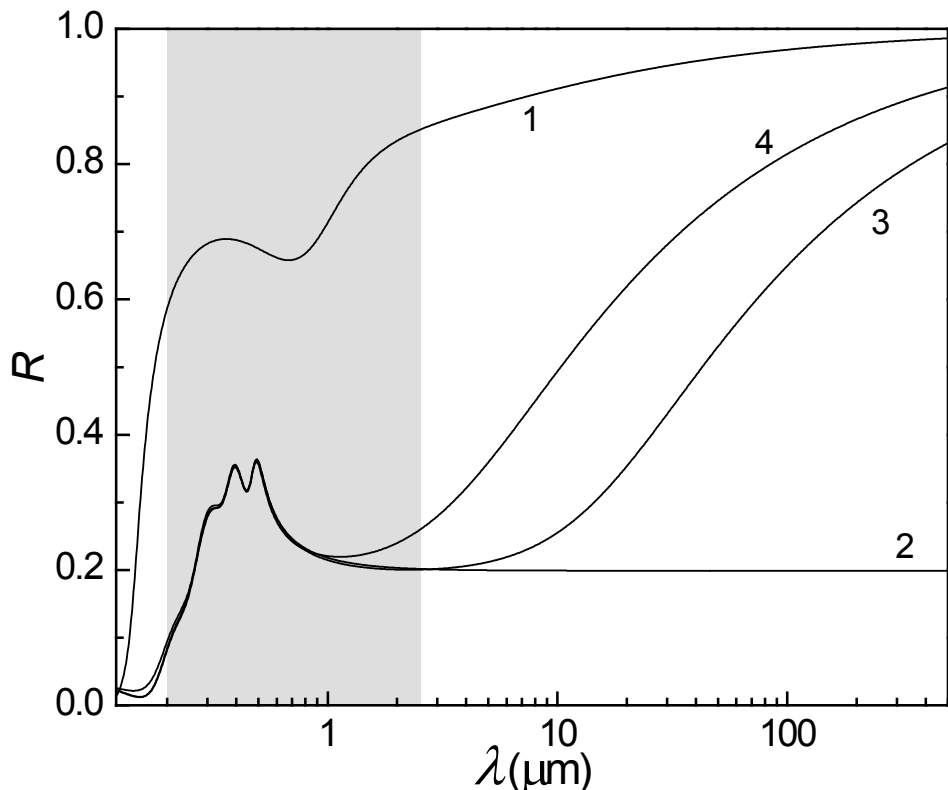


Figure 4.3: Reflectivity of Mg_2Ni Hydrogen Switchable Mirrors as a function of wavelength. The shaded area represents the wavelength region where experimental data are available. Curve 1 refers to a Drude-Lorentz model that fits the optical data of the mirror in its reflective state (before switching). Curve 2, 3, and 4 refer to hydrogenated Hydrogen Switchable Mirrors. Curve 2 represents a Lorentz model obtained by fitting the optical data. Curve 3 is equivalent to Curve 2, with the addition of a Drude term obtained from the combined analysis of Hall effect and resistivity measurements. Curve 4 is the sum of curve 2 and a Drude term with *ad hoc* plasma frequency and relaxation time.

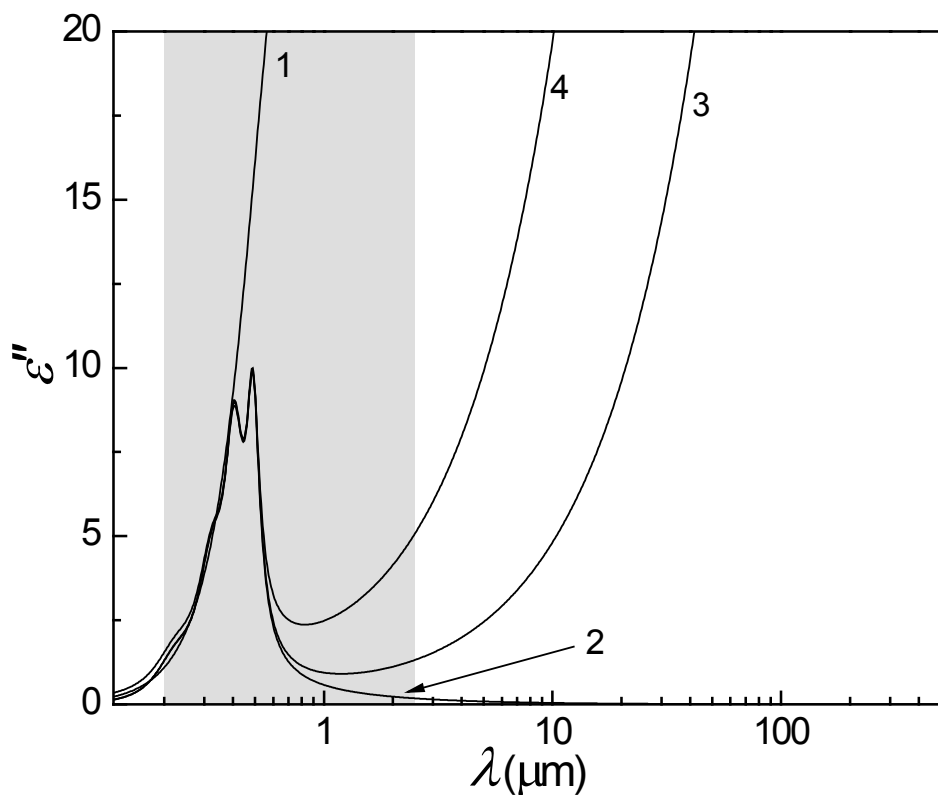


Figure 4.4: Imaginary dielectric function of Mg_2Ni Hydrogen Switchable Mirrors as a function of wavelength. Symbols are equivalent to those used in Fig. 4.3.

behavior up to the longer wavelengths investigated ($\simeq 2.5 \mu\text{m}$). To understand the relevance of this point, in Fig. 4.3 and Fig. 4.4 we plot, respectively, the reflectivity and the dielectric function of Mg_2Ni HSMs before and after switching. The shaded area represents the wavelength region where experimental data are available. Curve 1 refers to the fitting function proposed by Lohstroh *et al.* for Mg_2Ni HSMs before hydrogenation. Curve 2 corresponds to the fitting function proposed by the same group for the hydrogenated state, with four Lorentz oscillators and no Drude term. Curves 3 and 4 were obtained by us using the same function as in curve 2 with an additional Drude tail[‡]. The precise meaning of these curves will be clarified later in the text. Here we want to stress that curves 2 and 3, which have different behavior in the infrared, are very similar over the whole wavelength region where experimental data are available. None of these curves is thus in contradiction with the experiment. It is then evident that a correct extrapolation of the dielectric function at longer wavelengths cannot rely on these data. Unfortunately, these data still represent the only direct source of information available: to our knowledge, in fact, optical properties of HSMs have never been systematically measured beyond $\simeq 2.5 \mu\text{m}$ [§].

In the absence of more direct experiments, it is still possible to estimate the Drude term in fully hydrogenated Mg_2Ni HSMs by a combined analysis of Hall effect and resistivity measurements. Hall effect experiments provide a direct measurement of the density of free charge carriers n [79]. If resistivity is known, one can then calculate the dissipation factor and the plasma frequency of the Drude term using the following equations [79]:

$$\tau = \left(\frac{0.22}{\rho_\mu} \right) \left(\frac{r_s}{a_0} \right)^3 \times 10^{-14} \text{ sec} \quad (4.7)$$

$$\omega_p = 7.27 \left(\frac{a_0}{r_s} \right)^{3/2} \times 10^{16} \text{ rad sec}^{-1} \quad (4.8)$$

where ρ_μ is the resistivity in $\mu\Omega\text{cm}$, a_0 is the Bohr radius, and r_s is given by

$$r_s = \left(\frac{3}{4\pi n} \right)^{1/3} \quad (4.9)$$

Magnetoresistance and charge carrier density of Mg_2Ni HSMs were measured by Enache *et al.* for different hydrogen concentrations [80]. For fully loaded

$\beta_4 = 3.03 \text{ eV}$.

[‡]For curve 4, the oscillator strengths of the Drude-Lorentz model f_j were multiplied by a factor of 0.9.

[§]In reference [78], the authors reported measurements of the reflection and transmission coefficients up to $6 \mu\text{m}$. However, raw data were not analyzed in terms of the Drude-Lorentz model, and cannot be used in our calculations. It is however important to emphasize that those measurements do not reveal any Drude tail in the wavelength region between $2.5 \mu\text{m}$ and $6 \mu\text{m}$, still in agreement with curves 2 and 3.

mirrors, the authors obtained $n = 9.28 \cdot 10^{20}$ carriers/cm³ and $\rho = 12.9$ mΩcm.

We can now comment further on Fig. 4.3 and Fig. 4.4. We recall that curve 1 represents the HSM in its high reflectivity state[¶], and that curve 2 was obtained by fitting the optical data from visible to near infrared with four Lorentz oscillators and no Drude term. This model, which is equivalent to assume that HSMs become highly transparent at long wavelengths, is not consistent with Hall effect and resistivity measurements, and must thus be considered incorrect in the infrared spectrum. Curve 3 is equivalent to curve 2 plus a Drude term calculated according to the arguments reported above; it represents the best estimation of reflectivity and dielectric function of Mg₂NiH_{4-δ} (with $\delta \simeq 0$) that one can obtain with the data available in literature. Curve 4 is again an *ad hoc* model that will serve to stress once more the importance of infrared modes in the Casimir interaction. The properties of this hypothetical mirror are in contradiction with Hall effect and resistivity measurements.

At this point, we have enough information to model the Mg₂Ni mirrors in air (model 1) and in hydrogen (model 3), and to discuss the consequences that the use of erroneous models for the hydrogenated state would have in the calculation of the Casimir force upon hydrogenation (models 2 and 4). The presence of a thin palladium layer deposited on top of the mirror can be introduced in the calculation by means of a model developed by Parsegian and Ninham [81], according to which the Casimir force between a material 2 and a material 1 covered with a cap layer 4 of thickness t_4 , immersed in a medium 3, is obtained from Eq. 4.1, replacing $\Delta_{31}^{(1,2)}$ with

$$\Delta_{31}^{(1,2)} \rightarrow \frac{\Delta_{34}^{(1,2)} + \Delta_{41}^{(1,2)} e^{-\frac{xt_4s_4}{pd}}}{1 + \Delta_{34}^{(1,2)} \Delta_{41}^{(1,2)} e^{-\frac{xt_4s_4}{pd}}} \quad (4.10)$$

In order to run the calculation, it is still necessary to evaluate the dielectric function of the gold plate and of the palladium layer. For these materials, we use the tabulated data for the corresponding bulk metal [63] plus a Drude term as described in reference [27] (for gold) and reference [82] (for palladium).

In Fig. 4.5 we report the results of the calculations. The graphs show the decrease of the Casimir force between a gold plate and a 100 μm sphere coated with a Mg₂Ni HSM, alternatively exposed to either air or hydrogen. F_R and F_T indicate the force for the reflective state and for the optically transparent hydrogenated state, respectively. d is the separation between the sphere and the plate. Different curves refer to different models of the hydrogenated state (see table 4.1), and have been numbered in accordance with Figs. 4.3 and 4.4. Curves 2, 3, and 4 were obtained neglecting the presence of the palladium film. Concerning curve 3-Pd, a 5 nm thick palladium layer was added to the

[¶]It is interesting to note that, for the reflective state (Mg₂Ni), the combined analysis of Hall effect and resistivity measurements gives rise to plasma frequency and dissipation factor values that are in agreement with those obtained from optical data [76].

Material	Description
HSM reflective state Model 1	1 Lorentz Oscillator (Ref. [76]) plus Drude term: $\omega_p = 1.24 \cdot 10^{16} \text{ rad/s}; \tau = 9.9 \cdot 10^{-16} \text{ s}$
HSM hydrogenated state Model 2	4 Lorentz Oscillators (Ref. [77]) No Drude term
HSM hydrogenated state Model 3	4 Lorentz Oscillators (Ref. [77]) plus Drude term: $\omega_p = 0.17 \cdot 10^{16} \text{ rad/s}; \tau = 2.96 \cdot 10^{-16} \text{ s}$
HSM hydrogenated state Model 4	4 Lorentz Oscillators (Ref. [77])* plus Drude term: $\omega_p = 1.43 \cdot 10^{16} \text{ rad/s}; \tau = 1.82 \cdot 10^{-17} \text{ s}$
Gold surface	Tabulated data (Ref. [63]) plus Drude term: $\omega_p = 1.37 \cdot 10^{16} \text{ rad/s}; \tau = 1.88 \cdot 10^{-14} \text{ s}$ (Ref. [27])
Palladium layer	Tabulated data (Ref. [63]) plus Drude term: $\omega_p = 0.83 \cdot 10^{16} \text{ rad/s}; \tau = 4.28 \cdot 10^{-14} \text{ s}$ (Ref. [82])

Table 4.1: Summary of the models used for the calculations reported in the text. The asterisk added in the description of model 4 indicates that, for this particular model, the oscillator strengths of the Lorentz term have been multiplied by a factor 0.9.

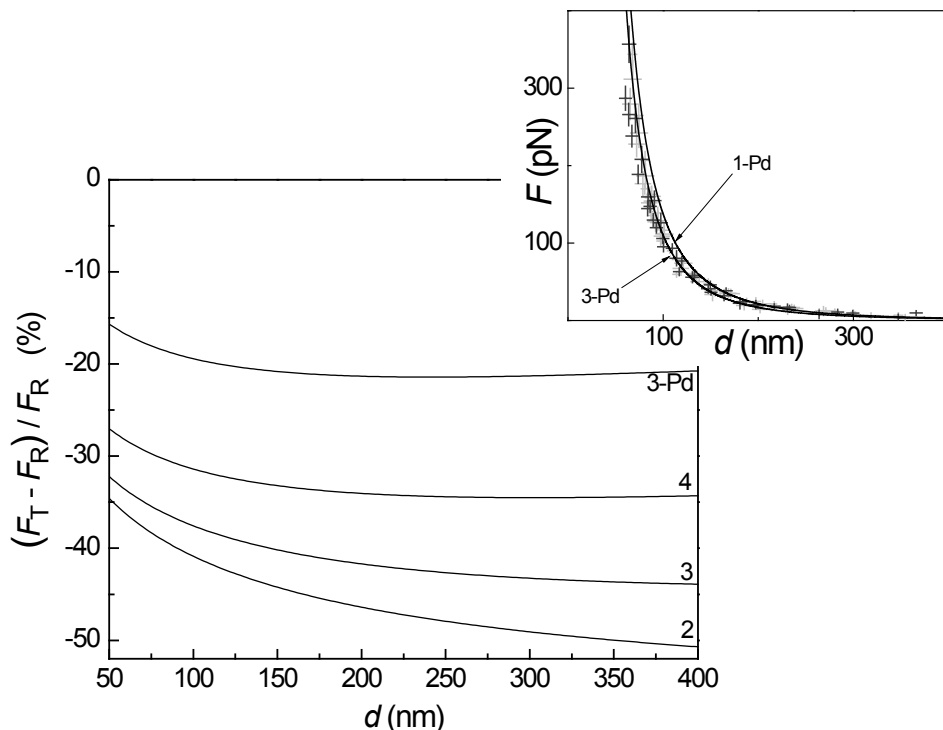


Figure 4.5: Expected decrease in the Casimir force between a gold plate and a $100 \mu\text{m}$ radius sphere coated with a Hydrogen Switchable Mirror exposed to either air or hydrogen. F_R and F_T indicate the force for the reflective state and for the transparent hydrogenated state, respectively. d is the separation between the sphere and the plate. Calculations were performed using the dielectric functions reported in Fig. 4.4 (see also table 4.1). Different curves refer to different models of the hydrogenated state, and have been numbered in accordance with Figs. 4.3 and 4.4. The suffix "Pd" indicates whether the 5 nm thick palladium coating layer was taken into account in the calculations or not. Inset: comparison of the results of the calculations with the experimental data reported in reference [32]. Light and dark gray symbols refer to measurements performed in air and hydrogen, respectively.

calculation of both F_T and F_R . From this graph, two important conclusions can be drawn.

- Curves obtained with no Drude term (curve 2), with the correct Drude term (curve 3), and with the fictitious Drude term (curve 4) are significantly different. This result emphasizes once more that if one assumes that hydrogenated HSMs remain highly reflective at long wavelengths, the decrease of the force upon hydrogenation is much smaller than that expected with a wide band switching mirror. Long wavelengths are thus indeed relevant, as already pointed out in reference [32].
- The 5 nm thick palladium capping layer deposited on top of the HSM plays a dramatic role in the interaction. At 100 nm separation, the change of the Casimir force upon hydrogenation for an uncapped mirror is larger than 35% (curve 3); if the palladium layer is added (curve 3-Pd), the effect reduces to $\simeq 20\%$. Further calculations show that a 10 nm thick palladium would decrease the change of the force at 100 nm to $\simeq 10\%$. The palladium layer represents a serious obstacle for the observation of large Casimir force modulations.

In the inset of Fig. 4.5 we report a direct comparison of the calculations with the experimental data of reference [32]. We want to stress once more that the curves represent the results of calculations performed using the properties of materials that probably have a different composition with respect to the ones used in the experiment. Nevertheless, the graph allows us to emphasize that, even in the *best case scenario* of fully loaded HSMs with fairly good switching properties in the infrared, the effect could have been hardly observed with the experimental sensitivity of the set-up described in [32].

It is to note that our calculation relies on the hypothesis that the HSM in use undergoes full hydrogen loading upon hydrogenation. Partial loading would significantly alter the result. It is known, in fact, that the loading process in Mg_2Ni HSMs (and, more generally, in most of Mg-Ni compounds) involves a remarkable self-organized double layering [83]. Hydrogen first penetrates inside the film and quickly reaches the substrate, from where hydrogenation starts (see inset of Fig. 4.6). Partial loading leads to a bi-layered structure formed by a transparent layer close to the substrate and a non-switched metallic layer close to the palladium film. This non-switched metallic layer is still highly reflective. Its presence would have a dramatic effect on the Casimir force, as it increases the overall thickness of the metallic film above the hydrogenated part of the mirror (see Fig. 4.6). Note that it is not possible to establish whether the HSMs used in the experiment of reference [32] were fully loaded. The presence of a non-switched layer below the palladium film might have contributed to reduce the magnitude of the Casimir force difference between measurements in air and in hydrogen.

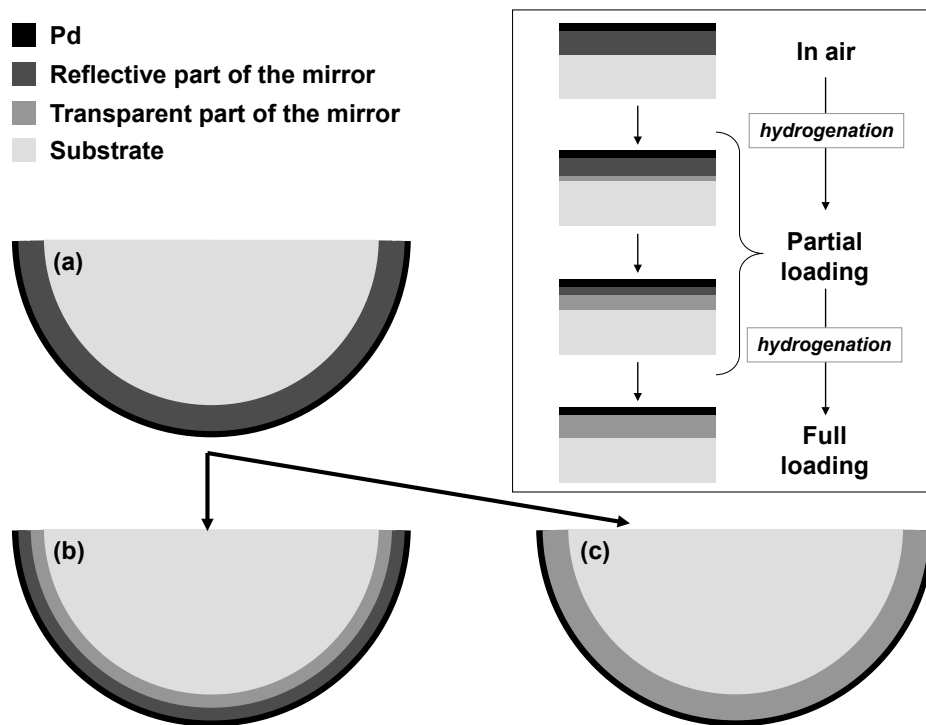


Figure 4.6: Schematic view showing that partial loading of Hydrogen Switchable Mirrors plays a detrimental role in Casimir force modulation experiments. Sketch (a) refers to the mirror before hydrogenation; sketch (b) shows the layered structure that would form in case of partial hydrogen loading, with a relatively thick reflective layer still present at the interface; sketch (c) illustrates the absence of layered structures at the interface in fully loaded mirrors. Inset: schematic diagram of the hydrogen loading mechanism in Mg-Ni Hydrogen Switchable Mirrors.

Our analysis also neglects the correction to the Casimir force due to the surface roughness of the interacting objects. These corrections cannot be explicitly calculated *a priori*, because the morphology of HSMs strongly depends on the deposition technique [84]. In this respect, it is worth stressing that the surface profile of HSMs in air undergoes large variations during the first few hydrogen loading and unloading cycles [84, 85], after which no more morphological adjustments are observed. Therefore, reproducible modulations of the Casimir force with HSMs can be achieved only after the mirrors have been switched a few times. It is also evident that for a correct interpretation of the data, accurate measurements of the morphology of the surfaces both in air and in hydrogen are needed, because the alteration of the roughness upon hydrogenation could mimic or hinder the decrease of the Casimir force induced by the change of the optical properties of the mirrors.

4.2.5 Conclusions

Tuning the Casimir force with HSMs is a fascinating opportunity that calls for deeper investigations. The only measurements reported so far [32] were affected by a relatively large experimental error, which was mainly due to the fact that the experiment was carried out at atmospheric pressure. The change in the force upon hydrogenation was smaller than intuitively expected, and was not sufficient to be observed. A qualitative theoretical analysis first showed that the results could have been explained assuming that the dielectric function of HSMs switches only in a limited wavelength region that spans from ultraviolet to near infrared, where optical data are available [32]. Longer wavelengths play in fact an important role in the interaction: if the mirror remains highly reflective in the infrared part of the spectrum, the change in the force upon hydrogenation can be smaller than the experimental sensitivity. A more complete theoretical analysis of the experiment was not performed, because the exact composition of the mirrors was not known.

In this paper we have calculated the expected decrease of the force for similar mirrors of known composition (Mg_2Ni). The results confirm the main conclusion of reference [32]: for an accurate comparison of experimental data with theory it is necessary to know the value of the dielectric functions of the interacting materials over a broad wavelength range that extends up to the far infrared region. Furthermore, the presence of a palladium capping layer strongly reduces the effect. Still, at 100 nm separation, the Casimir force is expected to decrease $\simeq 20\%$ upon full hydrogenation. We thus believe that it is possible to design a new experiment for the first observation of an *in situ* modulation of the Casimir force between HSMs. A significant reduction of the experimental uncertainty can be obtained by performing the measurements in vacuum. It is known that, in vacuum, hydrogenated HSMs do not release hydrogen. One could thus load or unload the mirror by flushing the measuring

chamber with proper gases at atmospheric pressure (hydrogen for loading, and air for unloading), and then pump vacuum during Casimir force measurements. In order to obtain a more pronounced effect, it would be also desirable to reduce the contribution of the thin palladium layer deposited on top of the HSM. The use of films thinner than 5 nm is in principle a possible solution to this problem. However, the resulting layer would probably be discontinuous after switching [85] and would not allow a complete control of electrostatic forces. A possible alternative is to replace palladium with a metal that wets the mirror better than palladium does, and then use hydrogen diffusion from a palladium pad located away from the interaction region (i.e., away from the portion of the sphere that, upon assembling of the experimental set-up, stands in front of the force sensor) to obtain uniform switching [86, 87]. This choice might allow one to reduce the thickness of the cap layer down to 2 or 3 nm. A more precise experiment would also probably stimulate a more accurate comparison with theory. Direct measurements of the dielectric functions in the infrared wavelength region and of the surface morphology of the films deposited onto the interacting surfaces would certainly facilitate a rigorous interpretation of the experimental data.

Acknowledgements

We are particularly indebted with J. N. Munday for his initial contribution to this work, and to R. Griessen for his critical analysis of the manuscript. We thank D. Borsa, C. Broedersz, F. Capasso, B. Dam, W. Lohstroh and R. Westerwaal for useful discussions, and the Netherlands Organisation for Scientific Research (NWO) for financial support, which was granted through the Innovational Research Incentives Scheme *Vernieuwingsimpuls* VIDI-680-47-209.

4.3 Force measurements in H₂ gas

Abstract – We present force measurements between a gold coated sphere and a planar sample coated with a Y/Pd hydrogen switchable mirror. Measurements were performed in air, argon and argon/hydrogen mixture. First, we prove that our setup is capable of working in hydrogen atmosphere by analyzing our measurements of the hydrodynamic force. Then we show that in hydrogen atmosphere, the force gradient detected between the sphere and the plate is much stronger than expected. A comparison of these data with data in pure argon suggests that this extra force gradient component has an electrostatic origin, since it follows a power law with relatively small exponent -2.35. Third, we present the simultaneously acquired contact potential measurements and show that although V_0 is rather constant as a function of separation in argon, it strongly depends on the distance in the argon/hydrogen mixture. This observation further enhances our suspicion that the stronger force gradient measured in hydrogen atmosphere has an electrostatic origin.

In the previous section, we have calculated the force between a Mg/Ni switchable mirror and a gold sphere in both the hydrogen loaded and unloaded states of the mirror. We concluded that the change in force upon hydrogenation of the HSM should be around 20%. With the current experimental setup, such a change should be easily observable. Therefore, we have upgraded our system such that it can work in hydrogen atmosphere at ambient pressure. We have fabricated a leak-tight chamber with electrical and fiber-optic feed-throughs in which the Casimir setup is placed. This chamber is anchored to the active anti-vibration stage that is placed inside our anechoic box. The chamber can be opened by removing the top half to access the Casimir setup for AFM laser alignment and sample placement. Since the vertical position of the position sensitive photodetector inside the AFM head has sometimes to be adjusted to account for slow drifts, we have equipped the associated control-knob with a stepper motor. This stepper motor can be controlled with sufficient precision with the computer. In Fig. 4.7 we show two pictures of the upgraded gas-capable setup. Fig. 4.7 a shows the setup with the top cover removed and photograph b is taken with the chamber closed for experiments in gaseous atmosphere. Experiments were carried out in air, argon and argon/hydrogen mixtures. The maximum partial pressure of hydrogen that we used is 40 mbar, as we used a maximum concentration of 4% H₂ in Ar at 1 bar. We were reluctant to increase hydrogen content, because several parts of the setup, most notably the feedback controlled piezoelectric transducer (PI) and the Veeco AFM head, are not warranted to survive operation in hydrogen atmosphere. Retrospectively, we can say that a 4% hydrogen in argon mixture does not compromise the workings of our setup.

As a first test to understand whether we would be able to observe the reduction of the Casimir force associated to hydrogen loading of a switchable mirror, we mounted an Y based mirror in the setup. The sample consists of a 30 nm Y layer sputtered on a 10 by 10 mm polished sapphire substrate, followed by a 5 nm Pd cap layer to facilitate the catalytic splitting of the H₂ molecules needed for the absorption of the hydrogen atoms by the Y layer. We chose to use Y as a switchable mirror because it is much easier to fabricate than a Mg/Ni mixture of the right composition. As the other surface we used the gold coated sphere that we also used for the experiments presented in chapter 3. When we coated the sphere in 2008, a metallic layer consisting of a Ti adhesion layer and a 100 nm Au film was sputtered onto it.

For all experiments presented in this section, we used the same experimental procedure as outlined in detail in section 3.3. The distance between the sphere and the plate is decreased in discrete steps, we always apply a bias voltage to compensate for V_0 , and we measure the electrostatic force, the total force gradient and the hydrodynamic force between the two surfaces. In the experiments presented in this section, we have always started the measurement series with reference runs in air. Afterwards, we purged the chamber with pure

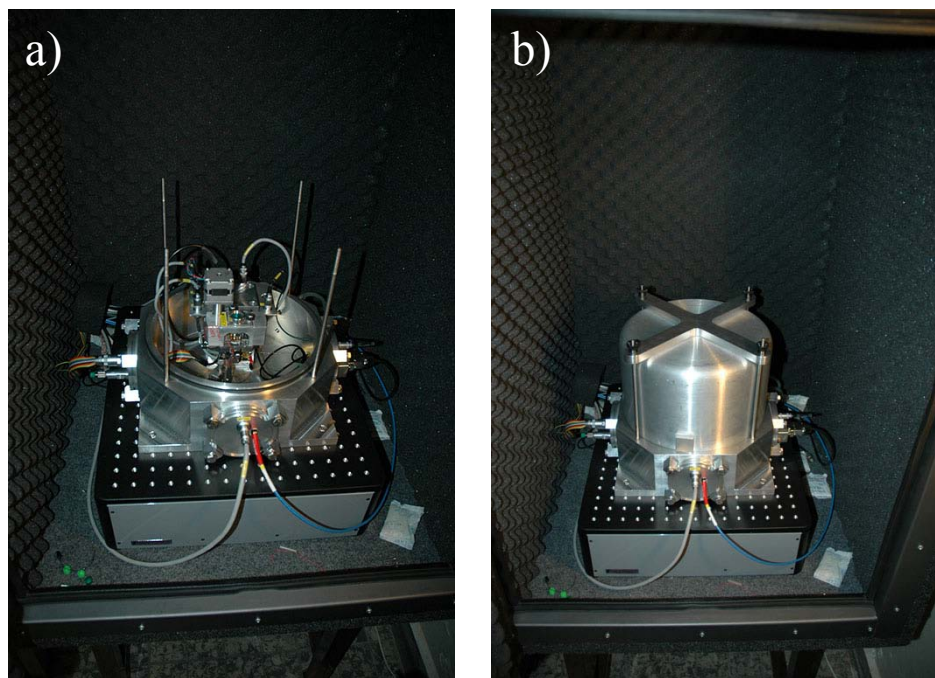


Figure 4.7: Photographs of the experimental setup after the upgrade for measurements in controlled gaseous atmospheres. In **a**), the top cover is removed for laser and detector alignment and sample placement. In **b**), the setup is closed and ready for gas flushing.

Ar gas for approximately 1 hour with a flush rate of around 2 liters per minute (the unoccupied volume of the chamber is 13 liters). We can thus assume that the chamber is filled completely with argon for all practical purposes. We now carry out measurement in Ar atmosphere. Then we flush the system with a 4% H₂ in Ar mixture using the same procedure, and perform measurements in this hydrogen enriched atmosphere. Finally, we flush the system again with pure Ar to compare with the previous runs in argon and to verify whether the system was modified or not by exposing it to hydrogen gas.

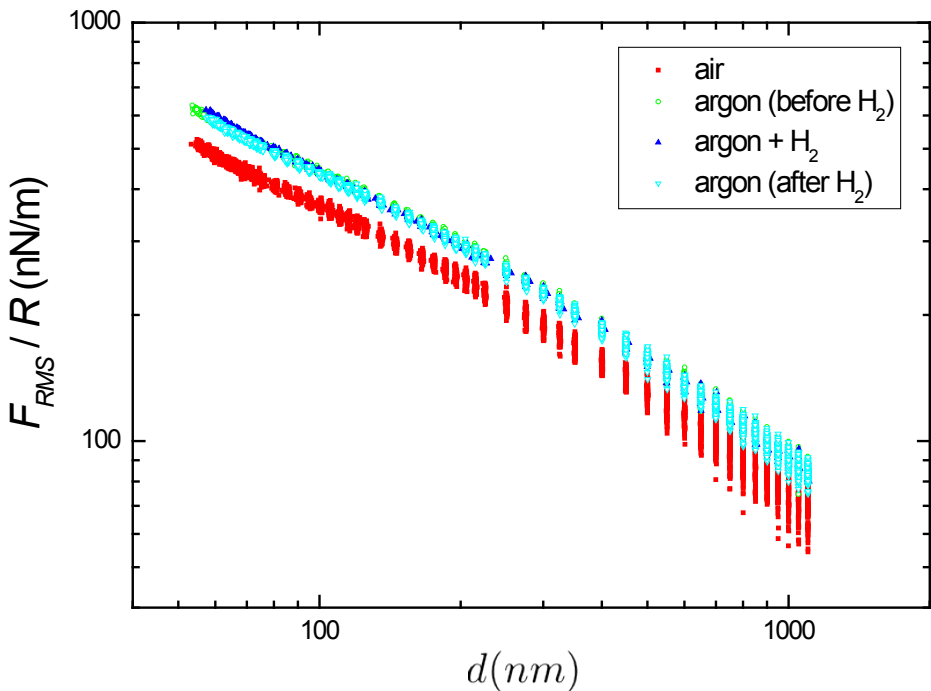


Figure 4.8: RMS hydrodynamic force divided by the sphere radius ($R \simeq 100 \mu\text{m}$) as a function of separation between the sphere and plate surfaces. Experiments are carried out in the following order: air (red squares), argon (green circles), argon with 4% hydrogen (blue upward triangles), and pure argon again (cyan downward triangles).

In Fig. 4.9, we present measurements of the hydrodynamic force due to the small oscillation of the piezoelectric stage. We have plotted the RMS force as a function of distance on a log-log scale. The presented data represent the force divided by the sphere radius (approximately 100 μm), because of the way the calibration procedure works. The oscillation of the plate surface is executed with an amplitude of 3.85 nm and a frequency $\omega_2/2\pi = 119 \text{ Hz}$. The measurements of the forces in air, argon, argon/hydrogen mixture, and pure argon after removing the H₂ are represented by the red squares, green circles, blue upward triangles and cyan downward triangles, respectively. Clearly, the

hydrodynamic interaction is weaker in air than in the other two gases, which is caused by the lower viscosity of air with respect to Ar. Furthermore, the measured hydrodynamic signals in Ar and Ar/ H_2 are very similar, which is consistent with the idea that the presence of a small amount of H_2 in Ar does not significantly change the viscosity. Moreover, these data also proof that our setup is working properly in the argon/hydrogen mixture, i.e. the calibration and piezo oscillation are not affected by the presence of the H_2 gas.

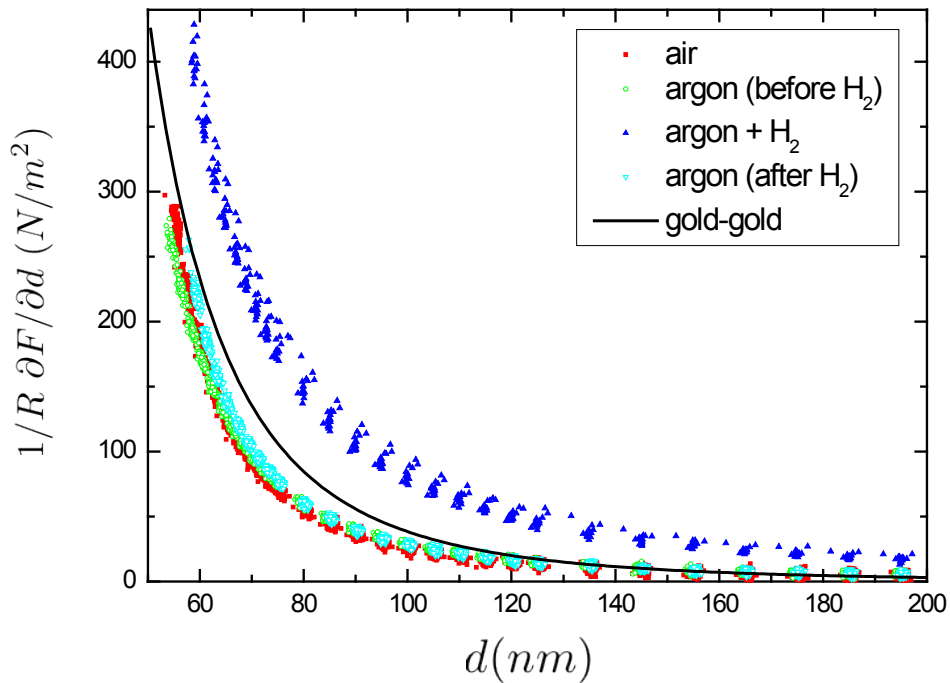


Figure 4.9: Force gradient between the Y/Pd mirror and the gold coated sphere as a function of separation. Experiments are carried out in the following order: air (red squares), argon (green circles), argon with 4% hydrogen (blue upward triangles), and pure argon (cyan downward triangles). The black line indicates the theoretical Casimir interaction between two gold surfaces.

In Fig. 4.9, we present measurements of the total force gradient as a function of separation, corrected for the electrostatic background gradient caused by the simultaneous calibration procedure (see section 3.3). We have seen in the previous chapter that this quantity can typically be modeled correctly by considering only the Casimir interaction. The force gradients in the cases of air, argon, argon/hydrogen mixture, and argon for the second time, are represented by the red squares, green circles, blue upward triangles and cyan downward triangles, respectively. The black line indicates the Casimir force gradient for the interaction between two gold surfaces, which should be very similar to the interaction between our unloaded Y/Pd switchable mirror and the gold sphere.

A fascinating observation is that the force gradient in the Ar/H₂ gas is much stronger than in Ar or air. Moreover, when we remove the hydrogen gas and measure for the second time in pure Ar (cyan downward pointing triangles), we recover the force gradient we measured before in Ar: the effect is reversible. The physical mechanism that underlies this extra force gradient is unclear at the time of writing, although we will try to shed some light on the origin of the effect later in this section. The second observation is that the force gradients we measured in air and in argon are too small compared to the expected Casimir force. This is not caused by the dielectric properties of the mirror, as we checked that measurements performed later on with the same sphere and a gold sample provide similar data (contrary to the measurements presented in chapter 3). We therefore expect that the exposure of this sphere to hydrogen has somehow changed its surface: a particular role could have been played by the Ti adhesion layer that is known to absorb hydrogen. We would like to point out that although the run in Ar/H₂ was the first exposure to hydrogen in this particular experiment, the sphere was already exposed multiple times to hydrogen in earlier experiments, which explains why the data in air and Ar before H₂ purging are already below the theory. Anyhow, the results presented in Fig. 4.9 are certainly not compatible with the expected reduction in the force upon exposure to hydrogen as predicted in the previous section, as we have observed a significant increase in the interaction strength.

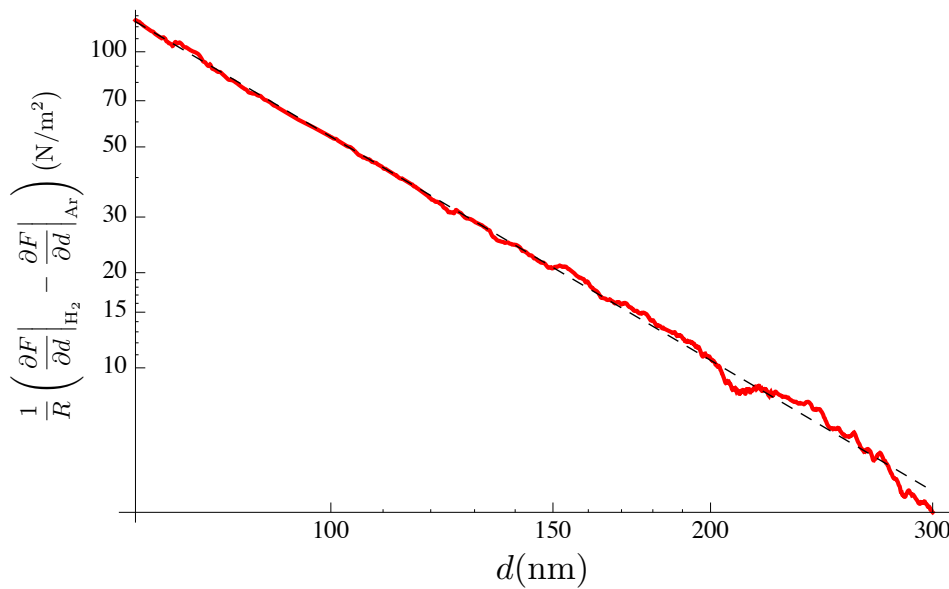


Figure 4.10: Difference between the force gradients measured in Ar and Ar/H₂ as a function of distance on a double logarithmic scale (red line). The black dashed line indicates a power law with exponent -2.35 .

We also checked in a different experimental setup whether our mirror alters

its dielectric properties upon exposure to 40 mbar partial pressure of H₂, and observed that this is not the case. Therefore, the Casimir interaction, although smaller compared to what expected from theory, should be equal in all cases (the Casimir force does not depend significantly on the dielectric properties of an intervening gas). This means that we can analyze the difference between the Ar/H₂ and pure Ar force gradient data of Fig. 4.9, and assume that this difference has no Casimir contribution in it. In Fig. 4.10, we plot the difference between the averaged force gradients in Ar/H₂ and pure Ar as a function of distance on a double logarithmic scale (red continuous line). The dashed black line indicates a power law with exponent -2.35 . It is evident that our force gradient difference follows this power law pretty strictly in the plotted distance range. This exponent would indicate a force between the sphere and the plate that scales like $d^{-1.35}$. Such a weak dependence on separation might indicate that the observed extra force is of electrostatic origin.

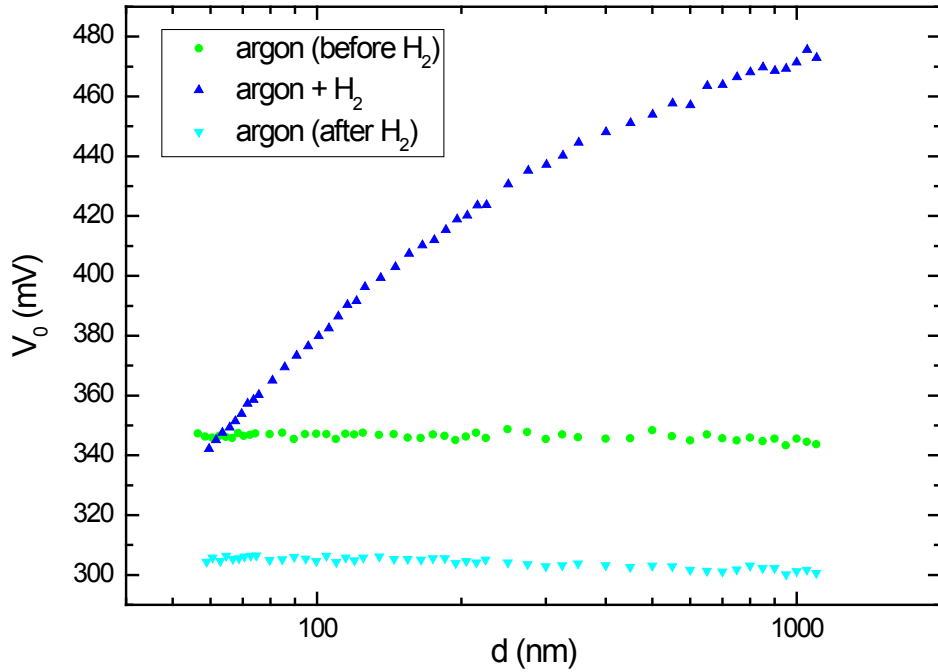


Figure 4.11: Measured contact potential difference as a function of separation on a semi-logarithmic plot. Green circles and cyan downward triangles are measurements in pure argon atmosphere before and after exposure to hydrogen, respectively. The blue upward pointing triangles represent the contact potential data acquired in the 4% H₂ in Ar mixture.

In fact, we have more clues pointing towards an extra electrostatic interaction caused by the presence of the H₂ molecules. In our setup, we continuously measure the contact potential difference between our surfaces. In our experiments, this contact potential is defined by the amount of counter bias voltage

one has to apply to have minimum electrostatic force between the sphere and the plate. It has recently been shown in several papers [19, 38, 39, 58] that this contact potential can depend on the separation between the surfaces. In Fig. 4.11, we plot the measured V_0 data as a function of separation on a semi-logarithmic scale. The green circles represent data obtained before the setup was purged with hydrogen gas. The blue upward pointing triangles were gathered in the argon/hydrogen mixture. After purging with pure Ar again and waiting 3 days to equilibrate the system, we recorded the data represented by the cyan downward pointing triangles. It is clear that the dependence of V_0 on separation for the data sets gathered in pure Ar atmosphere is rather small; they differ in absolute value, but this is mostly a time-related drift, as discussed in [39]. The data obtained for the argon/hydrogen mixture, on the contrary, strongly depend on separation. This effect is reproduced in all the measurement runs performed in this 4% H_2 in Ar mixture. Because this strong dependence of V_0 is an indication of an unknown electrostatic effect, we suggest that the strong force gradient we presented in Fig. 4.9 is of electrostatic origin. Further investigations need to be conducted to fully understand this phenomenon.

After our force measurement between the juxtaposed Y/Pd switchable mirror and the gold-coated sphere, we also performed measurements between the same sphere and a gold mirror. These experiments revealed the same behavior, i.e. strong dependence of V_0 on d and a strong force gradient in hydrogen. Furthermore, also in this case, the force gradient in air and argon was significantly lower than the force gradient expected from theory (and thus also than the one presented in chapter 3, because those agreed with theoretical predictions). We suppose that the gold coating on the sphere was somehow damaged by the exposure to hydrogen gas, perhaps due to the Ti adhesion layer that can absorb hydrogen. Therefore, we do not know whether the results presented in this chapter are a curiosity caused by some specific metal surfaces composition on our sphere, or that they are generic. We therefore strongly suggest to carry out new measurements between fresh gold coated spheres and a gold planar sample in Argon and Argon/hydrogen mixtures^{||}.

Acknowledgment

We would like to thank J. H. Rector for taking care of the gas upgrade of the system.

^{||}It would be better to use Cr instead of Ti as an adhesion layer, since Cr does not absorb hydrogen.

4.4 Hydrodynamic force measurements in various gases

Abstract – In this section we present hydrodynamic force measurements conducted between a sphere and a plate at separations between 100 nm and 10 μm . The hydrodynamic force data are acquired together with electrostatic force calibration data, ensuring a properly calibrated force setup. We have gathered measurements in He, air, Ar, and SF₆ atmosphere, and analyzed the data using a continuous medium model that takes into account fluid slip across the interfaces. The obtained slip lengths vary between 38 ± 1 nm for SF₆ and 387 ± 9 nm for He. Interestingly, the model and the data overlap even for data obtained at short separation in He, where the separation between the surfaces is smaller than the mean free path of the He molecules.

In chapter 3 and the previous section we have seen that our Casimir force setup is capable of performing precise measurements of the hydrodynamic interaction between the sphere and the plate. This interaction arises because of the moving gas that flows in and out of the sphere-plate gap due to the plate oscillation at ω_2 . For low enough oscillation frequencies this effect is purely dissipative and thus out-of-phase with the other force signals. In fact, according to [68], the in-phase elastic component is small as long as $\sigma_{sphere} = \frac{4\eta\omega_2 R}{pd} < 1$, where η is the viscosity of the intervening gas, R is the radius of the sphere, p is the gas pressure, and d is the separation between the sphere and plate surfaces. In our experiments, $\sigma_{sphere} \leq 10^{-3}$, and we therefore neglect the elastic component of the hydrodynamic interaction.

When we assume that the boundary conditions for the gas flow at the solid-gas interface are the usual no-slip boundary conditions that are typically valid in the macroscopic regime, the damping force acting on the sphere would be

$$F_{H,\text{no-slip}} = -\frac{6\pi\eta v R^2}{d}, \quad (4.11)$$

where v is the relative velocity between the sphere and the plate. This equation has the peculiar property that the damping force diverges rapidly for $d \rightarrow 0$. This means that a sphere dropping towards a plate in a fluid (albeit a gas or a liquid) would never reach the plate in a finite amount of time [42]. It turns out that, for small distance d , Eq. 4.11 needs to be modified to include the effects of fluid slip at the solid-gas interface.

For low fluid speeds, we assume that the flow is laminar and that thus the fluid velocity increases linearly with the distance from the interface. We introduce fluid slip by letting this velocity profile extend into the solid surface for a length b (the so-called slip length). This idea is schematically represented in Fig. 4.12, where v_b is the bulk fluid velocity (which varies with distance to the surface z) and v_s is the fluid velocity at the interface. Therefore

$$v_s = b \frac{\partial v_b}{\partial z} \quad (4.12)$$

which defines b . From these boundary conditions, Hocking derived in 1972 the full form of the hydrodynamic damping force between a sphere and a plate [42]:

$$F_H = -\frac{6\pi\eta v R^2}{d} f^* \quad (4.13)$$

with

$$f^* = \frac{d}{3b} \left[\left(1 + \frac{d}{6b} \right) \ln \left(1 + \frac{6b}{d} \right) - 1 \right]. \quad (4.14)$$

The main result of his work was, according to Hocking, the fact that his equation permits contact between the sphere and the plate in a finite amount

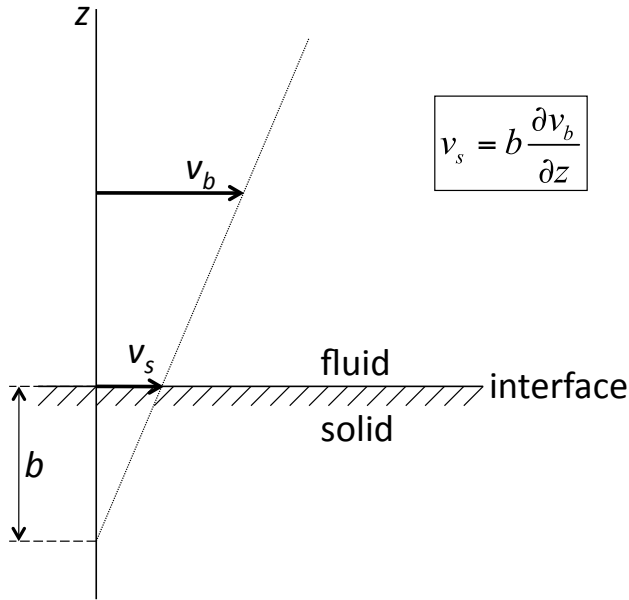


Figure 4.12: Schematic representation of the fluid flow boundary conditions used to derive Eqs. 4.13 and 4.14.

of time. Therefore, it was now possible to calculate correctly the coalescence of droplets without having to make the arbitrary assumption that collision occurs whenever the gap between the surfaces becomes less than some arbitrarily chosen small length, like it was done before [42]. With our Casimir force setup we can use his equation and check how well it describes the hydrodynamic force data and extract the slip lengths for different gases.

We have performed measurements of the hydrodynamic force between a 100 μm radius gold-coated sphere and a gold-coated polished sapphire slide. We have calibrated the force sensitivity and the separation between the surfaces with the electrostatic force, as described in chapter 2. The position of the plate is oscillated at 119 Hz with an amplitude of roughly 9 nm. The separation between the surfaces is decreased in discrete steps from 10 μm until 100 nm using the feedback-controlled piezoelectric actuator. The lock-in integration time is 300 ms and the waiting time at every position is 2.4 s. The mechanical drift within one measurement run is less than 1 nm. The hydrodynamic force measurements are conducted simultaneously with the electrostatic calibration, ensuring correct calibration of the data. We have conducted measurements in 1 bar of He, air, Ar, and SF₆ atmosphere.

In Fig. 4.13 we present the hydrodynamic forces we measured as a function of sphere plate separation in the four different gases. The green circles represent data in pure He, the upward pointing blue triangles in air, the downward pointing cyan triangles in Ar, and the red squares indicate data obtained in

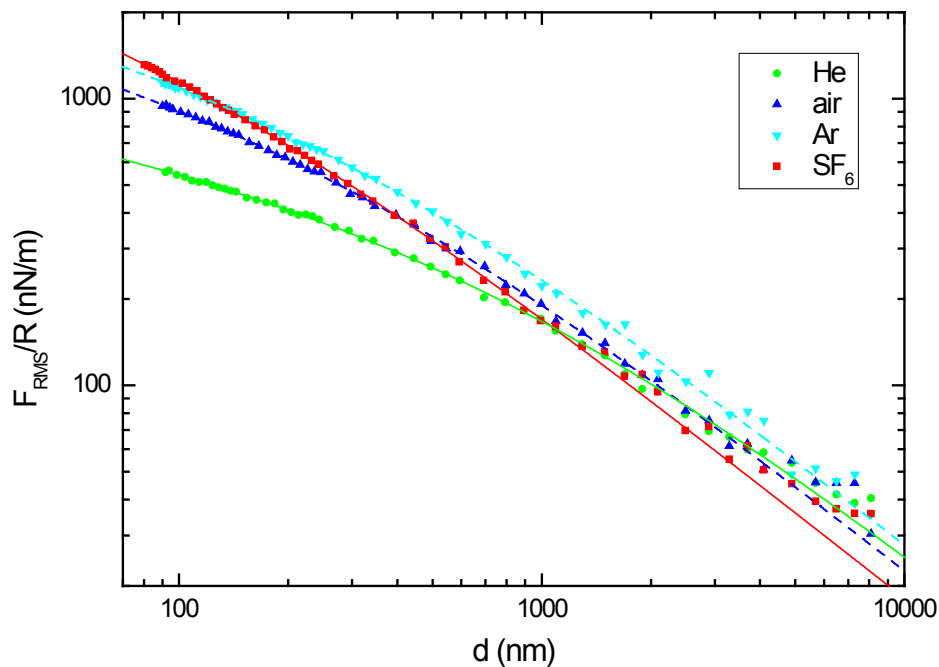


Figure 4.13: Double logarithmic plot of the hydrodynamic force divided by the sphere radius R as a function of separation between the sphere and plate surfaces. The green circles represent data in pure He, the upward pointing blue triangles in air, the downward pointing cyan triangles in Ar, and the red squares in SF₆ gas. The lines indicate the best fits to the data with the Hocking model [42] (Eqs. 4.13 and 4.14). Obtained slip lengths are 387 ± 9 nm in He, 124 ± 3 nm in air, 118 ± 3 nm in Ar, and 38 ± 1 nm in SF₆.

SF_6 gas. The forces are presented divided by the sphere radius, a consequence of our electrostatic calibration procedure. The continuous lines are the best fits to the data with Eqs. 4.13 and 4.14 with two fit parameters b and ηR . The model fits the data well, except at large separation. We suspect that the hydrodynamic interaction between the cantilever and the plate becomes relevant in this region, and this effect is not taken into account in the model. Therefore, we measure too much force at large separation.

Let us first discuss the fit parameter ηR . Since we have not measured the sphere radius, we are unable to get the viscosity directly from our data. This restriction is caused by the fact that the electrostatic force scales linearly in R while the hydrodynamic force scales like R^2 . Therefore, we can only compare the values of ηR among the four different experiments (R is the same for all experiments though). If we take the viscosity of air as a reference, we find $\eta_{\text{He}} = 1.15\eta_{\text{air}}$, $\eta_{\text{Ar}} = 1.2\eta_{\text{air}}$, and $\eta_{\text{SF}_6} = 0.78\eta_{\text{air}}$. From the literature, we see that $\eta_{\text{He}} = 1.06\eta_{\text{air}}$, $\eta_{\text{Ar}} = 1.17\eta_{\text{air}}$, and $\eta_{\text{SF}_6} = 0.79\eta_{\text{air}}$, a sufficiently close match, although the viscosity of He that we measure is significantly higher than what found in the literature.

The fitted slip lengths b that we have obtained with these measurements are 387 ± 9 nm in He, 124 ± 3 nm in air, 118 ± 3 nm in Ar, and 38 ± 1 nm in SF_6 . We have thus studied around one order of magnitude variation in gaseous slip lengths. It is known that the slip length scales with the mean free path of the gas molecules. It is therefore not surprising to find that a very light molecule as He slips strongly over the gold surface, whereas a heavy and big molecule like SF_6 does not slip very much. Furthermore, it is interesting to observe that in the case of He, the probed separation range extends well into the regime where the separation is smaller than the mean-free path of the molecules. Still, especially at these short distances, the continuous medium theory developed by Hocking seems to describe the data rather well. It is quite surprising to find out that the continuous medium description works well for distances smaller than the mean free path of the gas molecules.

Chapter 5

Fiber-top and Ferrule-top Casimir force measurements

5.1 Introduction

At the beginning of the development of our Casimir force setup, we were having a severe technical problem with the cantilever deflection detection system of the AFM. In fact, the laser light that hits the cantilever is not completely reflected into the quadrant photodetector by the cantilever, and part of the light reaches the sample beneath. This light is then reflected from the sample and also impinges on the photodetector, resulting in a spurious signal that depends on the separation between the cantilever and the sample. This signal contains multiple components, including a mostly linear background signal and oscillating interference signals. Since we wanted to measure forces as a function of separation, this spurious signal was problematic. It was then that we invented the fiber-top cantilever [45].

A fiber-top cantilever is a silica cantilever carved out from the cleaved end of an optical fiber and thus monolithically anchored to the fiber itself. Typically, one uses a Focused Ion Beam machine to mill a cantilever from the end facet of a single mode optical fiber (125 μm diameter with the jacket stripped off) such that it is positioned directly above the fiber core. Therefore, the light-guiding property of the optical fiber can be used to measure the actual position and movements of the cantilever. When one shines light through the fiber, the light is reflected from the fiber-to-air interface and then from the air-to-cantilever interface, where the latter is also reflected back into the fiber core. Both signals interfere and the intensity of the backwards traveling light signal is a precise measure of the cantilever position. Such an interferometric technique can determine the cantilever deflection with sub-nm precision and with high bandwidth. In this chapter, we report on our attempts to perform Casimir force measurements with such a sensor.

In section 5.2 we present our efforts to detect the Casimir force with a modified fiber-top sensor. To achieve high force sensitivity, we have altered the design of the cantilever and fabricated a torsional device, resulting in a much

lower spring constant than a conventional fiber-top cantilever. We present measurements of the force sensitivity of this device and show that the the sensor should be capable of providing precise measurements of the Casimir force. Unfortunately, we were unable to measure the force with this device due to too strong hydrodynamic interactions caused by the close proximity of the fiber edge to the sample. Two possible workarounds would be either to move the setup into vacuum or to increase the size of the cantilever-to-fiber gap in a new design.

Following the second route, we now fabricated a normal cantilever out of a ferruled optical fiber. The resulting cantilever is 3.4 mm long, 200 μm wide and 40 μm thick, and the cantilever-to-ferrule gap is roughly 100 μm (compared to only 3 μm for the fiber-top torsional force sensor). In section 5.3, we present the Casimir force measurements we obtained with such a ferrule-top cantilever, and show that we can precisely measure the Casimir force with this all-optical sensor. This expedient thus paves the way for Casimir force measurements in critical environments, where the standard Casimir force setups would be unable to operate.

In section 5.4, we present a new interferometric scheme to detect displacements with high resolution. In conventional homodyne interferometers, the output signal is a sinusoidal function of distance, and the displacement sensitivity strongly depends on the actual position in the interference fringe. One therefore often operates these devices in the so-called quadrature point, where the distance dependence of the signal is maximum. By slightly modulating the position of the fiber or the end-mirror (couple of nm), one can generate a new signal that is orthogonal to the conventional signal. By combining both signal one obtains a precise measurement of the distance that does not have the limitation of only being able to provide good data at the quadrature position. This technique is therefore extremely useful for the calibration of piezo-electric stages, that typically travel over several interference fringes. In this section, we present in detail this technique and show interferometric displacement measurements that demonstrate the method.

5.2 Casimir force experiments in air: Two birds with one stone

Abstract – We briefly discuss a new force sensor based on fiber optics that adapts well to Casimir force measurements in critical environments. We show that the new sensor is sensitive enough for the detection of Casimir forces, but that its performance is presently hampered by hydrodynamic interactions caused by the presence of air.

This section is a part of the paper: S. de Man, K. Heeck, K. Smith, R. J. Wijngaarden, and D. Iannuzzi, *Int. J. Mod. Phys. A* **25**, 2231 (2010)

5.2.1 Fiber-top Casimir force setup

The investigation of the dependence of the Casimir force on the boundary conditions is currently pushing experimentalists to rely on instruments that can measure surface forces under extreme conditions, such as low temperatures, conductive liquids, et cetera. Adapting existing setups to those situations is often not an option, and new technologies have to be developed to extend the experimental studies beyond standard environments.

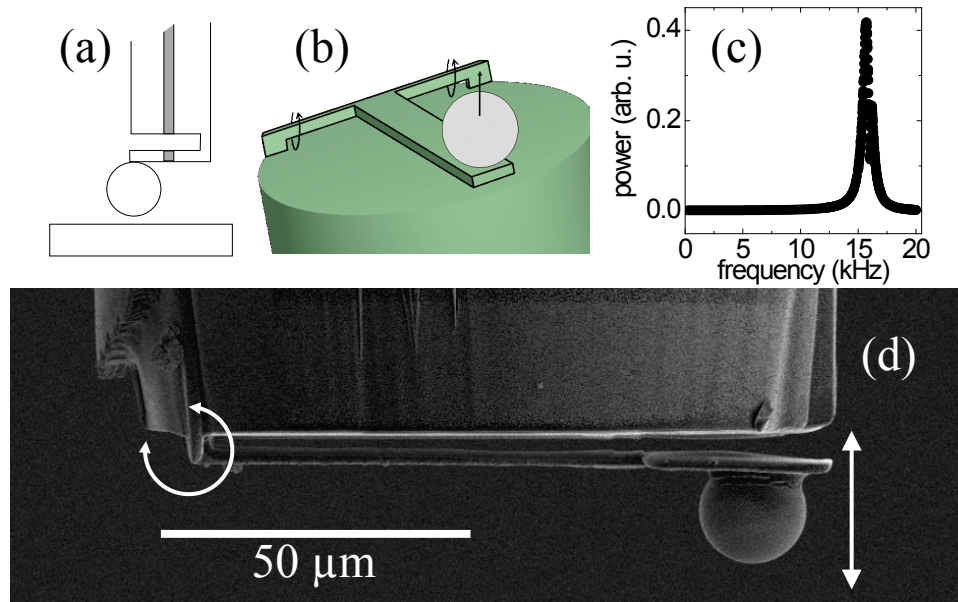


Figure 5.1: a) Drawing of a fiber-top based Casimir force setup. A sphere is attached to the free end of a fiber-top cantilever. The deflection of the cantilever is measured by coupling light in the fiber. b) Schematic drawing of a torsional fiber-top device. Instead of a normal cantilever, the torsional device is anchored to the fiber with two thin rods that can rotate around their central axes in response to external forces. c) Power spectrum of a fiber-top torsional device, as measured by driving the cantilever with an electrostatic force. d) Scanning electron microscope image of a fiber-top torsional device equipped with a sphere for performing force measurements. The pivot point of the cantilever is at the left of the figure.

In 2005, our group has introduced a new all-optical device that represents an interesting platform for the implementation of Casimir force setups in critical environments: the fiber-top cantilever [45]. Fiber-top cantilevers are obtained by carving a thin mechanical beam out of the cleaved end of a single mode optical fiber. The light coupled from the opposite end can then be used to detect tiny deflections of the cantilever, and, thus, tiny forces applied to the cantilever's free hanging end^{citeIannuzzi:2006p97,RUGAR:1989p11}. This

force sensor has no electronic contacts on the sensing head and is entirely fabricated on top of a 125 μm diameter optical fiber. It thus easily fits in small volumes (a good option, for example, for cryogenic temperatures) and still works properly in conductive liquids (where force sensors with electronic read-outs would fail). It is thus reasonable to envision that a fiber-top cantilever equipped with a sphere on its free hanging end could perform well as the force sensor in a Casimir force setup (see Fig. 5.1a).

It is however important to note that, even with the carving resolution of the most sophisticated tools currently available (i.e., Focused Ion Beam milling), it is not possible to fabricate fiber-top cantilevers with dimensions small enough to achieve spring constants smaller than 1 N/m, as required in Casimir force experiments. To solve this problem, we decided to fabricate a slightly different fiber-top device, where the cantilever is suspended over the fiber via two torsional beams, as reported in Fig. 5.1b. In Fig. 5.1d, we report an Scanning Electron Microscope (SEM) image of a fiber-top torsional force sensor equipped with a 18 μm diameter sphere on its free hanging end.

In Fig. 5.1c, we plot the power spectrum of the torsional device. This power spectrum is acquired by applying an oscillating electrostatic force to the sphere and recording the amplitude of the resulting cantilever motion with a lock-in amplifier. It is clear that the force sensor has a resonance frequency of roughly 16 kHz. Because we measured the dimensions of the cantilever and the diameter of the sphere with the SEM, we can calculate the mass of the cantilever (30 nanograms) using the density of the fiber material (2200 kg/m³). With the parallel axis theorem, we then obtain the total moment of inertia of the cantilever sphere combination around the axis that goes through the torsional beams ($1.6 \cdot 10^{-19}$ kg m²). Combining the latter with the measurement of the resonance frequency, we arrive at a torsional spring constant of $1.6 \cdot 10^{-9}$ Nm/rad and a spring constant of 0.2 N/m.

To assess the sensitivity of our device, we have applied an oscillating voltage between the sphere and a nearby metallic plate (as in Fig. 5.1a) at a frequency $\frac{\omega_1}{2\pi} = 72.2$ Hz. A digital lock-in amplifier equipped with a 24dB roll-off low-pass filter is used to measure the uncertainty in the resulting cantilever oscillation at $2\omega_1$ (144.4 Hz). The result is an RMS noise of 1.2 pm/ $\sqrt{\text{Hz}}$, which indicates that the AC force resolution of our setup is roughly 240 fN/ $\sqrt{\text{Hz}}$. Such a force resolution is more than sufficient for a high precision measurement of the Casimir force.

According to our preliminary results obtained using this device and the method described in the previous section, it appears evident that, as soon as the plate in front of the sphere is set into oscillation, the hydrodynamic interaction between the mechanical beam and the fiber is not negligible and actually hampers the efficiency of the experimental technique. To solve this problem, we are planning to move to larger fiber-top devices (namely, ferrule-top cantilever [50, 88]), where the gap between the force sensor and the fiber is

much larger ($\simeq 50 \mu\text{m}$). Studies are under way to understand the potentiality of this new instrument. For Casimir force measurements in vacuum, though, the system presented here should work fine.

5.3 Measurement of the Casimir force with a ferrule-top sensor

Abstract – We present a Casimir force setup based on an all-optical ferrule-top sensor. We demonstrate that the instrument can be used to measure the gradient of the Casimir force between a gold coated sphere and a gold coated plate with results that are comparable to those achieved by similar atomic force microscope experiments. Thanks to the monolithic design of the force sensor (which does not require any optical triangulation readout) and to the absence of electronics on the sensing head, the instrument represents a significant step ahead for future studies of the Casimir effect under engineered conditions, where the intervening medium or the environmental conditions might be unsuitable for the use of more standard setups.

5.3.1 Introduction

Long range surface interactions are of paramount importance in the design of Micro- and NanoElectroMechanical Systems (MEMS and NEMS), as they determine the minimum separation that two miniaturized mechanical pieces can reach before they snap to contact. It is thus not surprising that, over the last decade, an ever increasing number of groups has been drawing the attention of the scientific community to the potential relevance of the Casimir effect in nanotechnology [5, 18] and on what currently goes under the name of *quantum fluctuations engineering* – the possibility of tailoring the Casimir force with a suitable choice of the shape and material properties of the interacting objects and of the medium between them [14, 20, 32, 33, 37, 60, 89, 90]*. Driven by this trend, scientists have developed a wide variety of instruments that can assess different aspects of this interaction mechanism. Macroscopic setups [26, 28, 29, 52] and micromachined torsional balances [2, 3, 30] are typically optimized for utilization in vacuum or air, but would hardly work in liquids. Experiments in vacuum can be as well performed by means of custom made atomic force microscopes (AFMs) [35, 36], which, after proper modifications, can be also used to measure the Casimir force in gaseous environments [20] or in liquids [14]. Because AFMs rely on optical triangulation, however, it is difficult to imagine a universal measuring head that can easily adapt to different environments, ranging, for example, from low temperature vacuum to room temperature liquids.

Earlier this year, our group proposed to overcome this issue by replacing the AFM head with an all-optical micromachined torsional force sensor that adapts well to both vacuum and critical environments [91]. The sensor is based on fiber-top technology [45]. It consists of a mechanical rectangular beam carved out of the cleaved end of a standard single mode optical fiber. The beam is suspended a few microns above the rest of the fiber by means of two lateral torsional rods. The light coupled from the opposite end of the fiber allows one to measure the tilting angle of the rectangular beam and, therefore, the force that makes it tilt. Thanks to its monolithic design and to the absence of electronics on the sensing element, this micro-opto-mechanical balance can be in principle used in any environment without any change of the readout mechanics, optics, or electronics. Unfortunately, however, preliminary experiments show that, as soon as measurements are not carried out in vacuum, the sensor can only be used in static mode [91]. Dynamic modes, which are typically more sensitive, are in fact disturbed by spurious effects induced

*Over the last 30 years, there has been a much more extensive activity focused on the investigation of the van der Waals interaction in the non-retarded limit, with particular emphasis to liquid environments, and there are important examples in which the investigation has been extended to the retarded part of the interaction. A complete review of that part of the literature is out of the scope of this paper. We refer the reader to [15, 41] for more details.

by the hydrodynamic force between the mechanical beam and the fiber below (a phenomenon that goes under the name of *squeezed field air damping* [92]). Furthermore, because the optical fiber is only $125\text{ }\mu\text{m}$ in diameter, fiber-top devices are typically fabricated with an expensive and time consuming technique (namely, Focused Ion Beam (FIB) milling [93]). Fiber-top technology cannot thus be considered as a practical solution for systematic measurements, where, due to recurrent accidental damaging of the force sensor, one must rely on probes that can be easily replaced.

To overcome the fabrication issue of fiber-top devices, we recently introduced a novel approach that preserves the flexibility of fiber-top technology while reducing manufacturing costs and production time: the ferrule-top cantilever [50]. To fabricate a ferrule-top cantilever, a standard single mode optical fiber is glued inside the bore hole of a much bigger pierced ferrule. The fiber and the ferrule are so well held together by the glue that they behave like a single mechanical piece. The ferruled fiber is thus equivalent to a very large single mode optical fiber that can now be milled in the form of a cantilever by means of more convenient techniques (e.g., laser ablation). Interestingly, because of the larger dimensions of the building block, the gap between the cantilever and the remaining part of the ferrule is typically much larger than in fiber-top devices. Ferrule-top cantilevers are thus supposed to suffer considerably less from the hydrodynamic problems than fiber-top sensors.

In this paper we present a ferrule-top force setup designed to measure the Casimir attraction between a sphere and a flat plate, and we demonstrate that one can indeed perform precise measurements of the Casimir force between a sphere and a plate kept in air with a dynamic detection scheme that does not induce any spurious effects.

5.3.2 Experimental setup

The experimental setup presented in this paper is designed to measure the Casimir force between a $200\text{ }\mu\text{m}$ diameter sphere and a plate as a function of separation in a distance range between, approximately, 50 nm and 200 nm.

The force sensor is realized according to the scheme sketched in Fig. 5.2. A pierced $2.5\text{ mm} \times 2.5\text{ mm} \times 7\text{ mm}$ rectangular ferrule, made out of borosilicate glass, is initially carved by means of laser ablation in the form of a cantilever that stretches over one of the diagonals of the edge of the ferrule. At the end of the milling process, a small amount of transparent epoxy is dropped and cured inside the $127\text{ }\mu\text{m}$ diameter hole left open at the center of the cantilever, while a standard single mode optical fiber is slid into the hole of the ferrule from the other side and glued with the cleaved end at approximately $100\text{ }\mu\text{m}$ from the bottom surface of the cantilever. A $200\text{ }\mu\text{m}$ diameter sphere is then attached to the top of the free hanging end of the sensor by means of a small droplet of UV curable epoxy. The sensor and the sphere are finally coated

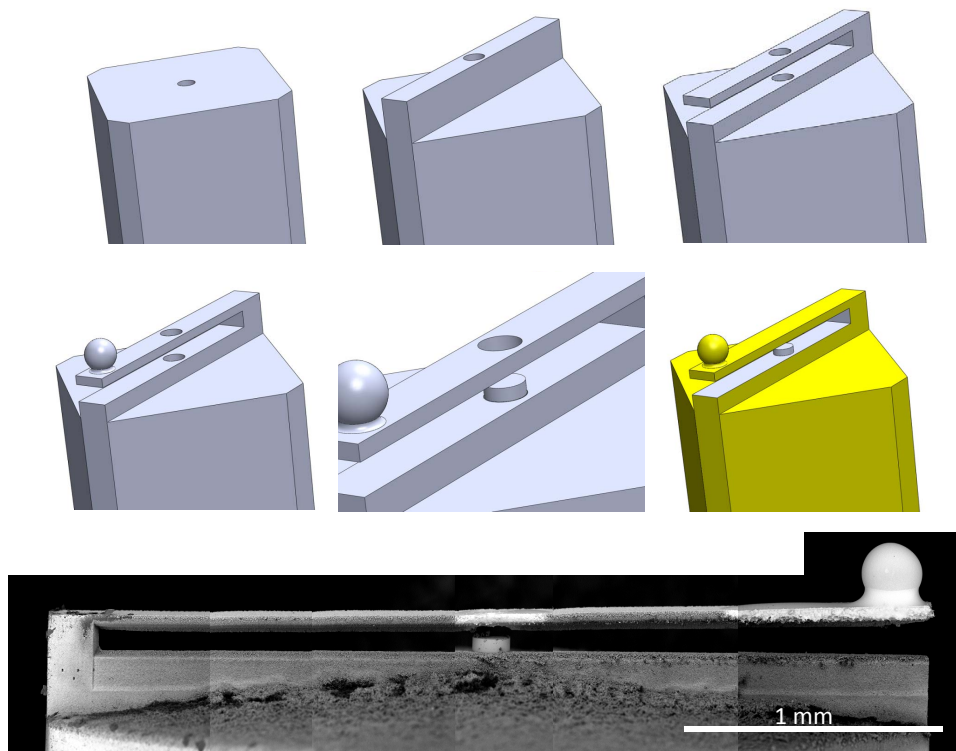


Figure 5.2: Fabrication steps followed to manufacture a ferrule-top cantilever for Casimir force measurements. The building block is a pierced $2.5\text{ mm} \times 2.5\text{ mm} \times 7\text{ mm}$ rectangular ferrule made out of borosilicate glass. The ferrule is machined in the form of a rectangular cantilever, which is then equipped with a spherical bead. An optical fiber slid through the central hole and glued to the ferrule allows detection of cantilever deflections by means of interferometric techniques. The bottom figure is a composition of six scanning electron microscope images showing the device used in the experiment described in the paper.

with a 5 nm thick Cr adhesion layer followed by a 200 nm thick Au film.

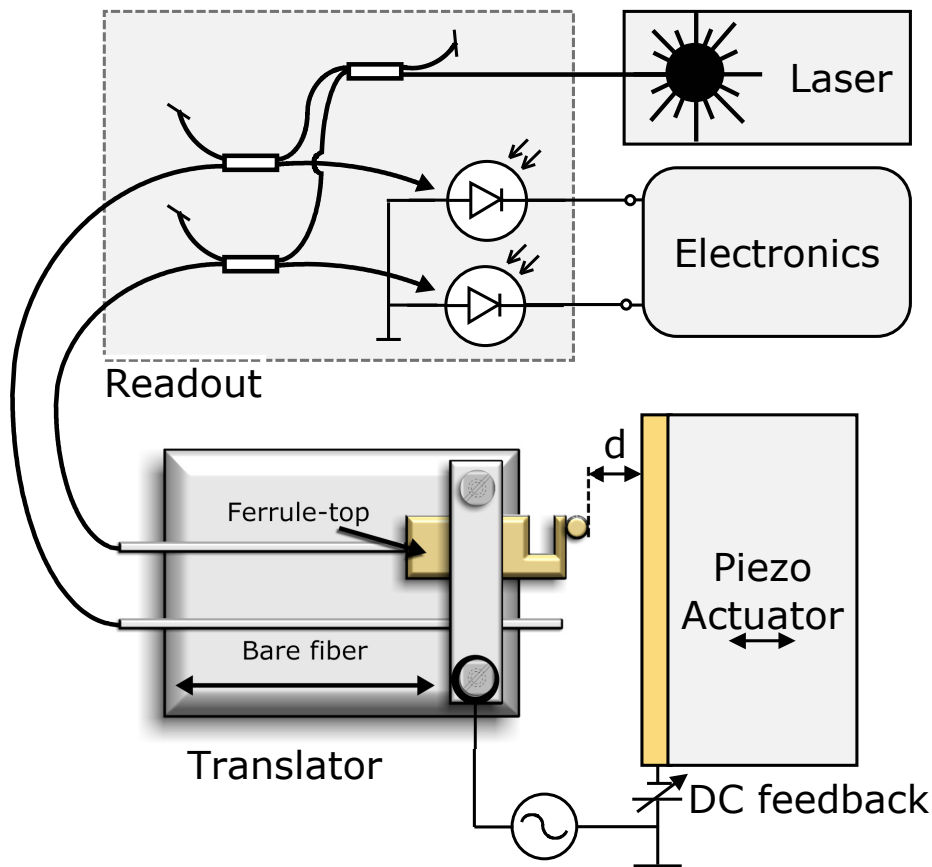


Figure 5.3: Sketch of the experimental setup used to measure the Casimir force between a plate and a sphere attached to a ferrule-top cantilever. The ferrule-top cantilever is anchored to a translational stage that allows one to coarsely move the sensor with the sphere close to the plate. The plate is attached to a piezoelectric stage for fine tuning of the separation between the two interacting surfaces. A bare fiber is anchored parallel to the force sensor and is used to measure movements of the piezoelectric actuator via interferometric techniques. An electronic circuit supplies an AC voltage between the sphere and the plate, which allows one to compensate for the residual electrostatic force and calibrate the force sensor. The setup is mounted on an aluminum block kept at fixed temperature inside an anechoic box and isolated from the surroundings with passive vibration dampers (not shown).

The ferrule-top device is anchored on top of a manual translation stage, just in front of a gold coated sapphire plate that is attached to a piezoelectric stage (see Fig. 5.3). The manual manipulator allows a first coarse approach of the sensor towards the plate, while the piezoelectric stage is used for the actual scanning during the force-vs-distance measurements. The translational stage also hosts a bare cleaved optical fiber, parallel to the ferrule-top sensor, that is used to measure movements of the piezoelectric stage. The setup is fixed to a

block of aluminum that is kept at fixed temperature by means of four resistors controlled via a feedback circuit. To reduce acoustic and seismic coupling to the environment, the whole instrument is mounted on a silicone pad inside an anechoic chamber on top of a marble table equipped with passive vibration damping blocks.

To simultaneously measure the deflection of the ferrule-top cantilever and the motion of the piezoelectric stage, we built two fiber optic interferometers that are fed with the same laser source (Thorlabs Pro800 chassis with a WDM tunable laser module (1552.48 nm to 1554.18 nm)) (see Fig. 5.3). The laser light is split by a 50/50 optical fiber coupler into two forward branches. In both forward branches, the light is then split again by 90/10 couplers and sent towards the ferrule-top cantilever and the bare cleaved fiber. For the ferrule-top sensor, the light is reflected by the fiber-to-air, air-to-glue, and glue-to-gold interfaces. The amount of light traveling backwards into the fiber is given by

$$W(d_{gap}) = W_0 \left[1 + V \cos \left(\frac{4\pi d_{gap}}{\lambda} + \phi_0 \right) \right] \quad (5.1)$$

where d_{gap} is the distance between the fiber end and the cantilever, W_0 is the mid-point interference signal, V is the fringe visibility, λ is the laser wavelength, and ϕ_0 is a phase shift that only depends on the geometry of the cantilever [50]. This reflected light travels back into the fiber and is split again by the coupler, which sends part of the signal onto a photodetector (Thorlabs PDA10CS). Reading the current generated on the photodetector, which is proportional to $W(d_{gap})$, one can measure changes in d_{gap} (see eq. 5.1) and, thus, the external forces that have produced those changes. The other branch of the double interferometer works identically to the ferrule-top branch, except that the reflected signal is composed of the reflections from the fiber-to-air interface and from the gold mirror, allowing one to measure the relative position of the piezoelectric stage.

From Eq. 5.1 it is clear that it is convenient to operate the force sensor in its quadrature point, where the readout is most sensitive and linear in deflection [94]. For this reason, before each experiment, we first coarsely bring d_{gap} close to quadrature by adjusting the temperature set-point of the setup, which induces differential thermal expansions on the different parts of the ferrule-top device. We then use the tunable laser wavelength to precisely tune λ to the quadrature point[†].

Casimir force measurements are performed following a method similar to that described in [19, 20], which allows one to simultaneously calibrate the instrument, counterbias the electrostatic potential difference that exists between the sphere and the plate, and measure the gradient of the Casimir force as a function of separation.

[†]The 1.7 nm wavelength variation spanned by our laser source alone is not always sufficient to adapt the laser wavelength to the actual length of the fiber-to-cantilever gap.

In a nutshell, while slowly changing the separation between the sphere and the plate by means of the piezoelectric stage, we supply an AC voltage to the sphere with frequency ω_1 much smaller than the resonance frequency of the force sensor. This AC voltage gives rise to an electrostatic force that makes the cantilever oscillate. The mechanical oscillation has one component at ω_1 and one component at $2\omega_1$. The ω_1 component drives a negative feedback loop that compensates for the contact potential difference that exists between the sphere and the plate, while the $2\omega_1$ component allows one to calibrate the instrument and to measure the separation between the interacting surfaces. On top of the electrostatic force modulation, we add a small oscillatory motion to the piezoelectric stage at a frequency ω_2 that lies somewhere between ω_1 and $2\omega_1$. From the in-phase motion of the cantilever at ω_2 , we can finally measure the gradient of the force between the sphere and the plate.

For the details of the experimental method, we refer the reader to [19, 20]. It is however important to stress that, contrary to the piezoelectric stage of the setup presented in [19, 20], the one used in this experiment is driven via an open loop circuit and is not equipped with any internal calibration sensor. For this reason, we have implemented a slightly different method to determine the separation between the two surfaces. To explain this new approach, we first note that the electrostatic force generated by the AC voltage is equal to:

$$\frac{F_e}{R} = \frac{\varepsilon_0 \pi (V_{AC} \cos(\omega_1 t) + V_0)^2}{d} \quad (5.2)$$

where ε_0 is the permittivity of air, R is the radius of the sphere, and V_0 is the residual potential difference. Therefore, the mechanical oscillation induced by the electrostatic force on the force sensor at $2\omega_1$ gives rise to a $2\omega_1$ signal on the photodiode of the interferometer that scales like $S_{2\omega_1} \propto V_{AC}^2/d$. The proportionality constant can be measured by looking at the output signal of the bare fiber interferometer. We know in fact that, when the bare fiber interferometer signal has moved through exactly one interference fringe, the plate has moved for exactly $\lambda/2$. Once the proportionality constant β is known, one can extract d from $d = \beta \cdot V_{AC}^2/S_{2\omega_1}$.

5.3.3 Results and discussion

The sensor used for the data presented below was a 3.4 mm long, 200 μm wide, 40 μm thick ferrule-top cantilever (resulting in an expected spring constant of $\approx 2 \text{ N/m}$) with $\approx 100 \mu\text{m}$ ferrule-to-cantilever gap (see the scanning electron microscope image of Fig. 5.2). The resonance frequency was measured independently, and resulted to be equal to 2.7 kHz, with a Q factor of 42.

In Fig. 5.4 and Fig. 5.5 we show the results of a typical measurement run. Data were gathered during 10 consecutive back-and-forth scans. Each scan had a duration of 1000 s and a stroke of 1 μm spanned by applying a driving

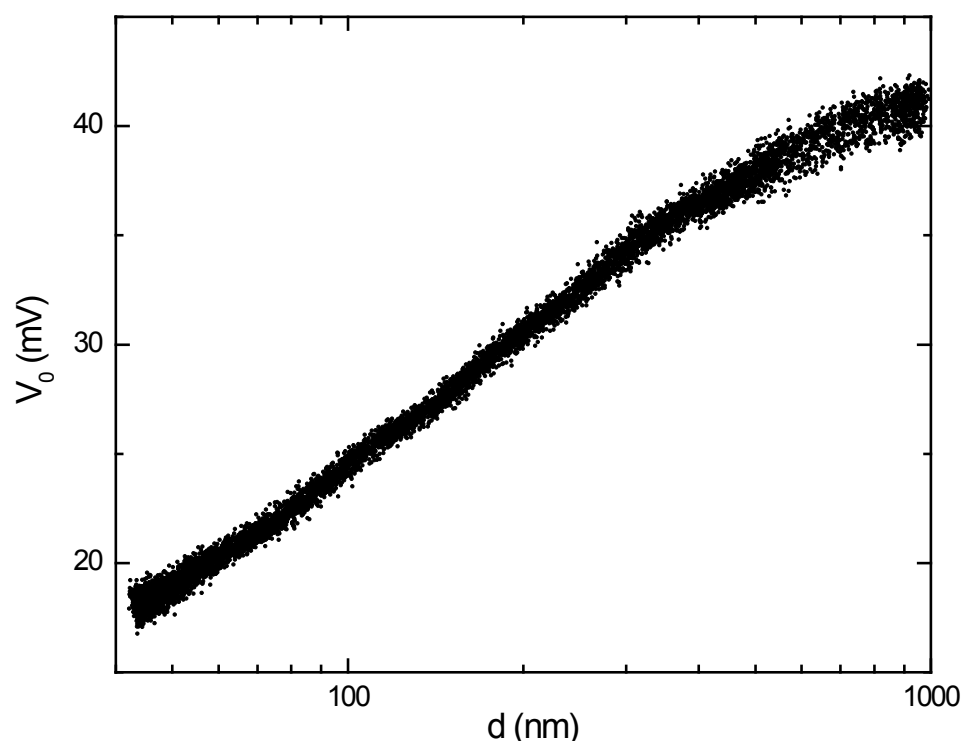


Figure 5.4: Measurement of the residual potential between the interacting surfaces as a function of separation as obtained during 10 consecutive scans.

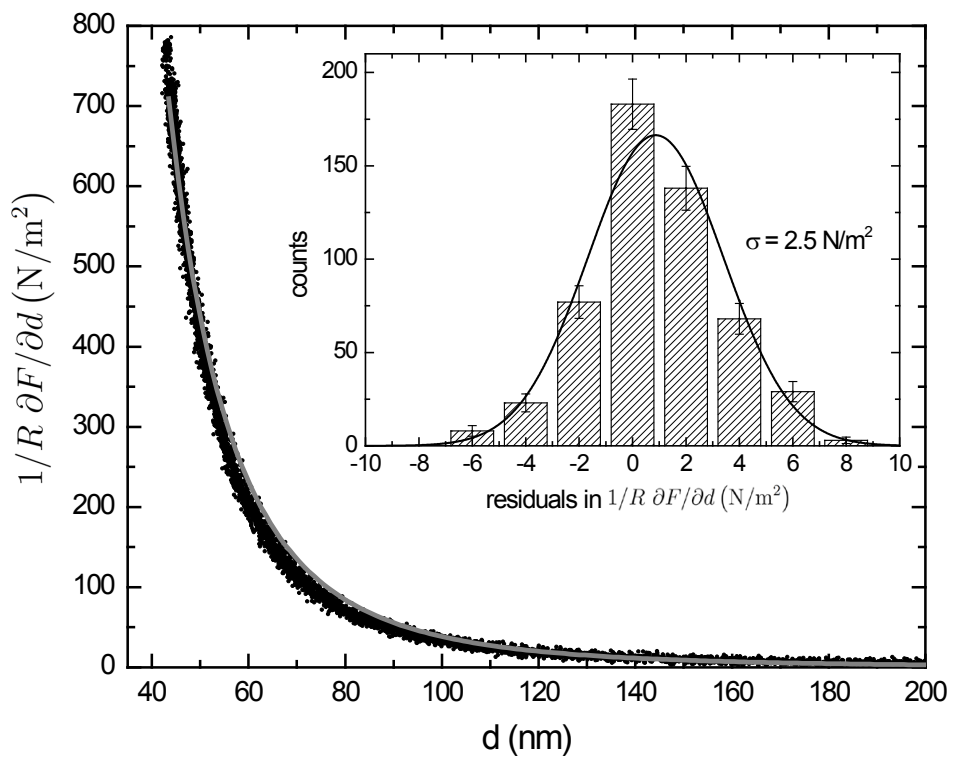


Figure 5.5: Dots: Measurements of the gradient of the Casimir force between the sphere and the plate (normalized to the radius of the sphere) as a function of separation as obtained during 10 consecutive scans. The grey line represents the result expected from theory. Inset: histogram of the residuals of the data between 160 nm and 200 nm.

voltage to the piezoelectric stage of the form $V_{\text{PZT}} \propto 1 - |t/\tau_s - 1|^3$, with $\tau_s = 500$ seconds. The frequency of the AC voltage was set to $\omega_1 = 72$ Hz. Its amplitude was continuously adjusted during the scan to keep the rms of the $2\omega_1$ electrostatic force component equal to roughly 230 pN at all separations (see [19, 20]). The oscillation frequency of the piezoelectric stage was set to $\omega_2 = 119$ Hz with 7.2 nm amplitude. Signals at $2\omega_1$ and ω_2 were demodulated with two lock-in amplifiers equipped with a 24dB low pass filter with RC time of 200 ms and 100 ms, respectively. To avoid mixing of the Casimir signal with that induced by the hydrodynamic force due to the air in the gap [20], the phase of the ω_2 lock-in amplifier was aligned with the phase of the oscillatory motion by going to contact, where the plate and the cantilever move synchronously. This procedure was performed only once before starting the measurement run.

Fig. 5.4 shows the potential difference V_0 needed to minimize the electrostatic interaction between the sphere and the plate as a function of separation d . The observed spread in the data is due to measurement noise and not to a time-related drift. It is clear that the data loosely follow a behavior like $a \log d + b$, as observed before in [19], [52], and [39]. This dependence is not yet fully understood.

Fig. 5.5 shows the Casimir force gradient as a function of separation. The data were obtained by subtracting from the original data an electrostatic contribution that arises from the calibration procedure [20]. This contribution, which scales like $1/d$, can be accurately calculated from the value of $S_{2\omega_1}$. In our experiment, this correction ranged from 15 N/m² at 200 nm up to 70 N/m² at 45 nm. The grey line in the graph represents the theoretical Casimir force as computed from the Lifshitz equation, where we have assumed that the dielectric function of the gold surfaces can be obtained by combining the tabulated data of reference [63] with the Drude term described in [95], and where we have neglected surface roughness corrections. The theoretical result should thus not be taken too rigorously. It is known, in fact, that gold layers deposited with different methods may have different optical properties, which can lead to significant differences in the resulting Casimir force [66]. Furthermore, surface roughness corrections can be as high as several tens of percent at the closest separations. A more refined calculation of the expected force is however outside our scope. The goal of this paper, in fact, is not to improve the accuracy in the comparison between theory and experiment, but to prove that ferrule-top cantilevers can be successfully used to obtain precise (i.e., low noise, small statistical error in force gradient) Casimir force measurements.

It is thus now important to discuss the statistical error in the Casimir force gradient. The inset of Fig. 5.5 shows a histogram of the residuals of all the Casimir force data collected in the separation range between 160 nm and 200 nm. The standard deviation is equal to 2.5 N/m². For comparison, our state-of-the-art atomic force microscope for Casimir force measurements is currently capable of achieving a standard deviation of 1.75 N/m² (see section 3.3) with

an ω_2 oscillation amplitude a factor of 2 lower but a ten times higher integration time.

5.3.4 Conclusions

We have presented a ferrule-top sensor for Casimir force experiments. The sensor is based on a monolithic miniaturized cantilever that is coupled to a remote readout via optical fibers. We have demonstrated that the setup provides measurements of the Casimir force between a sphere and a plate by means of a dynamic detection scheme. The sensor can be easily fabricated with cost effective techniques, allowing frequent substitution of the probe in systematic experiments. Furthermore, it adapts well to utilization in harsh environments, such as low temperatures, vacuum, and liquids. Similar ferrule-top devices can of course be used to investigate other long range interaction mechanisms as well. Ferrule-top technology can thus be considered as a new tool to explore phenomena that are of relevance in the future development of MEMS and NEMS.

Acknowledgements

This project was supported by the European Research Council under the European Community's Seventh Framework Programme (FP7/2007-2013)/ERC grant agreement number 201739, and by the Netherlands Organisation for Scientific Research (NWO) under the Innovational Research Incentives Scheme *Vernieuwingsimpuls* VIDI-680-47-209. The authors acknowledge useful discussions within the community supported by the ESF Research Network CASIMIR.

5.4 Simple fiber-optic interferometer with linear phase response

Abstract – Simple fiber-optic interferometers measure the path-length difference between the fiber end and a reflective surface by the intensity of the back-reflected light. Unfortunately, this signal is a sinusoidal function of the path-length difference and therefore the sensitivity of the interferometer depends strongly on the actual position of the reflective surface. Such interferometers are thus convenient when they can work continuously at high sensitivity (quadrature), for example for the detection of small cantilever motion, but are not capable of following larger movements with high precision, as needed in typical distance calibration procedures. We present a modified fiber-optic interferometer in which the position of the reflective surface is modulated slightly, causing an extra signal that is complementary to the total intensity signal. The right combination of both signals results in an output signal that is linear in the path-length difference and has constant sensitivity. This scheme can be highly beneficial in situations where simple fiber-optic interferometers are used for nm and sub-nm precision distance calibrations.

[†]This paper has been submitted: S. de Man and E. Jeffrey, 2010

Simple fiber-optic interferometers consist of an optical fiber and a mirror placed in front of it. The fiber-to-air interface and air-to-mirror interface form a low-finesse optical cavity, whose length variations can be determined by examining the light that propagates back into the fiber. Typically, one uses the intensity signal to measure these distance variations with sub-nm precision [94]. However, such a homodyne interference signal is only sensitive for specific cavity lengths, and therefore not practical for measurement schemes with relatively large (> 100 nm) distance variations (but practical, for example, to read out cantilever displacements). There were several attempts to overcome this problem by generating two quadrature interference signals, for example by using two fibers whose cleaved ends are separated by exactly an eighth of the wavelength [96, 97], or by switching the laser wavelength [98]. Recently, a simple fiber-optic interferometer with a diode array instead of a photodetector was used to examine the back-reflected light, also allowing the detection of quadrature signals [99]. In [100], an alternative scheme has been proposed based on modulation of the cavity length or laser wavelength to create two quadrature signals at the first and second harmonic of the modulation frequency, and a demonstration of the working principle for wavelength modulation is presented in [101]. In this note, we present measurements with an interferometric scheme that is similar to that proposed in [100], and show that one can easily generate two quadrature interference signals by slightly modulating the cavity length (couple of nm), achieving high sensitivity over large scan ranges. A big advantage of this scheme compared to wavelength modulation is that instead of a frequency tunable laser we can use a relatively inexpensive diode laser.

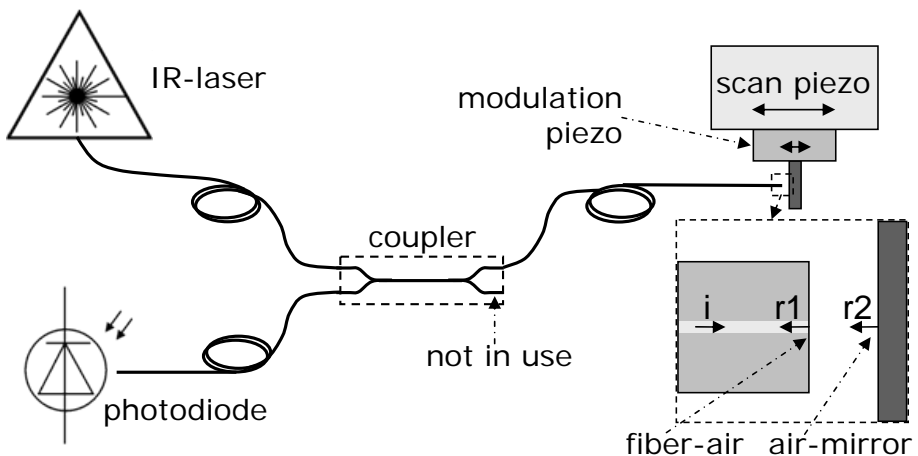


Figure 5.6: Schematic drawing of the experimental setup. See text for details.

Our simple fiber-optic interferometer consists of an infrared fiber-coupled laser source (Thorlabs S3FC-1310, wavelength $1.310\ \mu\text{m}$, 1 mW output power), an optical fiber coupler and an InGaAs photodetector (Thorlabs PDA10CS), as schematically shown in Fig. 5.6. The light coming from the laser is split by the fiber coupler into two branches. One of the branches functions as our interferometer (the upper branch in Fig. 5.6), while the other one is not used (the end is terminated with an angled cleave to avoid back-reflection). In the upper branch of Fig. 5.6 a reflective surface is placed in front of the fiber end. The task of the interferometer is to measure precisely the distance between the fiber end and this mirror, in order to calibrate the scanner piezo-electric stage to which it is attached. For typical applications, the distance between the fiber end and the mirror will be several mm or less. In this paper, we have used a gap of approximately 2 mm.

In a simple fiber-optic interferometer, the actual interference takes place between the light reflected by the fiber-to-air interface (r_1) and air-to-mirror interface (r_2), as shown in the magnified view of the fiber end and mirror in Fig. 5.6. The sum of both reflected signals r_1 and r_2 depends on their path length difference, which equals twice the gap size. The reflected light travels back through the fiber and is split in two by the coupler. The light propagating towards the laser is blocked by a faraday isolator (inside the laser housing), whereas the light that goes into the detector is our detection signal.

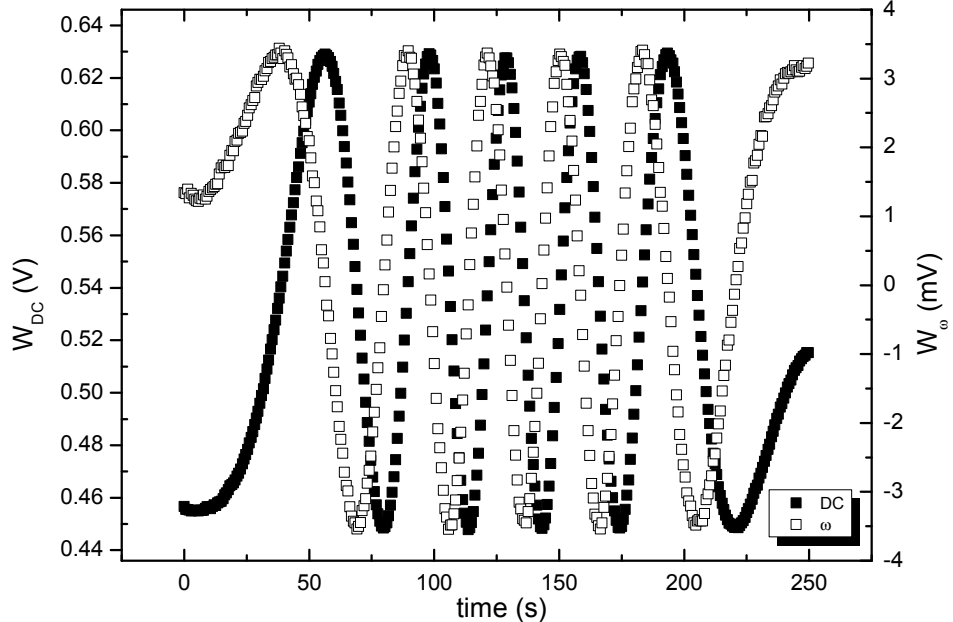


Figure 5.7: Raw data of the two interferometer signals W_{DC} and W_ω as a function of time for a single left-to-right sweep of the piezo-electric stage.

The output signal of the photodiode is given by [94]

$$W(d) = W_0 (1 - V \cos 4\pi d/\lambda) \quad (5.3)$$

where λ is the laser wavelength, d is the fiber-to-mirror distance, W_0 is the midpoint voltage, V is the fringe visibility, and we have ignored multiple reflections because of the very low finesse of our cavity. It is clear that the interferometer is only sensitive for changes in d at those values of d for which the cosine is steep, a major drawback of using this interferometric scheme. However, when we modulate the position of the sample as $d = d_{pz} + \Delta d \cos \omega t$ (with $\Delta d \ll \lambda/4\pi$) with an extra piezo-electric stage (modulation piezo in Fig. 5.6)[†], the photodiode signal becomes

$$W = W_{DC} + W_\omega \cos \omega t \quad (5.4)$$

$$W_{DC} = W_0 (1 - V \cos 4\pi d_{pz}/\lambda) \quad (5.5)$$

$$W_\omega = \frac{4\pi W_0 V \Delta d}{\lambda} \sin 4\pi d_{pz}/\lambda \quad (5.6)$$

The values of W_{DC} and W_ω can be measured with a low-pass filter and a lock-in amplifier at ω , respectively. The DC level of the photodiode voltage is measured with an ADC connected to a second order low-pass filter with a 1 Hz 3dB point. The small distance modulation Δd (2.8 nm RMS[§]) is performed at 119 Hz. The lock-in amplifier is locked at 119 Hz and uses a fourth order filter with a 100 ms integration time. To test this scheme, we have swept the scan piezo with a sinusoidal function with a period of 500 seconds and an amplitude of roughly 1.7 μm . In Fig. 5.7, we plot the recorded raw data of W_{DC} and W_ω as a function of time for a single left-to-right sweep during this very slow sinusoidal motion of the piezo-electric stage. Thus, besides the normal interferometric signal W_{DC} , we now have an extra signal W_ω . The advantage of the modulation scheme becomes clear now: W_{DC} and W_ω are related such that if one of them is not sensitive, the other is.

One could decide, at this point, to use then either W_{DC} or W_ω , depending on which signal is sensitive, and switching between them if necessary. However, it is even more convenient to combine both signals. For that, one displays the data as $\{W_{DC}, W_\omega\}$ coordinates for different values of d_{pz} in a Lissajous plot, as in Fig. 5.8. The resulting ellipse can be transformed into the unit circle by appropriate scaling (both axes) and translation (horizontal axis only). We define

$$X \equiv \frac{1 - W_{DC}/W_0}{V} = \cos 4\pi d_{pz}/\lambda \quad (5.7)$$

$$Y \equiv \frac{W_\omega \lambda}{4\pi W_0 V \Delta d} = \sin 4\pi d_{pz}/\lambda \quad (5.8)$$

[†]We chose to add an extra piezo stage instead of adding the oscillation to the motion of the scan piezo to ensure stability of the distance modulation amplitude.

[§]It will become clear later in the text how this is measured.

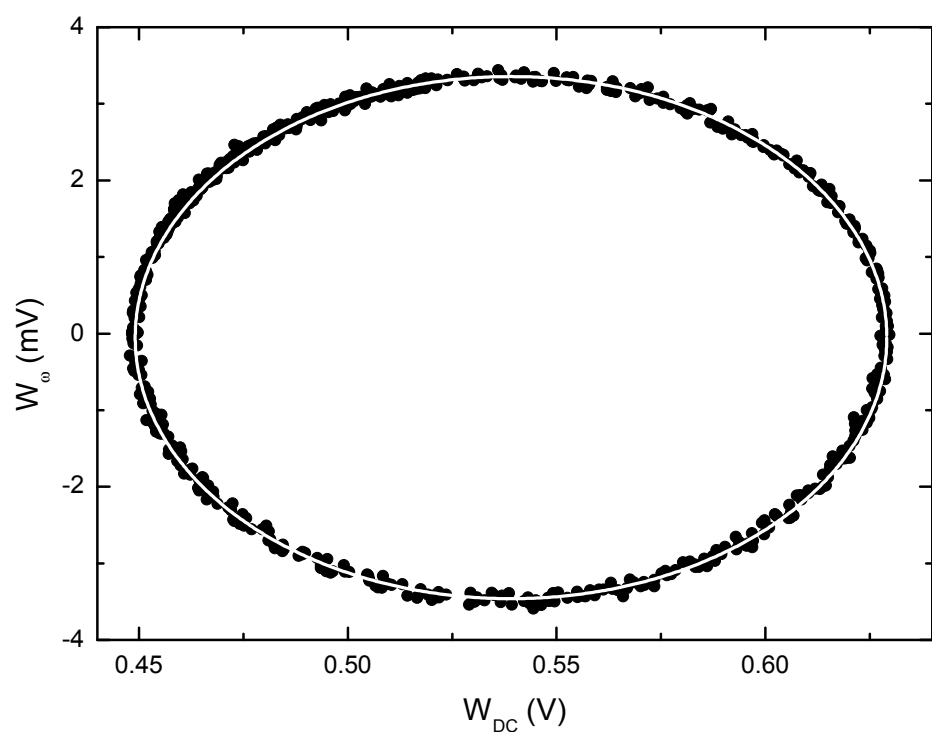


Figure 5.8: Raw data of the two interferometer signals W_{DC} and W_ω in a Lissajous plot (black circles). Fit of the data as used for the conversion to phase (white line).

We then find the values of W_0 , V , and $4\pi W_0 V \Delta d / \lambda$ by a minimization procedure that fits the unit circle to our $\{X, Y\}$ data-points. The fitted circle is displayed in Fig. 5.8 by the white line intersecting the black data-points. The amount of $\{X, Y\}$ data-points belonging to consecutive d_{pz} values one can use in this fit procedure depends on the stability of the laser wavelength and output power (they are assumed to be constant). It is interesting to note that by combining the obtained values of the three fit parameters we get the amplitude of the piezo oscillation Δd (λ is known). It is now straightforward to find the actual motion of the piezo-electric stage, d_{pz} , by

$$d_{pz} = \frac{\lambda}{4\pi} \arctan2(Y, X) \quad (5.9)$$

where $\arctan2$ is the four-quadrant arctangent of Y/X . Since changes in d_{pz} are translated linearly into changes of the phase-angle of $\{X, Y\}$, Eq. 5.9 represents the fact that our interferometer has a linear phase response. Therefore, the interferometer is now also sensitive to the direction of the mirror movement, contrary to normal readouts. As the arctangent is a periodic function of its argument, we can only find d_{pz} up to integer multiples of $\lambda/2$. However, as long as the scanning speed of the piezo is much lower than $\lambda/2$ per integration time, it is easy to detect the discontinuities in the signal and to unwrap the phase of $\arctan(Y/X)$, allowing for convenient scanning of multiple interference fringes. In Fig. 5.9, we have plotted d_{pz} as obtained from Eq. 5.9 for the raw phase of $\{X, Y\}$ in open squares and for the unwrapped phase in filled squares. It is clear that a very simple algorithm suffices to detect the discontinuities in the raw data and add appropriate multiples of $\lambda/2$ to d_{pz} .

To examine the noise level of our interferometer, we have selected roughly 200 data-points very close to each of the $\{X, Y\}$ coordinates $\{1, 0\}$, $\{-1, 0\}$, $\{0, 1\}$, and $\{0, -1\}$. Those 800 points come from a data set that spanned roughly 26 hours of continuous measurements. In order to be insensitive to slow variation of the laser output power, the fitting of the unit circle was performed on 250 s portions (separate trace and retrace scans of the piezo-electric stage). At $\{1, 0\}$ and $\{-1, 0\}$ (representing pure W_{DC} measurements), the noise in X is normally distributed with a standard deviation of 0.005, resulting in a phase error of 5 mrad at $\{0, 1\}$ and $\{0, -1\}$. At $\{0, 1\}$ and $\{0, -1\}$ (corresponding to W_ω measurement only), the noise in Y is normally distributed with a standard deviation of 0.012, resulting in a phase error of 12 mrad at $\{1, 0\}$ and $\{-1, 0\}$. Therefore, the noise in d_{pz} varies between minimum values of 0.5 nm and maximum values of 1.2 nm during scanning. This noise is most likely due to frequency (or phase) noise of the laser diode, that results in an equivalent distance noise δd due to a wavelength variation $\delta\lambda$ by $\delta d = d(\delta\lambda/\lambda)$ [94]. As our cavity is rather large (roughly 2 mm), a wavelength variation $\delta\lambda/\lambda$ of only 5×10^{-7} would be sufficient to generate the observed noise. Such an amount of wavelength variation is typical for laser

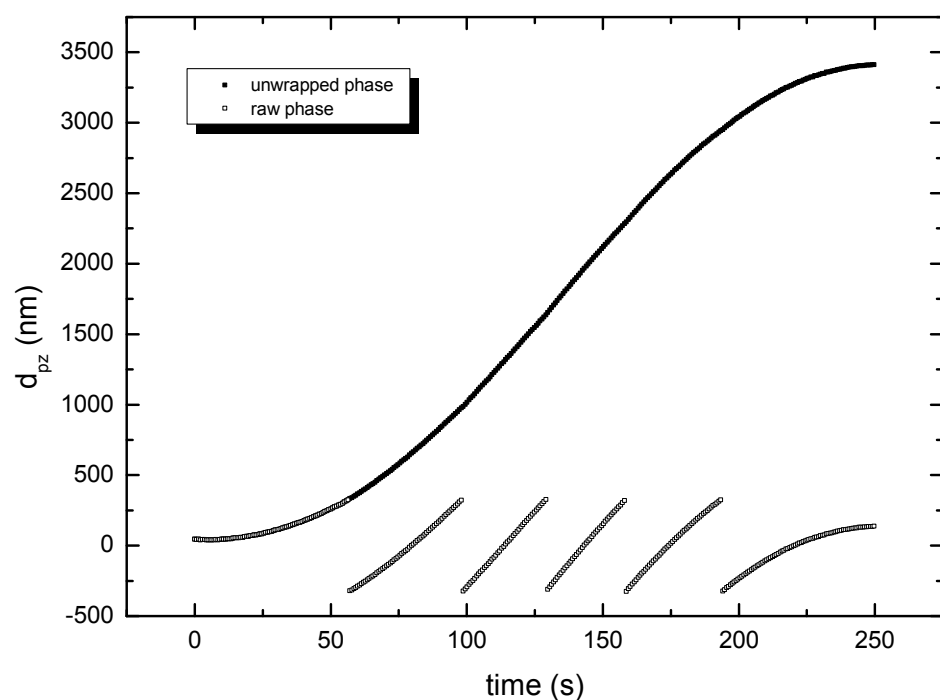


Figure 5.9: Piezo movement d_{pz} for a single left-to-right trace (same scan as Fig. 5.7) as a function of time.

diodes [94]. Obviously, the precision of the interferometer can be enhanced by working at smaller gap sizes. Anyway, even with such a large gap as used here, the movement of the piezo-electric stage can be calibrated with nm precision, which is sufficient for most applications.

In addition to intrinsic laser frequency noise, there are two other sources of error. Lasers are sensitive to light coupled back into the laser cavity which can cause amplitude and frequency fluctuations and mode-hopping. The S3FC-1310 has a built-in isolator to reduce this effect, but it does not eliminate the problem entirely. In addition, unwanted reflections from other fiber ends also cause fabry-perot interference. Both of these problems are greatly reduced by using FC/APC fiber termination at the unused port and the detector and by intensity modulating the laser at 30 kHz. The intensity modulation decreases the coherence length of the laser considerably, reducing the visibility of the unwanted fabry-perot interferences while not significantly affecting the visibility from the 2 mm gap.

It is important to mention that it is necessary to maintain relatively slow scan speeds of the piezo-electric stage. If the changes in both W_{DC} and W_ω as a function of time become comparable to the bandwidths of the low-pass filters (both the low-pass filter on W_{DC} and the one in the lock-in amplifier), then distortion of the circular relation between those quantities occurs; as the signals vary more rapidly close to their maxima and minima, their maxima and minima will be mostly reduced, resulting in non-linear compression of the data. Therefore, the data as presented in Fig. 5.8 would look more square-like for too fast scan speeds. Obviously, it becomes then hard to extract the phase.

Furthermore, we would like to stress that it is of course also possible to modulate the position of the fiber instead of the sample, suggesting that this technique can be widely employed for distance calibration in all kinds of setups. It is interesting to note as well that the scheme presented here can also be used for interferometric vibration measurements by increasing the detection bandwidth and modulation frequency.

The authors thank G. Gruca, K. Heeck and D. Iannuzzi for useful discussions. This work was financially supported by the Netherlands Organisation for Scientific Research (NWO), under the Innovational Research Incentives Scheme VIDI-680-47-209.

Appendix

Appendix A

Calculation of the Casimir force

With the Lifshitz equation, one can calculate the pressure of the Van der Waals interaction between parallel plates of materials A and B [41]:

$$P_{pp}(d) = \frac{k_B T}{\pi c^3} \sum_{n=0}^{\infty}' \xi_n^3 \int_1^{\infty} p^2 \left(\frac{1}{\overline{\Delta}_A^{-1} \overline{\Delta}_B^{-1} e^{r_n p} - 1} + \frac{1}{\Delta_A^{-1} \Delta_B^{-1} e^{r_n p} - 1} \right) dp, \quad (\text{A.1})$$

where the prime on the summation indicates that the $n = 0$ term has to be multiplied by $1/2$, T is the temperature, $\xi_n = 2\pi k_B T n / \hbar$ is the n -th Matsubara frequency, k_B , \hbar and c are the usual fundamental constants, and

$$r_n = 2d\xi_n/c, \overline{\Delta}_j = \frac{p \varepsilon_j(i\xi_n) - s_j}{p \varepsilon_j(i\xi_n) + s_j}, \Delta_j = \frac{p - s_j}{p + s_j}, s_j = \sqrt{p^2 - 1 + \varepsilon_j(i\xi_n)}. \quad (\text{A.2})$$

The dielectric function $\varepsilon_j(i\xi)$ evaluated at imaginary frequency $i\xi$ is obtained from the Kramers-Kronig relation

$$\varepsilon(i\xi) = 1 + \frac{2}{\pi} \int_0^{\infty} \frac{\omega \varepsilon_2(\omega)}{\omega^2 + \xi^2} d\omega. \quad (\text{A.3})$$

where $\varepsilon_2(\omega)$ is the imaginary part of the dielectric function. We evaluate Eq. A.3 for gold by obtaining $\varepsilon_2(\omega)$ from [63] and extrapolate the data with a Drude model for low frequencies (parameters from [27]). For ITO, we substitute the $\varepsilon_2(\omega)$ from the combined Drude and Tauc-Lorentz models with parameters from [64].

Note that in all equations above, we have set the magnetic permeability of both surfaces and air to unity, and the electric permittivity of air equal to one as well. Since the ITO and Au layers are described with Drude models at low frequencies, we take $\overline{\Delta}_j = 1$ and $\Delta_j = 0$ at ξ_0 . P_{pp} is calculated by summing the first 100 Matsubara frequencies at $T = 300$ K. The force gradient between a sphere and a plate is then obtained from Eq. 3.12.

Bibliography

- [1] F. W. DelRio, M. P. de Boer, J. A. Knapp, E. D. Reedy, P. G. Clews, and M. L. Dunn, *Nat. Mater.* **4**, 629 (2005).
- [2] H. B. Chan, V. A. Aksyuk, R. N. Kleiman, D. J. Bishop, and F. Capasso, *Science* **291**, 1941 (2001).
- [3] H. B. Chan, V. A. Aksyuk, R. N. Kleiman, D. J. Bishop, and F. Capasso, *Phys. Rev. Lett.* **87**, 211801 (2001).
- [4] F. M. Serry, D. Walliser, and G. J. Maclay, *J. Appl. Phys.* **84**, 2501 (1998).
- [5] F. Capasso, J. N. Munday, D. Iannuzzi, and H. B. Chan, *IEEE J. Sel. Top. Quantum Electron.* **13**, 400 (2007).
- [6] O. Kenneth, I. Klich, A. Mann, and M. Revzen, *Phys. Rev. Lett.* **89**, 33001 (2002).
- [7] J. N. Munday, D. Iannuzzi, Y. Barash, and F. Capasso, *Phys. Rev. A* **71**, 42102 (2005).
- [8] P. Ball, *Nature* **447**, 772 (2007).
- [9] P. Ball, *Nat. Mater.* **6**, 402 (2007).
- [10] P. Ball, *Nat. Mater.* **8**, 705 (2009).
- [11] M. A. Bevan and D. C. Prieve, *Langmuir* **15**, 7925 (1999).
- [12] J. Israelachvili, *Intermolecular and Surface Forces* (Academic Press, New York, 1992).
- [13] J. N. Munday and F. Capasso, *Phys. Rev. A* **75**, 60102 (2007).
- [14] J. N. Munday, F. Capasso, and V. A. Parsegian, *Nature* **457**, 170 (2009).
- [15] S. Lee and W. M. Sigmund, *J. Colloid. Interf. Sci.* **243**, 365 (2001).
- [16] S. Lee and W. M. Sigmund, *Colloid Surface A* **204**, 43 (2002).

- [17] A. Milling, P. Mulvaney, and I. Larson, *J. Colloid Interface Sci.* **180**, 460 (1996).
- [18] H. B. G. Casimir, *Proc. K. Ned. Akad. Wet.* **51**, 793 (1948).
- [19] S. de Man, K. Heeck, and D. Iannuzzi, *Phys. Rev. A* **79**, 024102 (2009).
- [20] S. de Man, K. Heeck, R. J. Wijngaarden, and D. Iannuzzi, *Phys. Rev. Lett.* **103**, 040402 (2009).
- [21] P. W. Milonni, *The quantum vacuum: an introduction to quantum electrodynamics* (Academic Press, San Diego, 1993).
- [22] P. W. Milonni, R. J. Cook, and M. E. Goggin, *Phys. Rev. A* **38**, 1621 (1988).
- [23] E. M. Lifshitz, *Sov. Phys. JETP* **2**, 73 (1956).
- [24] M. J. Sparnaay, *Physica* **24**, 751 (1958).
- [25] P. H. G. M. van Blokland and J. T. G. Overbeek, *J. Chem. Soc., Far. Trans.* **1**, 2637 (1978).
- [26] S. K. Lamoreaux, *Phys. Rev. Lett.* **78**, 5 (1997).
- [27] M. Bordag, U. Mohideen, and V. M. Mostepanenko, *Phys. Rep.* **353**, 1 (2001).
- [28] M. Masuda and M. Sasaki, *Phys. Rev. Lett.* **102**, 171101 (2009).
- [29] G. Bressi, G. Carugno, R. Onofrio, and G. Ruoso, *Phys. Rev. Lett.* **88**, 041804 (2002).
- [30] R. S. Decca, D. Lopez, E. Fischbach, and D. E. Krause, *Phys. Rev. Lett.* **91**, 50402 (2003).
- [31] R. S. Decca, D. Lopez, E. Fischbach, G. L. Klimchitskaya, D. E. Krause, and V. M. Mostepanenko, *Ann. Phys. - New York* **318**, 37 (2005).
- [32] D. Iannuzzi, M. Lisanti, and F. Capasso, *Proc. Natl. Acad. Sci. U.S.A.* **101**, 4019 (2004).
- [33] M. Lisanti, D. Iannuzzi, and F. Capasso, *Proc. Natl. Acad. Sci. U.S.A.* **102**, 11989 (2005).
- [34] W. A. Ducker, T. J. Senden, and R. M. Pashley, *Nature* **353**, 239 (1991).
- [35] U. Mohideen and A. Roy, *Phys. Rev. Lett.* **81**, 4549 (1998).

- [36] G. Jourdan, A. Lambrecht, F. Comin, and J. Chevrier, *Europhys. Lett.* **85**, 31001 (2009).
- [37] G. Torricelli *et al.*, *Phys. Rev. A* **82**, 010101(R) (2010).
- [38] W. J. Kim, M. Brown-Hayes, D. A. R. Dalvit, J. H. Brownell, and R. Onofrio, *Phys. Rev. A* **78**, 020101(R) (2008).
- [39] S. de Man, K. Heeck, R. J. Wijngaarden, and D. Iannuzzi, *J. Vac. Sci. Technol. B* **28**, C4A25 (2010).
- [40] M. Nonnenmacher, M. P. O'Boyle, and H. K. Wickramasinghe, *Appl. Phys. Lett.* **58**, 2921 (1991).
- [41] V. A. Parsegian, *Van der Waals Forces* (Cambridge University Press, New York, 2006).
- [42] L. M. Hocking, *J. Eng. Math.* **7**, 207 (1973).
- [43] O. I. Vinogradova, *Langmuir* **11**, 2213 (1995).
- [44] J. N. Huiberts *et al.*, *Nature* **380**, 231 (1996).
- [45] D. Iannuzzi, S. Deladi, V. J. Gadgil, R. G. P. Sanders, H. Schreuders, and M. C. Elwenspoek, *Appl. Phys. Lett.* **88**, 053501 (2006).
- [46] D. Iannuzzi, M. Slaman, J. H. Rector, H. Schreuders, S. Deladi, and M. C. Elwenspoek, *Sensors and Actuators B: Chemical* **121**, 706 (2007).
- [47] D. Iannuzzi, S. Deladi, J. W. Berenschot, S. de Man, K. Heeck, and M. C. Elwenspoek, *Review of Scientific Instruments* **77**, 106105 (2006).
- [48] C. J. Alberts, S. de Man, J. W. Berenschot, V. J. Gadgil, M. C. Elwenspoek, and D. Iannuzzi, *Measurement Science and Technology* **20**, 034005 (2009).
- [49] D. Iannuzzi *et al.*, *Measurement Science and Technology* **18**, 3247 (2007).
- [50] G. Gruca, S. de Man, M. Slaman, and J. H. Rector, *Meas. Sci. Technol.* **21**, 094033 (2010).
- [51] D. Chavan *et al.*, *Review of Scientific Instruments* **81**, 123702 (2010).
- [52] W. J. Kim, A. O. Sushkov, D. A. R. Dalvit, and S. K. Lamoreaux, *Phys. Rev. Lett.* **103**, 60401 (2009).
- [53] G. Torricelli, S. Thornton, C. Binns, I. Pirozhenko, and A. Lambrecht, *Journal of Vacuum Science & Technology B: Microelectronics and Nanometer Structures* **28**, C4A30 (2010).

- [54] R. S. Decca, D. Lopez, E. Fischbach, G. L. Klimchitskaya, D. E. Krause, and V. M. Mostepanenko, Phys. Rev. D **75**, 77101 (2007).
- [55] W. R. Smythe, *Static and dynamic electricity* (McGraw Hill, New York, 1939).
- [56] S. K. Lamoreaux, ArXiV 0808.0885 (2008).
- [57] S. E. Pollack, S. Schlamminger, and J. H. Gundlach, Phys. Rev. Lett. **101**, 071101 (2008).
- [58] W. J. Kim, A. O. Sushkov, D. A. R. Dalvit, and S. K. Lamoreaux, Phys. Rev. A **81**, 022505 (2010).
- [59] D. J. Griffiths, *Introduction to Electrodynamics* (Prentice Hall, Upper Saddle River, 1999).
- [60] F. Chen, G. L. Klimchitskaya, V. M. Mostepanenko, and U. Mohideen, Phys. Rev. B **76**, 035338 (2007).
- [61] F. Chen, U. Mohideen, G. L. Klimchitskaya, and V. M. Mostepanenko, Phys. Rev. A **72**, 20101 (2005).
- [62] G. Bressi, G. Carugno, A. Galvani, R. Onofrio, G. Ruoso, and F. Veronese, Classical Quantum Gravity **18**, 3943 (2001).
- [63] E. D. Palik, *Handbook of Optical Constants of Solids* (Academic Press, San Diego, 1998).
- [64] H. Fujiwara and M. Kondo, Phys. Rev. B **71**, 75109 (2005).
- [65] S. de Man and D. Iannuzzi, New J. Phys. **8**, 235 (2006).
- [66] V. B. Svetovoy, P. J. van Zwol, G. Palasantzas, and J. T. M. D. Hosson, Phys. Rev. B **77**, 35439 (2008).
- [67] A. A. Maradudin and P. Mazur, Phys. Rev. B **22**, 1677 (1980).
- [68] A. Maali and B. Bhushan, Phys. Rev. E **78**, 27302 (2008).
- [69] C. D. F. Honig, J. E. Sader, P. Mulvaney, and W. A. Ducker, Phys. Rev. E **81**, 056305 (2010).
- [70] R. Onofrio, New J. Phys. **8**, 237 (2006).
- [71] D. Iannuzzi, M. Lisanti, J. N. Munday, and F. Capasso, Solid state commun. **135**, 618 (2005).

- [72] D. Iannuzzi, M. Lisanti, J. N. Munday, and F. Capasso, *J. Phys. A - Math. Gen.* **39**, 6445 (2006).
- [73] D. Iannuzzi, I. Gelfand, M. Lisanti, and F. Capasso, *Quantum Field Theory Under the Influence of External Conditions* (2004).
- [74] T. J. Richardson, J. L. Slack, B. Farangis, and M. D. Rubin, *Appl. Phys. Lett.* **78**, 3047 (2001).
- [75] H. Ibach and H. Lüth, *Solid-State Physics* (Springer-Verlag, Berlin, 2003).
- [76] W. Lohstroh *et al.*, *Phys. Rev. B* **70**, 165411 (2004).
- [77] W. Lohstroh, R. J. Westerwaal, J. L. M. V., H. Schreuders, B. Dam, and R. Griessen, *J. Alloys Comp.* **430**, 13 (2007).
- [78] J. L. M. van Mechelen *et al.*, *Appl. Phys. Lett.* **84**, 3651 (2004).
- [79] N. W. Ashcroft and N. D. Mermin, *Solid State Physics* (Saunders College, Philadelphia, 1976).
- [80] S. Enache, W. Lohstroh, and R. Griessen, *Phys. Rev. B* **69**, 115326 (2004).
- [81] V. A. Parsegian and B. W. Ninham, *J. Theor. Biol.* **38**, 101 (1973).
- [82] M. A. Ordal, R. J. Bell, R. W. Alexander, L. L. Long, and M. R. Querry, *Appl. Optics* **24**, 4493 (1985).
- [83] W. Lohstroh *et al.*, *Phys. Rev. Lett.* **93**, 197404 (2004).
- [84] R. J. Westerwaal *et al.*, *J. Appl. Phys.* **100**, 063518 (2006).
- [85] A. Borgschulte *et al.*, *Appl. Surf. Sci.* **253**, 1417 (2006).
- [86] F. J. A. den Broeder *et al.*, *Nature* **394**, 656 (1998).
- [87] S. J. van der Molen, M. S. Welling, and R. Griessen, *Phys. Rev. Lett.* **85**, 3882 (2000).
- [88] G. Gruca, S. de Man, M. Slaman, J. H. Rector, and D. Iannuzzi, *Proc. SPIE* **7503**, PDP 07 (2009).
- [89] F. Chen, G. L. Klimchitskaya, V. M. Mostepanenko, and U. Mohideen, *Phys. Rev. Lett.* **97**, 170402 (2006).
- [90] H. B. Chan *et al.*, *Phys. Rev. Lett.* **101**, 30401 (2008).

- [91] S. de Man, K. Heeck, R. J. Wijngaarden, and D. Iannuzzi, *Int. J. Mod. Phys. A* **25**, 2231 (2010).
- [92] M. Bao and H. Yang, *Sensors & Actuators: A. Physical* **136**, 3 (2007).
- [93] S. Deladi, D. Iannuzzi, V. J. Gadgil, H. Schreuders, and M. C. Elwenspoek, *J. Micromech. Microeng.* **16**, 886 (2006).
- [94] D. Rugar, H. J. Mamin, and P. Guethner, *Appl. Phys. Lett.* **55**, 2588 (1989).
- [95] A. Lambrecht and S. Reynaud, *Eur. Phys. J. D* **8**, 309 (2000).
- [96] K. A. Murphy, M. F. Gunther, A. M. Vengsarkar, and R. O. Claus, *Opt. Lett.* **16**, 273 (1991).
- [97] J. L. Santos and D. A. Jackson, *Opt. Lett.* **16**, 1210 (1991).
- [98] A. D. Kersey, D. A. Jackson, and M. Corke, *Electron. Lett.* **19**, 102 (1983).
- [99] H. J. Konle, M. Spitalny, C. O. Paschereit, F. Bake, and I. Röhle, *Meas. Sci. Technol.* **21**, 075305 (2010).
- [100] K. Karrai, Patent WO2009043421 (A1) (2009).
- [101] K. Karrai and P. F. Braun, *Proceedings EUSPEN 2010* 156V1 (2010).

Summary

Vacuum is not empty. Even in the absence of electromagnetic sources, vacuum is filled with zero-point fluctuations of the electromagnetic field. These fluctuations give rise to quantum mechanical effects like spontaneous emission of radiation and the Lamb shift. In 1948, Casimir realized that these zero-point fluctuations could also have an effect on macroscopic objects. He considered two perfectly conducting and electrically neutral plates placed inside a vacuum filled with electromagnetic fluctuations. The plates set zero-field boundary conditions on the fluctuations, and Casimir showed that the total energy of the fluctuations depends on the separation between the plates. Hence, the vacuum field exerts a force on the plates: the Casimir force. This force is generally weak, but it grows quickly as the plates are moved closer to one another. In the sub-micrometer range, the Casimir force becomes relevant, and below 100 nm it is quite strong.

In 1956, Lifshitz generalized the theory in order to treat plates made out of real materials, instead of perfectly conducting surfaces. His work was mathematically complicated, but the results are fascinating. His theory converges to Casimir's result for perfectly conducting plates, but also recovers the Van der Waals force for objects at very close separation (let's say < 10 nm). He had thus unified the Casimir force and the Van der Waals force, and showed that both effects arise from the zero-point fluctuations of the electromagnetic field. In fact, the only difference between the Casimir and the Van der Waals force lies in the range of the interaction; at large distances, the finite speed of light and the corresponding retardation of the electromagnetic field has to be taken into account, whereas at small separation this retardation can be neglected.

The Casimir force is experimentally verified by many experiments, and only few very subtle questions regarding its strength remain unsolved. These questions mainly arise because of the real material properties one has to supply to the theory in order to calculate the force. In this work, we have not focused on trying to solve these subtle issues, but rather to investigate more practical aspects of the Casimir force. For instance, we have investigated how to switch the force with hydrogen switchable mirrors, and showed that by using a transparent conductive oxide as the plate material (used in touch screens) the strength of the Casimir interaction is halved, a practical solution for reducing the force in small mechanical and electrical devices.

We have developed an experimental setup to measure precisely the Casimir force. The two objects that are attracted to each other by the Casimir force are a small plate and a small sphere. We use this geometry instead of two plates, because it is experimentally quite involved to keep two plates parallel. The sphere has a radius of $100 \mu\text{m}$ and is attached to a small cantilever (about half a millimeter long). When the Casimir force attracts the sphere towards the plate, this cantilever is bended. Using a laser reflected from the end of the cantilever, we can determine the force precisely. To measure the force as a function of the distance between the surfaces, we can alter the position of the plate with a piezoelectric transducer with sub-nm accuracy. All these parts are attached to a rigid aluminum block that is temperature controlled to reduce mechanical drifts, and placed on an active vibration isolation system to reduce mechanical noise. The setup is placed inside an anechoic chamber inside a temperature controlled laboratory. We have achieved roughly 100 times smaller drifts as in comparable room temperature Casimir force setups.

In order to make accurate force measurements, the setup has to be calibrated with a known force. For that we use the electrostatic force, because its characteristics are well known and it is easily controllable by applying an external voltage difference to the interacting surfaces. Instead of performing separate calibration and measurement runs, we have developed a measurement scheme in which calibration and Casimir force measurement can be performed simultaneously. By using an oscillating voltage applied between the surfaces at a low frequency and a lock-in amplifier examining the cantilever deflection at twice this modulation frequency, we can precisely measure the electrostatic force, without being bothered by the Casimir effect. By modulating the distance between the sphere and the plate with a few nm at a different frequency, we can use another lock-in amplifier to detect the gradient of force between the objects. At short distances, this force gradient consists mainly of the Casimir force gradient, because the Casimir force is much more dependent on distance than the electrostatic force. In this way, we can calibrate and measure the Casimir force at two distinct frequencies, thereby acquiring both signals simultaneously.

For a good measurement of the Casimir force, it is essential to remove any spurious background forces that might hide the Casimir effect. One such a force is the electrostatic force that arises from the natural electric potential difference between the two surfaces. Even if both surfaces are electrically grounded together, their different work functions (also possible in the case of the same material on both surfaces) will cause an electric force. Therefore, the experimentalist has to supply a counter bias to the surfaces, to correct for the difference in work functions and remove this electric force. Our modulation scheme offers a neat way to accomplish this. It turns out that by using another lock-in amplifier locked to the voltage modulation, we can create a negative feedback loop that automatically compensates for the difference in work func-

tions by applying a DC voltage that minimized the electrostatic force. Thus, in our measurements, the difference in work functions is always compensated. In our experiments, we have found that this voltage can depend on time and separation between the surfaces, which we discuss in detail in this thesis.

The mechanical modulation of the separation between the surfaces that facilitates the measurement of the Casimir force gradient also causes a hydrodynamic interaction between the small sphere and the plate. Since this hydrodynamic interaction is dissipative, it manifests itself 90 degrees phase-shifted with respect to the Casimir force gradient, and it can be independently measured with a lock-in amplifier. In fact, our setup can provide very precise measurements of the hydrodynamic force, and we have carried out measurements in air, nitrogen, helium and SF_6 gas. These measurements are in good agreement with theory.

During our research on the Casimir effect and the development of our setup, a new optical fiber based force sensor has been invented in our research group: the fiber-top cantilever. This sensor is a normal optical fiber of which the end is machined in the form of a cantilever by focused ion beam milling. The deflection of the cantilever in response to external forces can be accurately determined by sending light inside the optical fiber and measuring the intensity of the light that is reflected back into the fiber by the cantilever. Later on, this design was slightly modified by carving the cantilever out of a ferruled fiber, which is a piece of glass that is glued around the fiber. This design is bigger (roughly 2 mm diameter), but the cantilever can be made weaker (i.e. more sensitive). We have demonstrated that this sensor can be effectively used to measure the Casimir force, which opens up the possibility to investigate Casimir forces in conditions that are not suitable for conventional force sensors, like explosive environments, liquids or cryogenic setups.

In these 4 years of research on the Casimir effect, we have built a new setup and used it to investigate the electrostatic force, the work function difference between the interacting surfaces, the hydrodynamic force in various gaseous atmospheres, and the Casimir force between different materials. Most notably, we have shown that the Casimir force between a gold surface and a surface coated with indium-tin-oxide is a factor 2 weaker than the force between two gold surfaces.

Samenvatting

Vacuüm is niet leeg. Zelfs in de afwezigheid van bronnen van elektromagnetische straling is het vacuüm gevuld met nulpunts-fluctuaties van het elektromagnetische veld. Deze fluctuaties leiden tot kwantummechanische effecten als spontane emissie van straling en de Lamb verschuiving. In 1948 besefte Casimir dat deze nulpunts-fluctuaties ook invloed konden hebben op macroscopische voorwerpen. Hij beschouwde twee perfect geleidende en elektrisch neutrale platen in dit vacuüm gevuld met elektromagnetische fluctuaties. De platen fungeren als nul-veld randvoorwaarden voor de fluctuaties, en Casimir heeft laten zien dat de totale energie van de fluctuaties afhankelijk is van de afstand tussen de platen. Daarom oefent het vacuüm veld een kracht uit op de platen: de Casimir kracht. Deze kracht is in het algemeen zwak, maar hij groeit snel wanneer de platen dichter bij elkaar gebracht worden. Voor afstanden beneden de micrometer wordt de Casimir kracht relevant en onder de 100 nm is hij behoorlijk sterk.

In 1956 heeft Lifshitz de theorie veralgemeiniseerd zodat hij platen van echte materialen kon begrijpen, in plaats van de perfect geleidende oppervlakken. Zijn werk was wiskundig ingewikkeld, maar de resultaten zijn fascinerend. De theorie convergeert naar het resultaat van Casimir voor perfect geleidende platen, maar leidt ook tot de Van der Waals kracht voor objecten op zeer korte afstand van elkaar (zeg maar < 10 nm). Hij had dus de Casimir kracht en de Van der Waals kracht geïnificeerd, en laten zien dat beide effecten voortkomen uit de nulpunts-fluctuaties van het elektromagnetische veld. In feite blijkt het enige verschil tussen de Casimir en Van der Waals kracht te liggen in de dracht van de interactie: op grote afstand moet de eindigheid van de lichtsnelheid en de daaruit voortvloeiende retardatie van het elektromagnetische veld meegenomen worden, terwijl voor kleine afstanden deze retardatie verwaarloosd kan worden.

De Casimir kracht is experimenteel geverifieerd door veel experimenten en slechts enkele zeer subtile vragen over de sterkte van de interactie zijn nog onopgelost. Deze vragen zijn voornamelijk het gevolg van het moeten invullen van de echte materiaaleigenschappen in de theorie om de kracht uit te kunnen rekenen. In dit werk hebben wij niet getracht deze subtile vragen op te lossen, maar gefocust op het onderzoeken van meer praktische aspecten van de Casimir kracht. We hebben bijvoorbeeld onderzocht hoe we de kracht in sterkte kunnen

omschakelen met schakelbare spiegels en we hebben laten zien dat door gebruik te maken van transparante geleidende oxiden (zoals gebruikt in touch screens) de sterkte van de Casimir kracht gehalveerd wordt, een praktische oplossing om de kracht te verkleinen in kleine mechanische en elektrische machientjes.

Wij hebben een experimentele opstelling ontwikkeld om de Casimir kracht precies te meten. De twee objecten die door de Casimir kracht naar elkaar toe getrokken worden zijn een kleine plaat en een kleine bol. We werken met deze geometrie in plaats van twee platen, omdat het experimenteel behoorlijk moeilijk is om twee platen parallel te houden. De bol heeft een straal van $100 \mu\text{m}$ en is bevestigd aan een klein bladveertje (ongeveer een halve millimeter lang). Wanneer de Casimir kracht de bol naar de plaat toetrekt, dan wordt het bladveertje gebogen. Met een laser die op het uiteinde van het bladveertje schijnt kunnen we precies de sterkte van de kracht bepalen. Om dan ook nog de kracht als functie van de afstand tussen de oppervlakken te kunnen meten, kunnen we de positie van de plaat instellen met een piezoelektrische verschuiver met een nauwkeurigheid beter dan een nanometer. Al deze onderdelen zijn bevestigd op een stevig aluminium blok dat temperatuur gestabiliseerd is om thermische uitzettingen te beperken, en dit alles is geplaatst op een actief anti-vibratie platform om mechanische ruis te beperken. De opstelling bevindt zich binnen in een dode kamer in een temperatuur gestabiliseerd laboratorium. We hebben een honderdvoudige verkleining van het weglopen van de opstelling kunnen bereiken in vergelijking tot andere kamertemperatuur Casimir kracht opstellingen.

Om accurate krachtmetingen uit te kunnen voeren moet de experimentele opstelling gekalibreerd zijn. Wij gebruiken daarvoor de elektrostatische kracht, omdat de karakteristieken goed bekend zijn en deze makkelijk te manipuleren is door een spanningsverschil tussen de twee oppervlakken aan te leggen. In plaats van afzonderlijke kalibreer en meet series uit te voeren, hebben wij een meetmethode ontwikkeld waarbij kalibreren en het meten van de Casimir kracht simultaan kan worden uitgevoerd. Door een langzaam oscillerend spanningsverschil tussen de oppervlakken aan te leggen en een lock-in versterker te gebruiken die de buiging van het bladveertje op tweemaal deze frequentie detecteert, kunnen we nauwkeurig de elektrostatische kracht meten, zonder dat het Casimir effect ons parten speelt. Door nu ook de afstand tussen het bolletje en de plaat te moduleren op een andere frequentie, kunnen we een andere lock-in versterker inzetten om de gradiënt van de kracht tussen de objecten te bepalen. Op kleine afstanden bestaat deze krachtsgradiënt voornamelijk uit de gradiënt van de Casimir kracht, omdat de Casimir kracht veel sterker van de afstand afhangt dan de elektrostatische kracht. Op deze manier kunnen we op twee verschillende frequenties kalibreren en de Casimir kracht bepalen, zodat we beide signalen tegelijkertijd kunnen meten.

Voor een goede meting van de Casimir kracht is het essentieel om ervoor te zorgen dat er geen onbedoelde achtergrond krachten zijn die het Casimir

effect zouden kunnen verbergen. Zo'n kracht is bijvoorbeeld de elektrostatische kracht die ontstaat door het natuurlijke spanningsverschil tussen de twee oppervlakken. Zelfs als beide oppervlakken gezamenlijk geaard zijn zullen hun verschillende werkgroten (ook mogelijk in het geval dat beide oppervlakken van hetzelfde materiaal zijn) leiden tot een elektrostatische kracht. Daarom moet de experimentator een extern spanningsverschil aanleggen om te corrigeren voor het verschil in werkgroten, en zodoende deze elektrostatische kracht te verwijderen. Ons modulatie schema biedt een mooie gelegenheid om dit te doen. Het blijkt namelijk dat we nog een lock-in versterker kunnen inzetten die dan werkt op de frequentie van de spanningsmodulatie, en dat we daarmee een negatieve terugkoppel lus kunnen maken die automatisch compenseert voor het verschil in werkgroten door een gelijkspanning aan te leggen die leidt tot minimale elektrostatische kracht. Hierdoor is in al onze metingen het verschil in werkgrote altijd gecompenseerd. Wij hebben in onze experimenten gevonden dat het spanningsverschil afhankelijk kan zijn van de tijd en van de afstand tussen de oppervlakken, wat we uitvoerig bediscussiëren in deze thesis.

De mechanische modulatie van de afstand tussen de oppervlakken waarmee we de Casimir kracht gradiënt meten leidt ook tot een hydrodynamische interactie tussen het bolletje en de plaat. Doordat de hydrodynamische interactie dissipatief is zal die zichzelf manifesteren met een 90 graden verschuiving ten opzichte van de Casimir kracht gradiënt, en kan zodoende onafhankelijk gemeten worden met een lock-in versterker. Daarmee kan onze opstelling eigenlijk zeer precieze metingen uitvoeren van de hydrodynamische kracht en we hebben dan ook metingen gedaan in lucht, stikstof, helium en SF₆ gas. Deze metingen zijn in goede overeenstemming met de theorie.

Gedurende ons onderzoek naar het Casimir effect en de ontwikkeling van onze opstelling, is er in onze groep een nieuwe krachtsensor gebaseerd op glasvezel ontwikkeld: de fiber-top cantilever. Deze sensor is een normale glasvezel waarvan het uiteinde bewerkt is in de vorm van een bladveertje met behulp van een gefocusseerd ionenkanon. De buiging van dit bladveertje ten gevolge van externe krachten kan nauwkeurig bepaald worden door licht door de glasvezel te sturen en de intensiteit te meten van het licht dat door het bladveertje teruggekaatst is de glasvezel in. Later is dit ontwerp wat aangepast door het bladveertje te maken uit een "ferruled optical fiber", wat een glasvezel is die in een ronde glazen behuizing gelijmd zit. Dit ontwerp is iets groter (ongeveer 2 mm in diameter), maar het bladveertje kan slapper gemaakt worden (oftewel: gevoeliger). We hebben laten zien dat zo'n sensor gebruikt kan worden om de Casimir kracht te meten, wat het mogelijk maakt om Casimir krachten te gaan onderzoeken in omgevingen die niet toegankelijk zijn voor conventionele sensoren, zoals explosieve gassen, vloeistoffen of cryogene opstellingen.

In de 4 jaar van ons werk aan het Casimir effect hebben we een nieuwe opstelling gebouwd en deze gebruikt om onderzoek te doen naar de elektro-

statische kracht, naar werlfunctie verschillen tussen de wisselwerkende oppervlakken, naar de hydrodynamische interactie in meerdere gassen, en naar de Casimir kracht tussen verschillende materialen. Het belangrijkste is dat we hebben laten zien dat de Casimir kracht tussen een gouden oppervlak en een oppervlak met een indium-tin-oxide coating een factor 2 zwakker is dan de kracht tussen twee gouden oppervlakken.

List of Publications

Articles

1. A. Borgschulte, R. Gremaud, S. de Man, R. J. Westerwaal, J. H. Rector, B. Dam, and R. Griessen
High-throughput concept for tailoring switchable mirrors
Applied Surface Science **253**, 1417-1423 (2006)
2. S. de Man and D. Iannuzzi
On the use of Hydrogen Switchable Mirrors in Casimir force experiments
New Journal of Physics **8**, 235 (2006) (selected for inclusion in IOP Select)
3. D. Iannuzzi, S. Deladi, J. W. Berenschot, S. de Man, K. Heeck, and M. C. Elwenspoek
Fiber-top atomic force microscope
Rev. Sci. Instr. **77**, 106105 (2006) (selected for inclusion in Virtual J. Nanoscale Sci. & Tech.)
4. D. Iannuzzi, K. Heeck, M. Slaman, S. de Man, J. H. Rector, H. Schreuders, J. W. Berenschot, V. J. Gadgil, R. G. P. Sanders, M. C. Elwenspoek, and S. Deladi
Fibre-top cantilevers: design, fabrication, and applications
Meas. Sci. Tech. **18**, 3247 (2007)
5. A. A. Said, M. Dugan, S. de Man, and D. Iannuzzi
Carving fiber-top cantilevers with femtosecond laser micromachining
J. Micromech. and Microeng. **18**, 035005 (2008)
6. K. Smith, S. de Man, H. Zeijlemaker, A. A. Said, M. Dugan, and D. Iannuzzi
Fiber-top atomic force microscope: a worthwhile challenge
OECC/ACOFT 2008 Conference Proceedings
7. D. Iannuzzi, S. de Man, C. J. Alberts, J. W. Berenschot, M. C. Elwenspoek, A. A. Said, and M. Dugan
Fibre-top micromachined devices Proc. SPIE **7004**, 7004-277 (2008)

8. R. Gremaud, M. Gonzalez-Silveira, Y. Pivak, S. de Man, M. Slaman, H. Schreuders, B. Dam, and R. Griessen
Hydrogenography of PdHx thin films: influence of H-induced stress relaxation processes
Acta Materialia **57**, 1209-1219 (2009)
9. C. J. Alberts, S. de Man, J. W. Berenschot, V. J. Gadgil, M. C. Elwenspoek, and D. Iannuzzi
Fibre-top refractometer
Meas. Sci. Tech. **20**, 034005 (2009)
10. S. de Man, K. Heeck, and D. Iannuzzi
No anomalous scaling in electrostatic calibrations for Casimir force measurements
Phys. Rev. A **79**, (2009) 024102
11. A. Petrušis, J. H. Rector, K. Smith, S. de Man, and D. Iannuzzi
Align-and-shine technique for series production of photolithography patterns on optical fibers
J. Micromech. and Microeng. **19**, 047001 (2009)
12. S. de Man, K. Heeck, R. J. Wijngaarden, and D. Iannuzzi
Halving the Casimir force with conductive oxides
Phys. Rev. Lett. **103**, 040402 (2009).
This Letter is highlighted in P. Ball, *Relaxing the vacuum*, Nature Materials **8**, 705 (2009)
13. A. Petrušis, J. H. Rector, K. Smith, S. de Man, and D. Iannuzzi
Align-and-shine photolithography
Proc. SPIE **7503**, 75036Q (2009)
14. G. Gruca, S. de Man, M. Slaman, J. H. Rector, and D. Iannuzzi
Ferrule-top micromachined devices: a new approach to fibre-top technology
Proc. SPIE **7503**, PDP07 (2009)
15. S. de Man, K. Heeck, R. J. Wijngaarden, and D. Iannuzzi
Contact potentials in Casimir force setups: an experimental analysis
J. Vac. Sci. Technol. B **28**, C4A25 (2010)
16. S. de Man, K. Heeck, K. Smith, R. J. Wijngaarden, and D. Iannuzzi
Casimir force experiments in air: two birds with one stone
Int. J. Mod. Phys. A **25**, 2231 (2010)
17. S. de Man, K. Heeck, K. Smith, R. J. Wijngaarden, and D. Iannuzzi
Casimir force experiments in air: two birds with one stone
Proceedings of QFEXT09 (World Scientific), 98 (2010)

18. G. Gruca, S. de Man, M. Slaman, J. H. Rector, and D. Iannuzzi
Ferrule-top micromachined devices: design, fabrication, performance
Meas. Sci. Tech. **21**, 094003 (2010)
19. Y. Y. Villanueva, D. V. Denisov, S. de Man, and R. J. Wijngaarden
Casimir-like effect on a granular pile
Phys. Rev. E **82**, 041303 (2010)
20. D. Chavan, G. Gruca, S. de Man, M. Slaman, K. Heeck, and D. Iannuzzi
Ferrule-top atomic force microscope
Rev. Sci. Instr. **81**, 123702 (2010) (selected for inclusion in Virtual J. Nanoscale Sci. & Tech.)
21. S. de Man and E. Jeffrey
Simple fiber-optic interferometer with linear phase response
Submitted for publication
22. P. Zuurbier, S. de Man, G. Gruca, K. Heeck, and D. Iannuzzi
Measurement of the Casimir force with a ferrule-top sensor
New J. Phys. **13**, 023027 (2011)
23. S. de Man, K. Heeck, and D. Iannuzzi
Halving the Casimir force with conductive oxides: experimental details
Phys. Rev. A **82**, 062512 (2010)

Patent

1. Iannuzzi, Gruca, de Man: Ferrule-top devices, US Provisional Application No. 61/204,541

Talks

1. Fluctuate 08 workshop, Kavli Institute for Theoretical Physics, Santa Barbara, CA, USA (invited visiting scientist November 10-14, 2008)
2. Physics@FOM Veldhoven 2009, Veldhoven, The Netherlands, contributed talk (January 21, 2009)
3. Casimir symposium at CNRS/Université Joseph Fourier, Grenoble, France, invited talk (February 26, 2009)
4. 12th International Conference on Non-Contact Atomic Force Microscopy, Casimir Satellite workshop, Yale University, New Haven, CT, USA, contributed talk (August 2009)

5. Casimir, van der Waals, and nanoscale interactions, ESF and Université Joseph Fourier, Les Houches, France, invited talk (April 2010)
6. Quantum Lunch, Theoretical Division Los Alamos National Laboratory, Los Alamos, NM, USA (invited visiting scientist July 5-16, 2010)
7. Colloquium at Sandia National Laboratories, Albuquerque, NM, USA (invited visiting scientist July 13-14, 2010)

Acknowledgment

This work would not have been possible without the numerous help of many people. I am grateful to all of you.

Curriculum Vitae

Sven de Man was born on October 26, 1983, in Almere, The Netherlands. In 2000, he graduated *cum laude* from highschool "De Meergronden", at the age of 16 and with eleven subjects instead of the compulsory seven. In 2001, he obtained his Propaedeutics in Physics and Astronomy *cum laude* from the VU University Amsterdam, for which he was awarded the Physica propaedeutics prize from the Holland Society for the Sciences. In 2002, while also studying for his Physics Bachelor degree, he received his Propaedeutics in Mathematics and Statistics from the VU University Amsterdam. In 2004, he obtained his bachelor degree in Physics and Astronomy *cum laude* from the VU University Amsterdam, with a project on the catalytic properties of nickel-oxide for hydrogen absorption in the group of prof.dr. R. Griessen. In 2007, he received his master degree in Condensed Matter Physics *cum laude* from the VU University Amsterdam, with a thesis on the Casimir effect in the group of dr. D. Iannuzzi.

From September 2006 to September 2010 he has been a PhD student at the VU University Amsterdam in the IDEAS^{μm} group of dr. D. Iannuzzi, which is part of the Condensed Matter Physics group of prof.dr. R. Griessen. During this period, he conducted research on the Casimir effect and on fiber-top and ferrule-top sensors. In the last one and a half year he has been collaborating with the group of prof.dr. D. Bouwmeester at Leiden University. He was also a short-term visiting scientist at KITP Santa Barbara in California in autumn 2008 and at Los Alamos National Laboratory and Sandia National Laboratories in summer 2010.